12-7-2005

Dynamic Aeroelastic Analysis of Wing/Store Configurations

Gregory H. Parker

DYNAMIC AEROELASTIC ANALYSIS OF WING/STORE CONFIGURATIONS

DISSERTATION

Gregory Hershel Parker
Major, USAF

AFIT/DS/ENY/06-06

AFIT/DS/ENY/06-06

DYNAMIC AEROELASTIC ANALYSIS OF WING/STORE CONFIGURATIONS

DISSERTATION

Presented to the Faculty

Graduate School of Engineering and Management

Air Force Institute of Technology

Air University

Air Education and Training Command

in Partial Fulfillment of the Requirements for the

Degree of Doctor of Philosophy

Gregory Hershel Parker, B.S., M.S.

Major, USAF

December 2005

AFIT/DS/ENY/06-06

DYNAMIC AEROELASTIC ANALYSIS OF WING/STORE CONFIGURATIONS

Gregory Hershel Parker, B.S., M.S.

Major, USAF

Approved:

(signature)	7 Dec 05
Lt. Col. Raymond C. Maple	Date
Committee Chairman	
(signature)	7 Dec 05
Philip S. Beran	Date
Committee Member	
(signature)	7 Dec 05
Paul I. King	Date
Committee Member	
(signature)	7 DEC 05
Paul E. Crittenden	Date
Committee Member	
(signature)	Dec 7, 2005
Meir Pachter	Date
Dean's Representative	
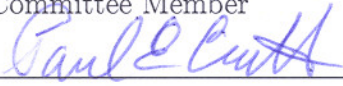
(signature)

Robert A. Calico, Jr
Dean

AFIT/DS/ENY/06-06

Abstract

Aircraft with stores can exhibit aeroelastic limit-cycle oscillation in the transonic regime. Limit-cycle oscillation is an aeroelastic phenomenon characterized by limited amplitude, self-sustaining oscillations produced by fluid-structure interactions. In order to study this phenomenon for practical configurations, a first-order accurate code was developed to interface a modal structural model with a commercial, parallel, Euler/Navier-Stokes fluid solver with a deforming grid capability. Initial testing of this code was completed on the Goland$^+$ and AGARD 445.6 wings.

Limit-cycle oscillation was simulated for the Goland$^+$ rectangular wing and was successfully compared to previously reported findings. It was found that the aerodynamic nonlinearity responsible for limit-cycle oscillation in the Goland$^+$ wing was the periodic appearance/disappearance of shocks. The Goland$^+$ structural model was such that in the transonic flutter dip region, the primary bending and twisting modes were in phase and coupled to produce a single-degree-of-freedom, torsional flutter mode about a point located ahead of the leading edge of the wing. It was determined that the combination of strong trailing-edge and lambda shocks which periodically appear/disappear, limited the energy flow into the structure. This mechanism quenched the growth of the flutter, resulting in a steady limit-cycle oscillation.

Under-wing and tip stores were added to the Goland$^+$ wing to determine how they affected limit-cycle oscillation. It was found that aerodynamic store shapes affect limit-cycle oscillation in two offsetting ways: by interfering with the flow field on the wing surface, and by transferring additional store forces into the structure. The under-wing stores interfere with the airflow on the lower surface of the wing which decreases limit-cycle oscillation amplitudes, whereas, under-wing and tip store forces transferred into the wing structure directly increase limit-cycle oscillation amplitudes.

Acknowledgments

I owe thanks to many people that made this work possible. Foremost among those, and to whom I owe a great debt of gratitude, are my dissertation advisor, Lt Col Raymond Maple and my research advisor and sponsor, Dr. Philip Beran. They always kept me motivated and focused on the research effort whenever I would become frustrated. I would like to thank Dr. Paul King for all his advice and for helping with all the administrative hurtles. I would also like to thank Dr. Larry Chilton, Dr. Paul Crittenden, and Dr. Meir Pachter for helping define the scope of the project and for reviewing this document. Thanks to Dr. Robert Canfield, Dr. Richard Snyder, and Dr. Oddvar Bendiksen for the many insightful discussions.

This research would not have been completed without tremendous computer support from Dave Doak and Jason Speckman. I received an amazing amount of support from FLUENT Inc. when developing this code, especially Dr. Greg Stuckert, Dr. Jeff Ma, and Dr. Christophe Hiemcke. I also would like to thank the MSU ERC for providing me with SolidMesh and for training me how to use it, especially Dr. David Marcum, Dr. Montgomery Hughson, and Dr. Eric Blades. I would like to thank Dr. Hugh Thornburg for his assistance with Gridgen as well as Jacob Freeman, John Staples, and Dr. Charles Denegri for providing F-16 data. I would also like to thank my fellow PhD students. The many hours sitting at my desk and running simulations were made bearable through their camaraderie and friendship.

Finally, I wish to thank all of my family. I could not have made it without the understanding and support of my parents and my in-laws. Most importantly, I want to thank my wife for taking care of me these last three years. Her love, devotion, and encouragement were a constant source of strength for me. My son and my daughter also kept reminding me what is truly important in life, and it is to them and to my wife that I dedicate this work.

Table of Contents

List of Figures

List of Tables

Nomenclature

Symbol	Description
b	wing span
c	wing chord
$[C]$	damping matrix
C_L	aerodynamic lift coefficient
C_M	pitching moment coefficient
C_P	pressure coefficient
dA	differential surface area
E	energy per unit mass
E	Young's modulus
F	force
G	shear modulus
$[K]$	stiffness matrix
M	Mach number
$[M]$	mass matrix
N	number of modes
n	time step
P	pressure
q	coordinates
q	dynamic pressure
$\{\boldsymbol{q}\}$	heat flux vector
R	gas constant
Re	Reynold's number
$[S]$	spline matrix
t	time
T	temperature

u	x-component of velocity vector
$\{u\}$	modal displacement vector
$\{\dot{u}\}$	modal velocity vector
$\{\ddot{u}\}$	modal acceleration vector
v	y-component of velocity vector
$\{\boldsymbol{v}\}$	velocity vector
V	arbitrary control volume
w	z-component of velocity vector
x	stream-wise position
z	vertical position
δ	displacement
$\triangle t$	time step
γ	ratio of specific heats
ω	frequency
$[\Phi]$	modal matrix
ρ	density
ρ_s	structural density
τ	thickness
$\boldsymbol{\tau}$	viscous stress tensor

Subscripts

a	aerodynamic
e	experimental
g	generalized
s	structural
∞	free-stream

Abbreviations

Abbreviation	Definition
AFIT	Air Force Institute of Technology
AOA	angle-of-attack
ASC	Aeronautical Systems Center
CFD	computational fluid dynamics
CSD	computational structural dynamics
EA	elastic axis
GB	gigabyte
LCO	limit-cycle oscillation
LES	large-eddy simulation
RAM	random access memory
RNG	renormalized group
ROM	reduced order modelling
RSM	Reynold's stress model
SST	shear-stress model
TSDT	transonic small disturbance theory
UDF	user-defined function

DYNAMIC AEROELASTIC ANALYSIS OF WING/STORE CONFIGURATIONS

I. Introduction

Aeroelasticity is the interaction between an elastic structure in an air stream and the resulting aerodynamic force [29]. The performance of aircraft is often limited by adverse aeroelastic interactions such as flutter. Flutter is defined as: "A dynamic instability of a flight vehicle associated with the interaction of aerodynamic, elastic, and inertial forces" [29]. Classical flutter is characterized by catastrophic diverging oscillations [15].

Aircraft operating in the transonic region risk encountering limit-cycle oscillation (LCO) which is also called limit-cycle flutter and limited amplitude flutter [8]. Limit-cycle oscillations are limited amplitude, self-sustaining oscillations produced by fluid-structure interactions. LCO results in undesirable airframe vibrations that adversely affect a pilot's ability to function and degrades targeting accuracy for fighter aircraft. Aircraft with high aspect ratio or highly swept wings can experience LCO [41]. For typical LCO, the amplitude is constant for a given flight speed. The amplitude increases when the flight speed is increased and a new constant amplitude is obtained when the flight speed is again fixed [8]. If the flight speed is decreased but is still above the flutter point, a new constant, lower amplitude is obtained. If the flight speed is decreased below the flutter point, the oscillations damp out. For nontypical LCO, the amplitude does not increase as the flight speed increases [8].

LCO is related to flutter, which occurs when the dynamic pressure is increased to a critical value above which the system becomes dynamically unstable. When a non-linear mechanism that counters the amplitude growth is present in this unstable

region, LCO can result. The nonlinearity that sustains LCO can be in the structure, the aerodynamic flow, or in both. The case of interest for this study was the nonlinearity in the aerodynamic flow. Sources of aerodynamic nonlinearity include separated flow and shock motion in transonic flow [17].

Advances in nonlinear modelling and computer hardware have led to nonlinear aeroelastic predictions for reasonably complex configurations [22, 23, 24, 42, 44]. However, there is continued interest in LCO motivated by the need to further understand the physics and mechanisms involved in LCO so that better LCO predictive tools can be developed [12, 15, 52]. This research examines the aerodynamic nonlinearities for a clean wing and the non-linear aerodynamic effects induced by underwing stores. There have been several efforts where LCO driven by aerodynamic nonlinearities were studied [35, 42, 44]. This research adds to this knowledge base by providing a detailed analysis of the shock motion during LCO and by determining the role of store aerodynamics in LCO.

Tijdeman and Seebass [56] characterized the periodic motion of shock waves on oscillating airfoils into three different types. In type-A shock motion, the shock wave moves fore and aft sinusoidally. The shock strength may vary as the shock moves, but the shock is always present [56]. In type-B shock motion, the shock moves sinusoidally as in type-A, but the shock disappears during a part of its backward motion [56]. Type-C shock motion occurs when a periodic shock wave leaves the airfoil and continues upstream as a weak, free shock-wave [56]. Bendiksen [5] has shown that if a transonic flutter mode that appears to be a single-degree-of-freedom, torsional motion, ahead of the leading edge, has a phase angle between bending and torsion less than approximately 10 degrees, and has a transition from a type-A to type-B shock motion, it is likely that LCO will result. This type-B shock motion limits the flow of energy from the fluid to the structure, resulting in LCO [5].

Under-wing and tip stores can affect LCO by changing the inertial properties of the wing, and by changing the aerodynamics of the wing. If a store mass is

added forward of the elastic axis (EA), the flutter speed generally increases, which produces a stabilizing effect [32]. If a store mass is added aft of the elastic axis, it has a destabilizing effect [32]. Exceptions to this can occur in the transonic flutter dip region [6, 7]. Therefore, if there is typical LCO at a given airspeed and a mass is added ahead of the elastic axis, and it raises the flutter speed, the LCO amplitude will decrease because the given fixed airspeed becomes closer to the flutter speed. If the mass is moved aft of the elastic axis and it lowers the flutter speed, the LCO amplitudes will increase.

The role of store aerodynamics in LCO is less well understood. One can hypothesize two primary mechanisms by which store aerodynamics affect LCO: the stores could change or interfere with the airflow on the wing, thereby changing how the shock motion is limiting the energy transferred into the structure; and the store aerodynamic carriage loads that are transferred into the structure could sufficiently change the total forces experienced by the wing, thereby changing the LCO response. The first mechanism deals with changes to the wing aerodynamics because of the presence of the store. The second mechanism is independent of any changes to the wing aerodynamics and any changes in the LCO are because of aerodynamic forces experienced by the store. The most likely method that store aerodynamics affect LCO is through a combination of these two.

1.1   Overview of Computational Aeroelasticity

Several computational methods have been used to model fluid-structure interactions such as flutter and LCO. The simplest and fastest method is to use a finite element formulation for the structure and a linear aerodynamic model such as the doublet-lattice method for the fluid [31]. Finite element models are very fast and accurately predict instability frequencies, therefore, they are often used as a first step in aeroelastic analysis [6, 7, 12, 13, 15, 51]. However, in the transonic region where the aerodynamic flow is non-linear, these methods do not accurately predict

flutter onset velocity [12]. Accuracy can be improved when using a finite element formulation for the structure by employing an unsteady-aerodynamics computation procedure such as an aerodynamic-influence-coefficient matrix. This procedure calculates the unsteady aerodynamics once and stores the results in tables that are reused for repetitive aeroelastic computations [10].

Greater accuracy can be obtained by using a more complex aerodynamic model. A computationally efficient aerodynamic model that is frequently used solves the three-dimensional transonic small disturbance potential flow equations. This method has been used in research codes [34] and in the NASA Langley developed CAPTSDv [3, 6, 7, 14, 31, 51]. Mildly separated flows have been studied with CAPTSDv with the addition of an inverse integral boundary layer model [31]. These models are more accurate than linear aerodynamic models but they do not completely capture the intricacy of the flow due to shock-boundary layer interaction or large angles of attack.

The latest aeroelastic codes solve the Euler equations for inviscid flows or the Navier-Stokes equations for viscous flows for even greater accuracy, but at a cost of greater computational time. The most widely available of these codes are ENS3DAE and CFL3DAE. ENS3DAE was developed by the Lockheed-Georgia Company. It uses a central finite-difference scheme and structured grids. It has been used to solve a large number of aeroelastic problems [6, 7, 31, 51]. CFL3DAE was developed by NASA Langley. It uses an upwind finite-volume scheme and structured grids. It has also been used to solve a large number of aeroelastic problems [3, 6, 7, 31, 51]. In addition to these widely distributed codes, the majority of the latest research codes use a finite-volume scheme to solve the Euler/Navier-Stokes equations. Most of these codes are based on structured grids [26, 27, 37, 42, 43, 44, 45, 46, 53] while a few recent codes use unstructured grids [20, 21, 22, 23, 33, 35, 47, 48].

In an effort to attain the greater accuracy obtained from using Euler/Navier-Stokes solvers, without the computational expense, there is significant research in

the area of reduced order modelling (ROM). In these methods, the dominant spatial modes of the flow field are determined and used to represent the flow [16]. The most common ROM techniques include harmonic balance [54, 55] and proper orthogonal decomposition [16]. ROM can reduce the computational expense by several orders of magnitude but care must be taken that the flow field is not over simplified, thereby, excluding or changing the nonlinearity being studied.

Computational methods have successfully been used to predict the flutter point of several aircraft wings. The most common case studied [9, 27, 33, 34, 35, 37, 38, 40, 45, 47, 48, 49] is the AGARD 445.6 weakened wing, which has been presented as a standard aeroelastic test case [57]. Experimental flutter data for this wing is available at several points between Mach 0.499 and Mach 1.141 [57]. This test case has often been used to validate aeroelastic programs. With various computational aeroelasticity methods, good agreement with experimental data was achieved for subsonic results but all the computational methods tend to over predict the flutter point for supersonic results [9, 27, 33, 34, 35, 37, 38, 40, 45, 49]. It has been found that inclusion of turbulence and viscous effects slightly improved the flutter point predictions of the AGARD 445.6 wing [27].

Computational methods have also been successfully used to predict the flutter point of fighter wings. Computational results compared well with flight test results for an F-16 in clean configuration [22, 23, 43] and with stores [10]. It has been noted that the level acceleration achievable by an F-16 does not significantly impact its aeroelastic parameters. However, increasing the wing loading by increasing the angle-of-attack increased the aeroelastic torsional frequency. For a generic delta fighter wing with stores, it has been found that adding or changing the store in the structure affected the flutter point, however store aerodynamics only affected the supersonic flutter point, not the subsonic [34, 53]. It has also been found that computational aeroelasticity methods which take into account aerodynamic nonlinearities produce

a much more conservative flutter boundary than linear theory in high transonic flow [33, 35].

All of the previously listed computational aeroelasticity methods have been used to study wings with linear structural models that exhibit transonic limit-cycle oscillations. For the Goland$^+$ rectangular wing with a tip store [6, 7, 51], researchers found that LCOs occurred at speeds less than that predicted using linear analysis and at speeds lower than that computed for a clean wing. They also found that modelling the aerodynamics of the tip store did not affect the LCO. Each of the computational methods they tested showed LCO responses over the Mach range 0.91 through 0.94 but with different onset velocities [6]. The computed frequencies were qualitatively similar but did not agree in magnitude as well as expected [6].

Attempts have been made to model LCO in the F-16 in both a clean configuration and with stores. Melville discovered a limit-cycle oscillation case for an F-16 without stores at 10 degrees angle-of-attack [42, 44]. He determined that the shock-induced, trailing-edge separation was a critical nonlinear limiting mechanism responsible for LCO. Denegri has identified F-16 store configurations that lead to LCO during flight test [13, 15]. These configurations have been used to computationally model LCO with mixed results [14, 47, 48, 54, 55]. The computed LCO amplitudes have not successfully duplicated those seen in flight test. Research on this configuration is continuing in order to determine what fidelity of computational model is required to correctly simulate this LCO.

1.2   Scope of Research

The objective of this research is to determine how nonlinear aerodynamics quench the energy flow from the fluid into the structure resulting in LCO. It is known that shock motion is the nonlinearity responsible for LCO in the Goland$^+$ wing, but it is not understood how this shock motion quenches the flutter growth resulting in LCO. It is also known that adding under-wing stores to the structure affects the

flutter onset speed. However, it is not understood how the store aerodynamics affect the LCO response nor is it understood how they affect the quenching mechanism responsible for LCO. The scope of this research is defined by the following thesis statement and research approach.

1.2.1 Thesis Statement. The primary bending and torsional modes that are known to couple in the Goland$^+$ wing, result in periodic shocks that are responsible for inhibiting divergent flutter by decreasing the restoring forces on the wing, resulting in a balancing of the inertial forces and a stable limit-cycle oscillation. Further, store aerodynamics do not cause limit-cycle oscillation but can decrease or increase the amplitude of the limit-cycle oscillation depending on the size and location of the store.

1.2.2 Research Approach. In order to address the thesis statement, a computational aeroelasticity code was developed around a commercial computational fluid dynamics (CFD) code and a linear modal structural model. It was required that the CFD code have the capability to interact with user written programs. This interaction allowed a structural model to be linked to the CFD code. The CFD code also had to incorporate a deforming mesh capability in order to simulate the flow around a moving wing. Finally, the CFD code had to use unstructured grid methodology. Unstructured grids were required in order to speed up the grid generation time since multiple configurations were studied. In addition to these requirements, it was desired that the CFD code solve the Navier-Stokes equations and have multiple turbulent models for greater accuracy. FLUENT 6.1 by FLUENT Incorporated was chosen because it met these requirements. Once the CFD code was chosen, it was linked to a modal structural model in order to create an aeroelastic program.

Once the aeroelastic program was developed and validated, it was used to simulate transonic LCO. External aerodynamic stores with pylons were then added in order to analyze how the LCO response changed. The stores were not added to

the structural model, only to the aerodynamic model. Modal response, force and moment data, velocity vectors, pressure contour maps, Mach contour maps, density contour maps, power spectral density plots, work on the structure, and wing tip response were studied in order to quantify how the store aerodynamics affected the LCO and to determine what aerodynamic nonlinearity was providing the quenching mechanism responsible for the LCO.

1.3 Document Organization

This document is organized into five chapters. Chapter I introduces the problem, discusses prior work, states the thesis of the research, and lays out the organization of the document.

Chapter II provides an overview of FLUENT 6.1. It also describes the aeroelastic program that was written to interact with FLUENT in order that it could be used as an aeroelastic analysis tool.

Chapter III describes the validation of the aeroelastic program. It covers the prescribed motion, Goland$^+$ wing, and AGARD 445.6 wing test cases used in validating this aeroelastic analysis method.

Chapter IV discusses the results obtained using the aeroelastic program. The chapter is divided into three sections. The first section discusses the Goland$^+$ wing without aerodynamic stores and analyzes the quenching mechanism responsible for the LCO. The second section discusses the Goland$^+$ wing with aerodynamic underwing stores and their effect on LCO. The last section discusses the Goland$^+$ wing with an aerodynamic tip store and its effect on LCO.

Chapter V summarizes the conclusions and provides recommendations for future research.

In addition to these five chapters, this document contains supporting appendices that provide detailed information in support of the five main chapters.

II. Aeroelastic Program

2.1 Aeroelastic Analysis Method

One goal of this research effort was to extend the investigation of Dr Beran, et al. [6, 7, 51] by evaluating the capability of a commercial, parallel, Euler/Navier-Stokes fluid solver, coupled with a modal-analysis structure model, to accurately predict aeroelastic behavior such as flutter and LCO. There is not currently available a dynamic-aeroelastic analysis tool based on a fully unstructured formulation. This is needed to reduce the grid-generation time in order to investigate LCO for complex wing/store/pylon configurations. Grid generation for these configurations is difficult for structured methods and usually requires overset technology [4, 39].

FLUENT 6.1 by FLUENT Incorporated was chosen to fill the need for a commercial solver that could handle geometrically-complex configurations undergoing structural deformation. FLUENT 6.1 is an unstructured fluid solver with a deforming grid capability that can be controlled through a user-written subroutine called a user-defined function (UDF). A UDF was written that extracted aerodynamic force data from the fluid solver and applied it to a modal structure model in order to deform the grid. By coupling FLUENT with a modal structure model, groundwork was laid to analyze aeroelastic problems for complex geometries.

2.2 Overview of FLUENT 6.1

FLUENT is a commercially available computer program for modelling fluid flow and heat transfer in complex geometries. FLUENT solves flow problems using unstructured meshes that can be generated about complex geometries with relative ease [2]. FLUENT uses a control-volume-based technique which consists of integrating the governing equations on a control-volume basis yielding discrete equations [2]. FLUENT has two different fluid solvers: a segregated solver and a coupled solver. The segregated solver is for low speed or incompressible fluids. For compressible

fluids, the coupled solver should be used. The coupled solver solves the governing equations of continuity, momentum, energy, and species transport (if required) simultaneously. The governing equations can be written in vector form as:

$$\frac{\partial}{\partial t} \int_V W \, dV + \oint (F - G) \cdot dA = \int_V H \, dV \qquad (2.1)$$

where W, F, and G are defined as

$$W = \left\{ \begin{array}{c} \rho \\ \rho u \\ \rho v \\ \rho w \\ \rho E \end{array} \right\}, \qquad F = \left\{ \begin{array}{c} \rho \boldsymbol{v} \\ \rho \boldsymbol{v} u + P\hat{i} \\ \rho \boldsymbol{v} v + P\hat{j} \\ \rho \boldsymbol{v} w + P\hat{k} \\ \rho \boldsymbol{v} E + P\boldsymbol{v} \end{array} \right\}, \qquad G = \left\{ \begin{array}{c} 0 \\ \boldsymbol{\tau}_{xi} \\ \boldsymbol{\tau}_{yi} \\ \boldsymbol{\tau}_{zi} \\ \boldsymbol{\tau}_{ij} \boldsymbol{v}_j + \boldsymbol{q} \end{array} \right\}, \qquad (2.2)$$

and H contains source terms such as body forces and energy sources [2].

Because the governing equations are non-linear and coupled, several iterations must be performed to obtain convergence. Each iteration consists of the following steps [2]:

1. Fluid properties are updated, based on the current solution. (If the calculation has just begun, the fluid properties will be set to the initial conditions.)

2. The continuity, momentum, and energy equations are solved simultaneously.

3. Where appropriate, equations for scalars such as turbulence are solved using the previously updated values of the other variables.

4. A check for convergence is made.

These steps are continued until the convergence criteria is met [2]. When performing unsteady simulations, FLUENT uses an implicit-time formulation (dual-time stepping) which treats each physical time step of the unsteady problem as

a steady state problem, which is run to convergence. The solver can be run with first or second-order temporal accuracy, however, the deforming mesh algorithms are only supported by the first-order time-accurate solver. The coupled solver employs a first or second-order, spatially-accurate, upwind method to solve the governing equations [2].

FLUENT includes three mesh-motion methods that can be used to update the volume mesh in the deforming regions of the grid based on motion defined at the boundaries: spring-based smoothing, dynamic layering, and local remeshing [2]. In the spring-based smoothing method, the edges between any two mesh nodes are idealized as a network of interconnected springs. The initial configuration of the edges before any boundary motion constitutes the equilibrium state of the mesh [2]. A displacement at a given boundary node will generate a force proportional to the displacement along all the springs connected to the node. The second method, dynamic layering, can be used in prismatic-mesh zones to add or remove layers of cells adjacent to a moving boundary [2]. The third method is remeshing. When the spring-based smoothing method is used, the boundary displacement may become large compared to the local cell sizes. This can cause the cell quality to deteriorate or the cells to become degenerate [2]. This can result in negative cell volumes or convergence problems when the solution is updated to the next time step. To circumvent this problem, FLUENT agglomerates cells that violate user-specified skewness or size criteria and locally remeshes the agglomerated cells [2]. If the new cells satisfy the skewness and the size criteria, the mesh is locally updated with the new cells [2].

FLUENT provides several turbulent models for modelling turbulent flows, including the Spalart-Allmaras model, standard $k - \varepsilon$ model, renormalization-group (RNG) $k - \varepsilon$ model, realizable $k - \varepsilon$ model, standard $k - \omega$ model, shear-stress transport (SST) $k - \omega$ model, Reynolds stress model (RSM), and large-eddy simulation (LES) model [2].
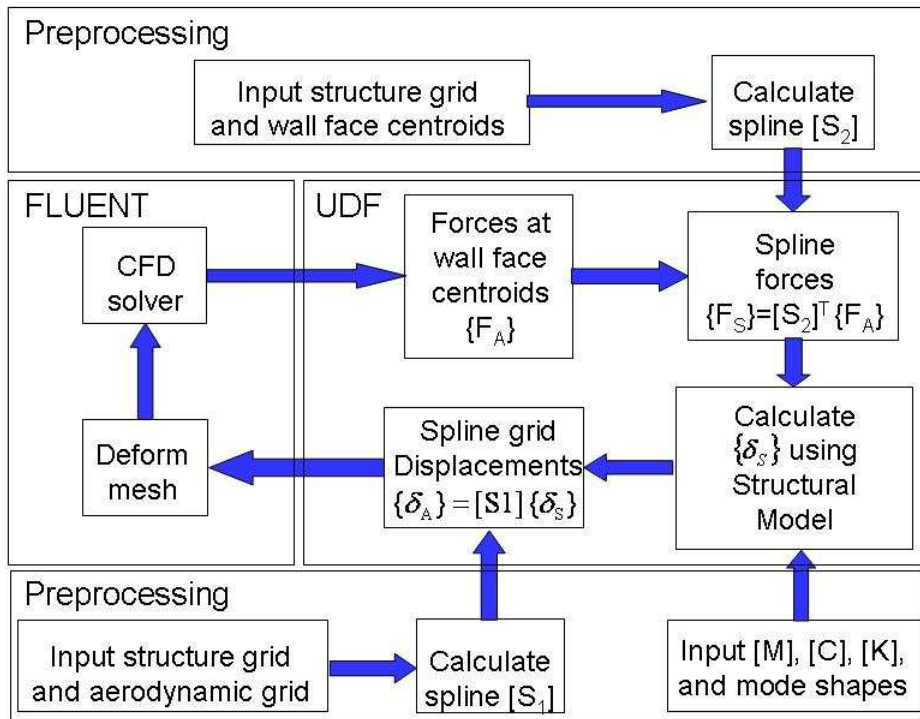
Figure 2.1   Aeroelastic Program Flowchart

2.3   Overview of Aeroelastic Program

The aeroelastic program developed around FLUENT is depicted in Figure 2.1. FLUENT solves the Euler/Navier-Stokes equations (equations 2.1 and 2.2) and calculates flow variables such as velocity, pressure, density, temperature, etc., for each cell in the flowfield. It also deforms the mesh based on new wing-node coordinates when they are provided. The remainder of the aeroelastic program is a UDF (written in C) that is called by FLUENT. In addition to the aerodynamic and structural grids, the aeroelastic program has five main inputs: two spline matrices, a mode shape matrix, a mass matrix, and a stiffness matrix. The mode shape matrix, the mass matrix, and the stiffness matrix are determined during modal

analysis preprocessing using software such as MSC/NASTRAN. The output from preprocessing is then reformatted for input into the aeroelastic program.

In general, the grid used by the structural model and the aerodynamic grid used by FLUENT are non-point matching. A spline matrix $[S]$ is used to interpolate displacement data from the structural grid $[\delta_s]$ to the aerodynamic grid $[\delta_a]$ using the equation

$$[\delta_a] = [S][\delta_s]. \qquad (2.3)$$

It is also used to interpolate force data from the aerodynamic grid $[F_a]$ to the structural grid $[F_s]$ using the equation

$$[F_s] = [S]^T[F_a]. \qquad (2.4)$$

Because FLUENT provides aerodynamic forces at cell centers rather than at grid nodes, the coupling between the fluid and structural models is accomplished with two splines. The first spline matrix (S_1) is created to spline displacements between the structural grid points and the aerodynamic grid points. FLUENT calculates pressures at the cell centers. These pressures are then extrapolated to the face centroids on the wing and used with the wall-face area vectors to calculate the pressure forces. These pressure forces are then combined with the viscous shear forces to get the total forces. Since the total forces are at the face centroids and not at the aerodynamic grid points, a second spline matrix (S_2), is created to spline between the structural grid points and the wall-face centroids on the aerodynamic grid. Coordinates for the structural grid nodes, aerodynamic grid nodes, and aerodynamic-grid wall-face centroids are used during preprocessing to create these two spline matrices.

The two spline techniques chosen for this application were the thin-plate spline [1, 18, 50] and the infinite-plate spline [1, 28, 50]. Details of the spline algorithms are presented in Appendix A. Both the thin-plate and infinite-plate spline are based on

the undeformed node coordinates of the two computational grids, therefore, they are computed and stored during pre-processing.

The Newmark algorithm [30], presented in Appendix B, was used to discretize the structural model. The semi-discrete equations of motion can be written as

$$[M]\{\ddot{u}\} + [C]\{\dot{u}\} + [K]\{u\} = \{F\} \qquad (2.5)$$

where $[M]$ is the mass matrix, $[C]$ is the damping matrix, $[K]$ is the stiffness matrix, $\{F\}$ is the vector of applied forces, and $\{u\}$, $\{\dot{u}\}$, and $\{\ddot{u}\}$ are vectors of modal displacements, modal velocities, and modal accelerations, respectively [30]. Assuming a linear acceleration and no structural damping, the Newmark algorithm is used to solve equation 2.5 for $\{u\}_{n+1}$ with the following set of equations:

$$\left([M] + \frac{\Delta t^2}{6}[K]\right)\{\ddot{u}\}_{n+1} = \{F\}_{n+1} - [K]\left(\{u\}_n + \Delta t\{\dot{u}\}_n + \frac{\Delta t^2}{3}\{\ddot{u}\}_n\right), \qquad (2.6)$$

$$\{\dot{u}\}_{n+1} = \{\dot{u}\}_n + \frac{\Delta t}{2}\left((\{\ddot{u}\}_n + \{\ddot{u}\}_{n+1}\right), \qquad (2.7)$$

and

$$\{u\}_{n+1} = \{u\}_n + \Delta t\{\dot{u}\}_n + \frac{\Delta t^2}{6}\left(2\{\ddot{u}\}_n + \{\ddot{u}\}_{n+1}\right). \qquad (2.8)$$

FLUENT uses an implicit, dual-time stepping formulation for unsteady flow simulations. Because of this dual-time stepping formulation, and the lack of a provision to extract wall-force values and a fractional, physical, time-step size during the sub-iterations, the fluid solver and structural model can only be coupled at the end of each physical time-step. Therefore, the structure always lags the fluid solver by one time-step.

The aeroelastic program moves an attached store as a rigid body based on how the pylon attachment points move on the wing surface. The aerodynamic forces and moments acting on the store are calculated and transferred into the structure

through the pylon, in order that any aerodynamic effects on the store are felt by the structural model. These forces can also be turned off or ignored, allowing the aerodynamic interference on the bottom of the wing due to the store to be isolated. In order to determine how much of an effect the store forces are having on LCO as compared with how much of an effect the store interference with the wing is having on LCO, the aeroelastic program can also magnify the store forces that are transferred into the structure. In addition, these magnified forces can be reversed in direction in order to further isolate their effect. The aeroelastic analysis program also allows for inertial forces to be added to the store aerodynamic forces. To add inertial forces, a mass and mass location are entered into the aeroelastic program. The acceleration vector of the mass is calculated from the store motion. This acceleration vector is multiplied by the mass to obtain an inertial force vector which is converted to forces and moments at the store attachment location. These forces are then transferred into the original structural model.

A typical aeroelastic analysis is started by computing an initial, steady-state solution for the undeformed wing. This solution is used as the starting point for the unsteady, deforming-grid computations. At the start of the unsteady run, the forces at the wall-face centroids on the wing are calculated. These forces are then splined using equation 2.4 to the structural-grid nodes. New deformed structural-grid coordinates are then calculated using the Newmark method. These new structural displacements are then splined using equation 2.3 to get new aerodynamic-grid coordinates. FLUENT then deforms the mesh based on the new coordinates, increments the time-step, and calculates new flow variables. This process repeats until a specified flow time is reached.

The aeroelastic program is fully parallelized to take advantage of using multiple processors. The fluid solver is second-order accurate spatially, and first-order accurate temporally (when using the deforming mesh algorithms). The structural model is second-order accurate, both spatially and temporally.

III. Validation of Aeroelastic Program

The aeroelastic program described in chapter II was implemented as FLUENT user-defined functions in the C programming language. The components of the aeroelastic program (splines, structural model, etc.) were tested individually to verify correctness. The thin-plate spline was then tested to obtain an estimate of the error induced in the system when transferring data from one grid to the other. The full aeroelastic program was then tested in two stages, first with prescribed structural motion, then through full aeroelastic structural motion using two different 3-D wing configurations: the AGARD 445.6 wing, flutter case, and the Goland$^+$ wing, LCO case.

The aerodynamic forces were calculated by the fluid solver for the aerodynamic grid. These forces were then transferred to the structural grid through the use of a spline matrix. Any errors introduced in the force distribution, by the spline matrix, would result in an inaccurate deformation of the wing. In order to quantify the errors induced when transferring forces from the aerodynamic grid to the structural grid, the thin-plate spline was tested first with a model problem and then with the Goland$^+$ LCO case. The model problem was a flat plate. The "aerodynamic" grid was created by evenly dividing the top and bottom surfaces of the plate into six by four cells with a node at the center of each cell. The "structural" grid was created by evenly dividing the top and bottom surfaces of the plate into three by two cells with a node at the center of each cell. A distributed force was then applied to the plate and the exact force at each node was calculated for both grids. The calculated force on the aerodynamic grid was then splined to the structural grid and these values were compared with the exact values that were calculated. Errors at each structural node varied between 3% and 16%. However, when the forces on the aerodynamic grid and splined structural grid were summed, the total forces were the same. When moments about a point were calculated for both the aerodynamic grid

and the splined structural grid and then summed, the total moments were the same for both grids. The model problem showed that the spline conserves the total forces and moments on a global level, but that errors exist on a cell-by-cell basis.

To characterize the error for a more realistic geometry, the total forces and total moments for both the aerodynamic and structural grids were calculated for the Goland$^+$ Wing (discussed in section 3.2.2) at each time-step during an LCO simulation run. The average error was 0.0003% except for the total moment about the y-axis which had an average error of 0.0078%. The total work was also calculated for each grid. Work was calculated by taking the dot product of the change in force at each node, and the displacement of each node. The results were summed to provide a total work. The work was compared at each time-step for both grids. The difference between the total work calculated on the structural grid, and the total work calculated on the aerodynamic grid varied from -0.1 to 0.17 $N \cdot m$ with an average of 0.0004 $N \cdot m$ (Figure 3.1), or 0.0017%. Overall, there is a very small error in the total moment about the y-axis and in the work induced by the thin-plate spline using these grids for this problem.

3.1   Prescribed Structural Motion Test Case

The Goland$^+$ wing, described in section 3.2.2, was sinusoidally pitched $\pm 0.5°$ at 3 Hz. Coefficients of lift and moment were plotted and compared to Beran et al. [6, 7]. The grid consisted of 678,657 tetrahedral cells. Beran et al. [6] used non-match-point flow conditions. FLUENT requires match-point flow conditions. Therefore it was necessary to change the freestream temperature and pressure conditions in order to match a given Mach number, freestream velocity, and freestream density. The Mach number was set at 0.92, the freestream velocity was set to 400 ft/sec (121.92 m/s), and the freestream density was set to 0.0023771 $slugs/ft^3$ (1.225 kg/m^3). For $\gamma = 1.4$ and $R = 1716.16$ $\frac{ftlb_f}{slug°R}$ ($R = 287.05$ $\frac{Nm}{KgK}$), this gave a freestream temperature of $78.5245°R$ (43.6247 K) and a freestream pressure of 320.9412 lb/ft^2 ($15,366.746$ Pa).
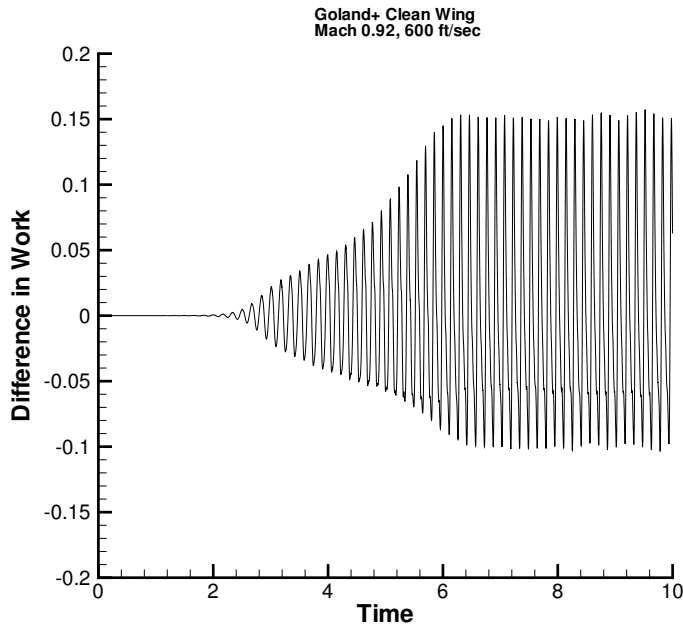
Figure 3.1   Difference in Work $(N \cdot m)$

As shown when plotting the coefficient of moment (C_M) versus the coefficient of lift (C_L) (Figure 3.2), the results from FLUENT compare well to ENS3DAE and CAPTSDv. There was a slight asymmetry in the FLUENT-based results attributed to grid asymmetries introduced as the mesh was deformed. Overall, the results indicated that the aeroelastic program produced similar results to other software used for aeroelastic analysis.

A test was performed to determine the computational impact of moving the grid. The amount of time needed per iteration was compared for a steady state calculation versus an unsteady calculation that called the moving grid routine every iteration. All the force and structural model calculations were performed, but the grid coordinates were not changed so the flow for both solutions was identical. The test was performed on two, four, eight, and sixteen Athlon MP 2600+ processors with 2 GB RAM and a Myrinet network. As shown in Figure 3.3, the aeroelastic
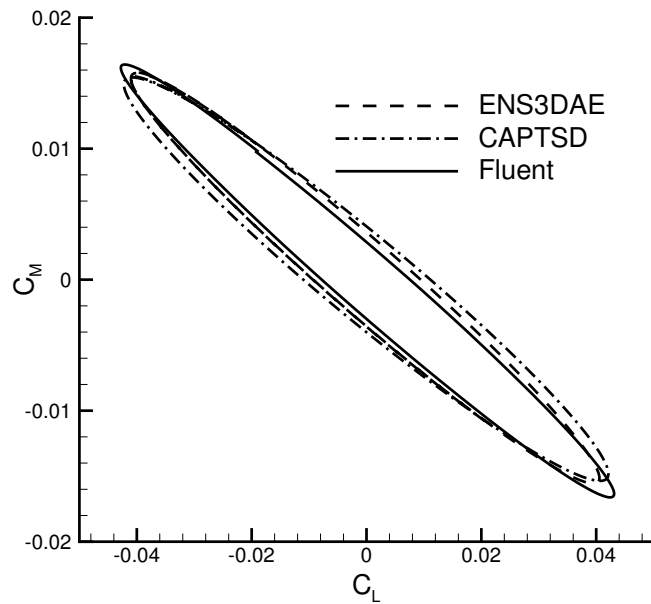
Figure 3.2 $C_L - C_M$ Phase Portrait

code with deforming grid capability had degraded computational efficiency when more than eight processors were used.

3.2 Aeroelastic Structural Motion Test Cases

3.2.1 AGARD 445.6 Wing.   The first 3-D wing to be studied with the full aeroelastic program was the AGARD 445.6 weakened-wing model [57]. This wind tunnel model has been presented as a standard aeroelastic case [57]. Experimental flutter data is available for this wing at several points [57] between Mach 0.499 and Mach 1.141. This test case has often been used to validate aeroelastic programs [27, 38, 40].

This wing consists of a NACA 65A004 airfoil in the streamwise direction with a panel aspect ratio of 1.6525 and a panel taper ratio of 0.6576. The span is 2.5 ft (0.762 m), the root chord is 1.833 ft (0.5587 m), and the tip chord is 1.208 ft (0.3682 m). The quarter chord line is swept 45 degrees (Figure 3.4).
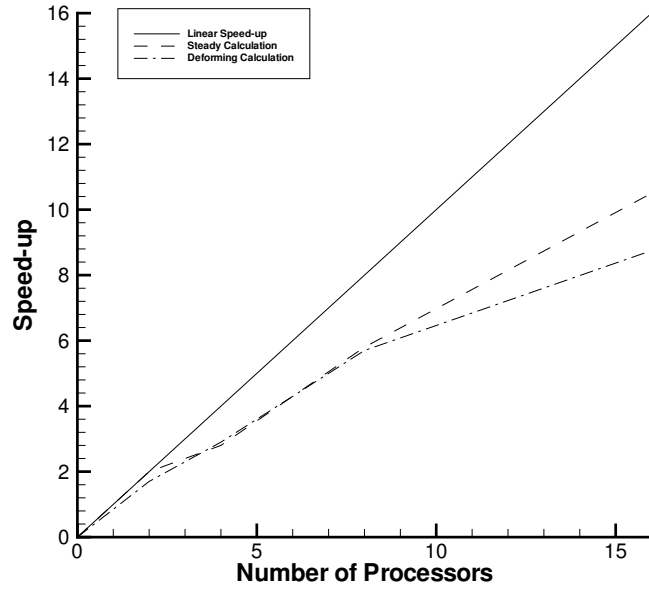
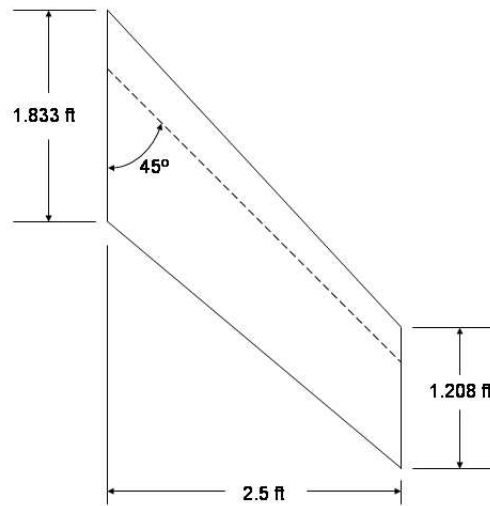Figure 3.3   Computational Impact of Moving Grid
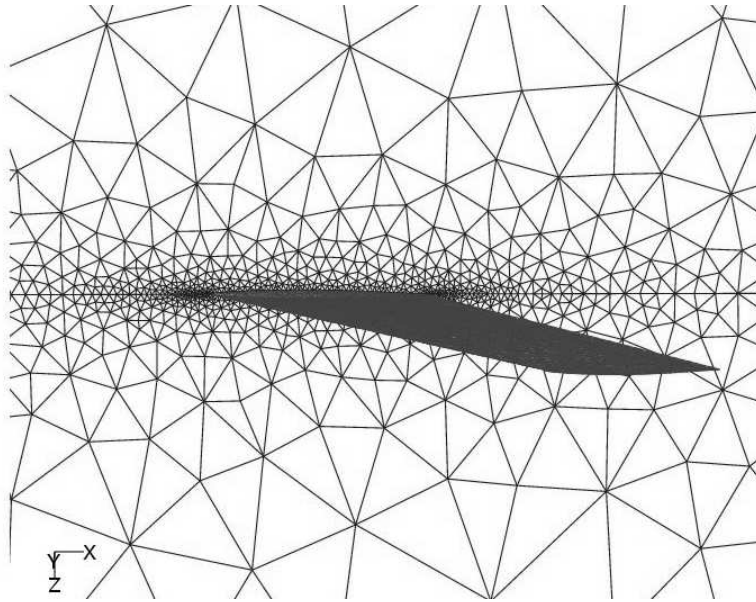

Figure 3.4   AGARD 445.6 Planform

Figure 3.5   AGARD 445.6 Aerodynamic Grid

An ASTROS model, developed by Kolonay [36], was obtained from Gordnier [27] and used in this test. This structural model produced the first fourteen natural vibration modes for the AGARD 445.6 wing.

An unstructured aerodynamic grid consisting of 177,778 tetrahedral cells (Figure 3.5) was created using Gridgen. A calculation of the flutter point was then made using the aeroelastic program. A dynamic pressure was chosen (table 3.1) and the solution was computed for four oscillations. If the oscillations were growing, a lower dynamic pressure was chosen and the solution recomputed. If the oscillations were damped, a higher dynamic pressure was chosen. This was continued until the flutter point was bounded and a dynamic pressure was found that produced neutral oscillations. The point of neutral oscillations was the flutter point.

For this problem, an initial displacement perturbation of 0.01 was given to mode 1. A time step of 0.0003 was also used. A time-step convergence study showed that larger time steps caused the oscillations to grow while smaller time steps did not change the solution. For the AGARD 445.6 wing, computational flutter results are compared by calculating the ratio of the computational flutter dynamic pressure

Table 3.1   AGARD 445.6 Test Conditions for Mach 0.96

q/q_e	Velocity		Temperature		Pressure	
0.8	893 ft/sec	(272 m/sec)	$360°R$	(200 K)	76.02 lb/ft^2	(3639.67 Pa)
1.0	998 ft/sec	(304 m/sec)	$450°R$	(250 K)	95.02 lb/ft^2	(4549.59 Pa)
1.2	1094 ft/sec	(333 m/sec)	$540°R$	(300 K)	114.02 lb/ft^2	(5459.50 Pa)
1.4	1181 ft/sec	(360 m/sec)	$630°R$	(350 K)	133.03 lb/ft^2	(6369.49 Pa)

Table 3.2   Flutter Point Results, Mach 0.96

Method	q/q_e
Gordnier coarse viscous	1.15
Gordnier medium viscous	1.12
Gordnier fine viscous	1.05
Gordnier coarse inviscid	1.02
Gordnier medium inviscid	0.96
Gordnier fine inviscid	0.84
Parker inviscid	**0.86**
Wind-Tunnel Experiment	1.00
Lee-Rausch et al.	0.89
Vermeersch et al.	1.47

(q) over the experimental dynamic pressure (q_e). Using the aeroelastic program, at Mach 0.96, a flutter point of $q/q_e = 0.86$ and a flutter frequency of 12.65 Hz was calculated. This compares well with Gordnier's fine inviscid grid results as shown in table 3.2 [27].

3.2.2   Goland$^+$ Wing.   The second 3-D wing to be studied was the Goland$^+$ wing. The Goland$^+$ is a variant of the heavy Goland wing developed as a transonic flutter test case by Eastep and Olsen [19]. Based on the original Goland wing [25], the heavy Goland wing has increased mass to ensure applicability in the transonic regime. The Goland$^+$ version of the heavy Goland wing was modelled with a box structure beam to allow a variety of store attachment options [7]. This wing was selected as a test case because data for ENS3DAE and CAPTSDv exists for this configuration [6, 7, 51].

The Goland$^+$ wing is rectangular and cantilevered from an infinite midplane. The wing semi-span is 20 ft (6.096 m) and the chord (c) is 6 ft (1.8288 m). The thickness, τ, is 0.04 ft (0.01219 m). The elastic axis is located 2 ft (0.6096 m) from the leading edge. The airfoil section is constant over the spanwise extent of the wing and is a symmetric, parabolic-arc airfoil given by

$$z = \pm 2\tau(1 - \frac{x}{c})(\frac{x}{c}). \tag{3.1}$$

As reported by Beran et al. [7] and Snyder et al. [51], the Goland$^+$ wing-box structure (Figure 3.6) is made up of shear elements representing three spars evenly spaced 2 ft (0.6096 m) apart, and 11 ribs evenly spaced 2 ft (0.6096 m) apart. Each rib and spar is 4 in (0.1016 m) high. Each of the 20 cells created by the ribs and spars are capped with an upper and lower wing skin membrane element. Rods are added on the top and bottom of each shear element and at every spar/rib intersection. These 137 rod elements represent 60 spar caps, 44 rib caps, and 33 posts. Every element is modelled using the fictional material properties shown in table 3.3 [51]. These properties were selected to match the structural dynamic characteristics of the wing-box model to those of the beam model of the heavy Goland wing [19]. The elements were sized to minimize the differences between the first three natural frequencies. The resulting element dimensions are shown in table 3.4 [51]. The mass properties are modelled by placing lumped masses with no rotational inertia at each grid point [51]. The internal ribs were modelled with lumped masses of 1.9650 slugs (28.6768 kg) at each leading edge spar, 3.9442 slugs (57.5609 kg) at each center spar, and 5.3398 slugs (77.9280 kg) at each trailing edge spar. The masses on the root and tip ribs are half those of the internal ribs. In order to match the LCO results as presented by Snyder et al. [51], a tip store was added to the structure. The tip store is 10 ft (3.048 m) long and is modelled as a series of rigid bar elements. The bar is positioned 6 in (0.1524 m) outboard of the wing tip and extends 3 ft (0.9144 m) in front of the wing leading edge and 1 ft (0.3048 m) behind the trailing edge. The tip
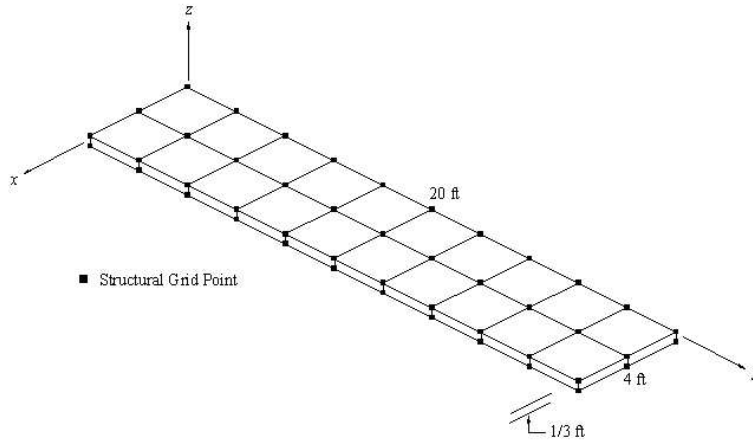
Figure 3.6   Goland$^+$ Structural Model

Table 3.3   Goland$^+$ Material Properties

| Parameter	Value
Young's Modulus, E	$1.4976x10^9$ $slugs/ft^2$ ($2.3525x10^{11}$ kg/m^2)
Shear Modulus, G	$5.616x10^8$ $slugs/ft^2$ ($8.822x10^{10}$ kg/m^2)
Structural Density ρ_s	0.000001 $slugs/ft^3$ (0.0005154 kg/m^3)

store has a mass of 22.498 slugs (328.3313 kg) located 1.75 ft (0.5334 m) forward of the elastic axis and a rotational inertia of 50.3396 slugs-ft^2 (68.2509 kg-m^2) [51].

Natural vibration modes for the Goland$^+$ wing with a tip mass were obtained from MSC/NASTRAN [6, 51]. The first six modes were used in the aeroelastic analysis. These modes are plotted in Figure 3.7, which shows the top of the right wing with the leading edge to the upper right and the trailing edge to the lower left.

The aeroelastic code was tested on a coarse, unstructured, tetrahedral grid made up of 68,949 cells with 518 cell faces on the wing itself. This grid was purposefully created very coarse in order to decrease the run times for initial testing of the aeroelastic program. The program was run at multiple Mach numbers and velocities in order to calculate the flutter stability boundary. The Goland$^+$ simu-

Table 3.4   Goland⁺ Element Dimensions

| Elements	Dimensions
Upper and lower wing skin thickness	$0.0155 ft$ $(4.7244x10^{-3}m)$
Leading and trailing edge spar thickness	$0.0006 ft$ $(1.8288x10^{-4}m)$
Center spar thickness	$0.0889 ft$ $(2.7097x10^{-2}m)$
Rib thickness	$0.0347 ft$ $(1.0577x10^{-2}m)$
Post area	$0.0008 ft^2$ $(7.4322x10^{-5}m^2)$
Leading and trailing edge spar cap area	$0.0416 ft^2$ $(3.8648x10^{-3}m^2)$
Center spar cap area	$0.1496 ft^2$ $(1.3898x10^{-2}m^2)$
Rib cap area	$0.0422 ft^2$ $(3.9205x10^{-3}m^2)$
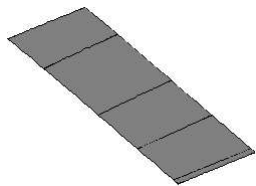
(a) Mode 1 (1.69 Hz)
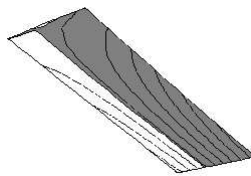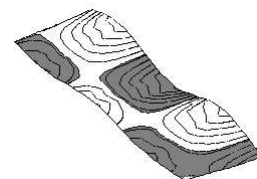
(b) Mode 2 (3.05 Hz)
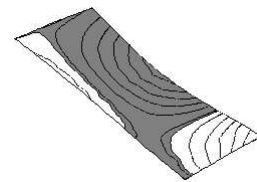
(c) Mode 3 (9.17 Hz)
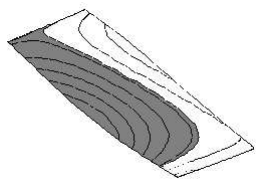
(d) Mode 4 (10.8 Hz)
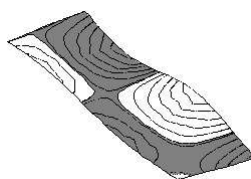
(e) Mode 5 (16.3 Hz)

(f) Mode 6 (22.8 Hz)

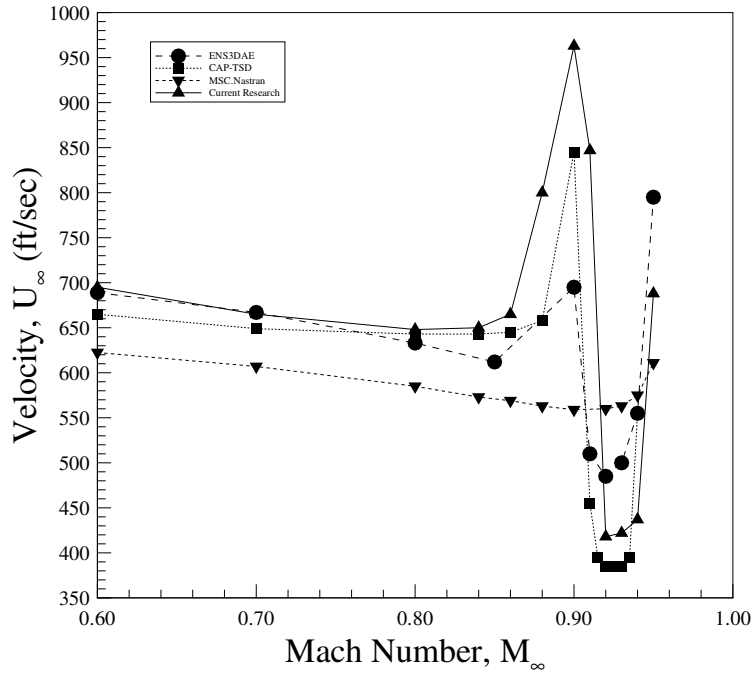Figure 3.7   Mode Shapes for Goland⁺ Wing with Tip Store

Figure 3.8   Goland$^+$ Stability Boundary

lations were started by giving mode 2 a modal displacement perturbation of 0.02. These results were then compared to the results presented by Snyder, et al. [51]. Snyder, et al. [51] used non-match-point flow conditions for their analysis. For each test case, they chose a Mach number and velocity, and fixed the far-field density and temperature values at standard-day, sea-level conditions. In order to match their flow parameters in FLUENT, the specific gas constant R and the far-field pressure were varied for different Mach number and velocity settings. The specific heat ratio, γ, was held fixed at 1.4. The computed stability boundary is shown in Figure 3.8. For an extremely coarse grid, it compares well with the results presented by Snyder, et al. [51].

At 600 ft/sec (182.88 m/sec) and Mach 0.92, the dynamic pressure is beyond the flutter point and was shown by Snyder, et al. [51] to result in LCO. At these conditions and with a time step of 0.001 seconds, the aeroelastic program did produce LCO with a frequency of 3.37 Hz. A time-step convergence study showed that larger
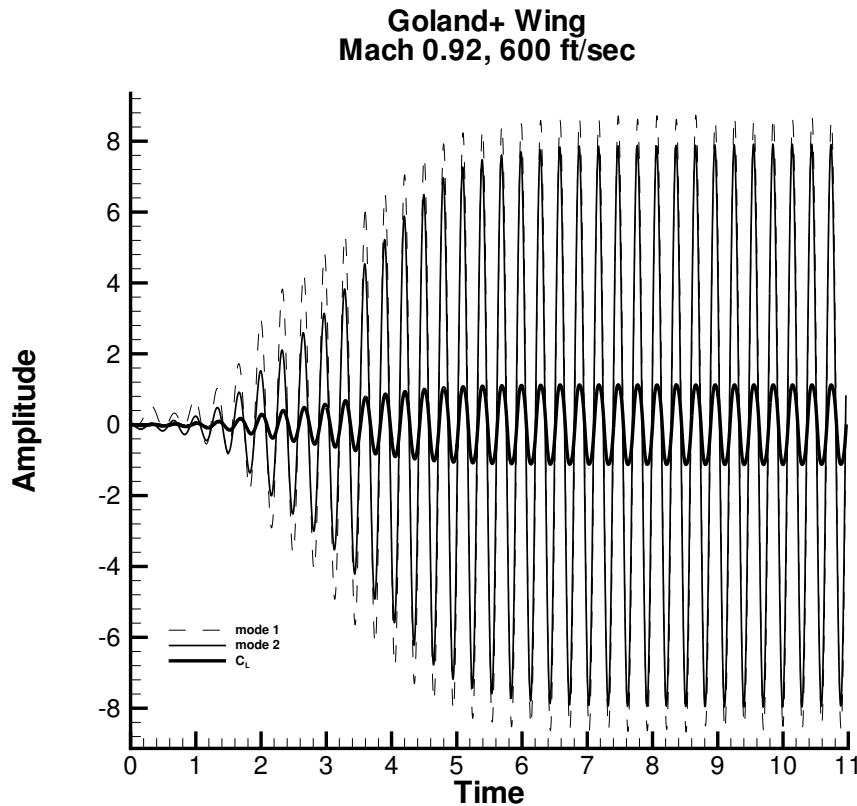
Goland+ Wing
Mach 0.92, 600 ft/sec

Figure 3.9   Goland$^+$ Coarse Grid Amplitudes

time steps caused the oscillations to damp while smaller time steps did not affect the solution. It took 3 hours and 17 minutes to produce one second of data using eight 2.2 GHz opteron processors. Mode 1 and mode 2 amplitude time histories as well as C_L time history are shown in Figure 3.9. These tests showed that the aeroelastic program was capable of modelling LCO.

3.3   Validation Summary

An aeroelastic program based on a fully unstructured-grid formulation capable of simulating flutter and LCO was successfully developed by integrating a modal structural model with FLUENT 6.1. The individual parts of the aeroelastic code such as the splines and structural model were validated to ensure they produced the

correct results. The transfer of forces from the aerodynamic grid to the structural grid was critical for the accurate calculation of wing deformations. The thin-plate spline was therefore tested for both a flat plate and with the Goland$^+$ wing to obtain an estimate of the errors induced by the spline. It was found that there was an error induced but on average it was less than 0.0078%.

Prescribed motion results showed that the aeroelastic program produced lift and moment results similar to those produced by other aeroelastic analysis codes. Validation testing with the AGARD 445.6 flutter test case showed that the aeroelastic program performed well predicting flutter onset velocity and frequency. Finally, initial testing of the Goland$^+$ LCO test case showed that the program correctly predicted LCO behavior.

IV. Analysis of Goland⁺ LCO

4.1 Computational Experiment Setup

The aeroelastic program was used to analyze the LCO of the Goland⁺ wing described in section 3.2.2. Four inviscid grids and one viscous grid were built to look at grid convergence (Appendix C) for both steady solutions at angles-of-attack from 0 to 20 degrees, and for unsteady LCO solutions. Based on the results of this study, it was determined that the computational expense was prohibitive for viscous LCO simulations. All Goland⁺ LCO simulations were therefore computed using the inviscid solver. Based on the results of the grid convergence study, the clean Goland⁺ results presented in section 4.2 were obtained from an inviscid grid which consisted of 194,780 tetrahedral cells with 9,178 cell faces on the wing.

At 600 ft/sec (182.88 m/sec) and Mach 0.92, the dynamic pressure was beyond the flutter point and was shown by Snyder, et al. [51] to result in LCO. For the Goland⁺, these flow conditions fell within the transonic flutter dip region. To match the conditions of Snyder, et al. [51], the far-field density, temperature, and pressure were set to 0.0023771 $slugs/ft^3$ (1.225 kg/m^3), 518.67°R (288.15 K), and 722.1813 lb/ft^2 (34578.04 Pa) respectively, while R was set to 585.7438 $\frac{ft \cdot lb_f}{slug \cdot °R}$ (97.951 $\frac{N \cdot m}{Kg \cdot K}$). These flow parameters were used for all the clean wing and store simulations in this study.

All of the Goland⁺ simulations used a time step of 0.001 seconds corresponding to approximately 300 time steps per cycle. To check for time-step convergence, a time step of 0.0005 was tested. Cutting the time step in half changed the mode 1 response by 0.367%, the mode 2 response by 0.027%, the C_L response by 0.029%, and the frequency by 0.160%. These changes were sufficiently small that the time step of 0.001 seconds was considered converged.

To determine the role of store aerodynamics in LCO, grids for various store configurations were created and used with the same structural model used by the

clean wing. Therefore, in these cases, the stores were modelled aerodynamically but not structurally. The tip mass was retained in the structural model because it was necessary for the clean wing to obtain LCO. The grids were created by starting with the clean grid of 68,949 tetrahedral cells with 518 cell faces on the wing, and then adding store shapes.

Under-wing and tip stores were added to the Goland$^+$ wing and the same initial perturbation and boundary conditions were used as for the clean wing. Under-wing stores can be added to the Goland$^+$ wing at any rib station. These stations are evenly spaced 2 ft (0.6096 m) apart. Aerodynamic forces and moments were calculated for the store at the point the pylon joined the wing on the elastic axis. These forces and moments were transferred into the structural model at this point. Under-wing stores were added at 20% (4 ft (1.2192 m)), 50% (10 ft (3.048 m)), and 80% (16 ft (4.8768 m)) half-span. The under-wing configurations consisted of the Goland$^+$ grid with a 10 ft (3.048 m) long, 12 in (0.3048 m) diameter cylindrical store with an elliptic nose cone centered below the wing. The top of the store was located 12 in (0.3048 m) below the bottom of the wing and was attached to the wing via a biconvex-shaped pylon that was 3 ft (0.9144 m) long centered chordwise under the wing. The grid with a tip store consisted of the Goland$^+$ grid with a 10 ft (3.048 m) long, 5 in (0.127 m) diameter cylindrical store with an elliptic nose cone centered on the wing tip. These four configurations are shown in Figure 4.1.

Additional store configurations were also analyzed in order to determine how store modifications change the store forces or change the interference on the bottom of the wing. These additional configurations included the addition of fins to the stores, changes in pylon height, fore/aft movement of the stores, changes in store diameter, and multiple stores. The effect fins on stores had on LCO was examined by adding fins to the tail of the stores for the four store configurations. The pylon height effect was studied by changing the height from 12 in (0.3048 m) to 6 in (0.1524 m). The effect of stream-wise positioning of the store was examined by modifying the
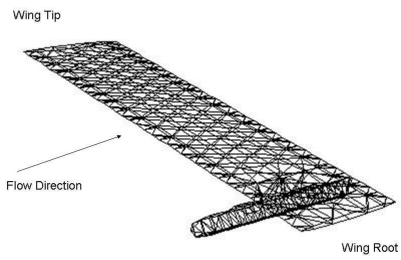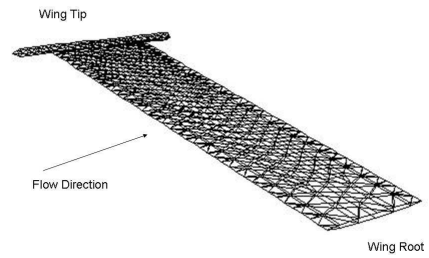
(a) Goland$^+$ 20% Half-span Under-wing Store
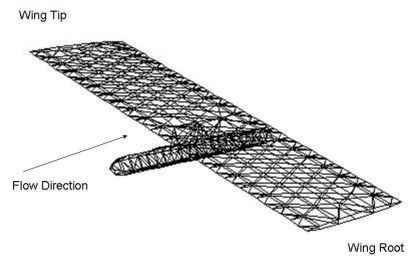
(b) Goland$^+$ 50% Half-span Under-wing Store
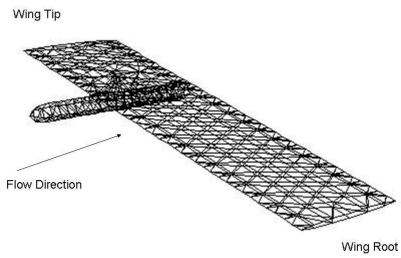
(c) Goland$^+$ 80% Half-span Under-wing Store

(d) Goland$^+$ Tip Store

Figure 4.1   Goland$^+$ Wing with Aerodynamic Stores Surface Grids

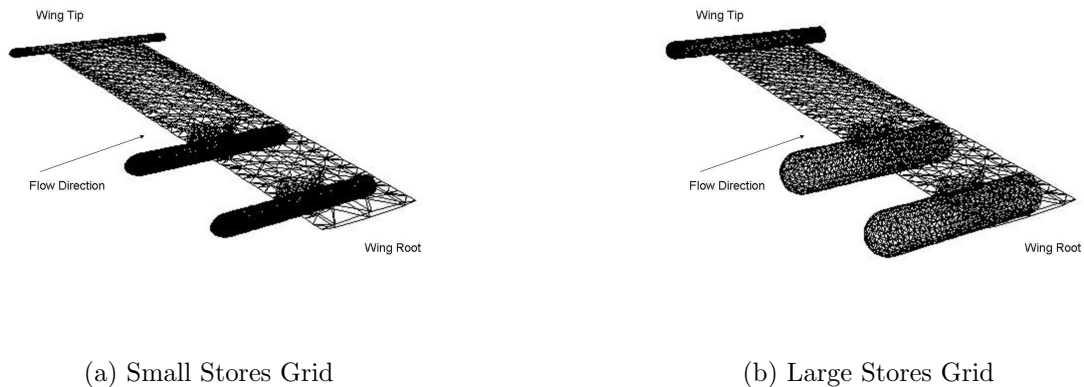(a) Small Stores Grid   (b) Large Stores Grid

Figure 4.2   Goland$^+$ with Multiple Stores Surface Grids

position of the under-wing store grids by shifting the stores 2 ft (0.6096 m) fore and aft, while the 12 in (0.3048 m) pylon remained centered beneath the wing. The effect store diameter had on LCO was examined by doubling the under-wing store diameter to 24 in (0.6096 m) and the tip store diameter to 10 in (0.254 m). Finally, multiple, small-diameter stores were added to the Goland$^+$ wing to create further interference on the bottom of the wing. The tip store and the under-wing stores at 20% and 50% half-span, were added to the Goland$^+$ wing (Figure 4.2a). This was repeated for the large diameter stores (Figure 4.2b).

Inertial forces were added to the stores in order to determine the relative importance of store aerodynamics versus store mass. The inertial forces were calculated based on a mass of 25 slugs (364.8476 kg) located a fixed distance from the elastic axis. The configurations with a 12 in (0.3048 m) diameter under-wing store centered on a 12 in (0.3048 m) pylon and the 5 in (0.127 m) diameter tip store were run with a store mass located -2 ft (-0.6096 m), -1 ft (-0.3048 m), 0 ft (0.0 m), 1 ft (0.3048 m), and 2 ft (0.6096 m) in the x-direction (stream-wise direction) from the elastic axis.

4.2 Clean Goland$^+$ Wing Results

The LCO for the Goland$^+$ clean-wing configuration consisted of a nearly in-phase coupling of mode 1 and mode 2 which produced a single-degree-of-freedom, torsional motion, with an axis of rotation running from the elastic axis at the wing root to a point slightly forward of the leading edge at the wing tip. The LCO had an amplitude of ± 1.065 for C_L (Figure 4.3), ± 0.47 for C_M, and ± 20.6 degrees for the tip angle-of-attack. There was significant hysteresis in C_M as shown in Figure 4.5. This was expected because LCO is a non-linear phenomenon. If it were linear with no hysteresis, C_M versus angle-of-attack would form a straight line. The two dominant modes had an amplitude of ± 8.8 for mode 1 and ± 7.5 for mode 2 (Figure 4.3). The amplitude of mode 3 was ± 0.66 which was only 7.5% of the contribution of mode 1. The remaining modes contributed even less. A power-spectral-density plot of the motion showed that the power was primarily at 3.3 Hz and 9.8 Hz with some contribution from 6.5 Hz and 10.7 Hz (Figure 4.4). The dominant modes in the LCO response were mode 1 followed closely by mode 2. However, the dominant forces were mode 1 followed by mode 4. The remaining force contribution was in mode 3, mode 5, then finally mode 2 and mode 6 (Figure 4.6).

The only nonlinearity present was due to the existence and movement of shocks. There was no separation (inviscid flow) and no structural nonlinearity. The shock was initially located at approximately 80% chord where it ran from the wing root, to the wing tip, with a slight curve forward before disappearing at the wing tip (Figure 4.7). As the wing began to deform, the shock started to slowly move fore and aft sinusoidally (type-A shock motion [56]). As the amplitude of the wing motion increased, the magnitude of the shock strength changed periodically with the motion until the shock disappeared during part of its aft motion (type-B shock motion [56]). Transition from type-A to type-B was observed at approximately 2.9 seconds, ranging from the wing root to about 50% span. The shock motion for the outboard 50% span remained type-A. The inboard type-B shock motion limited the energy flow
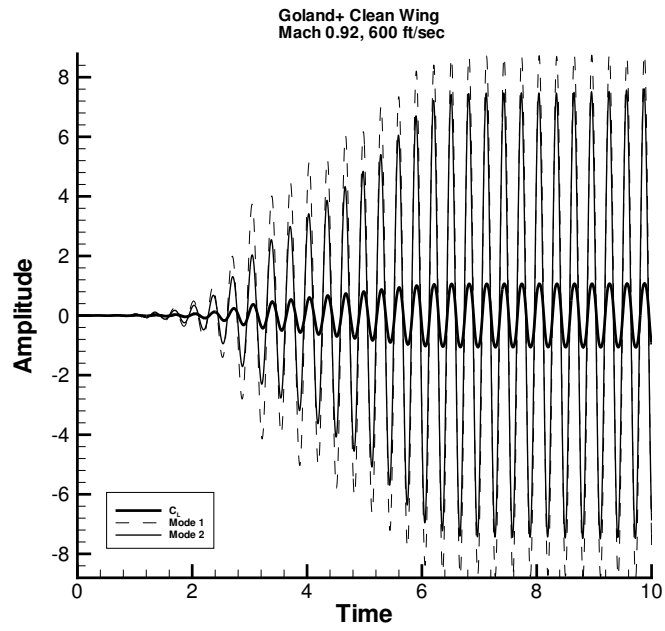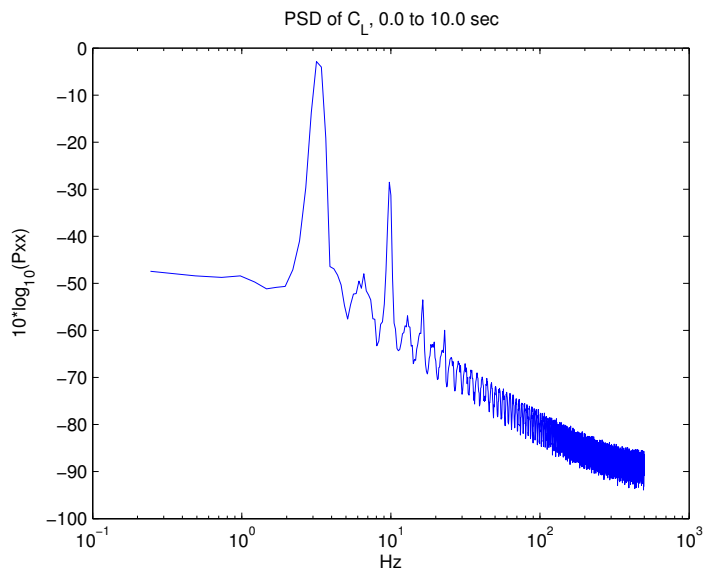
Figure 4.3　Clean Wing C_L and Modal Amplitudes
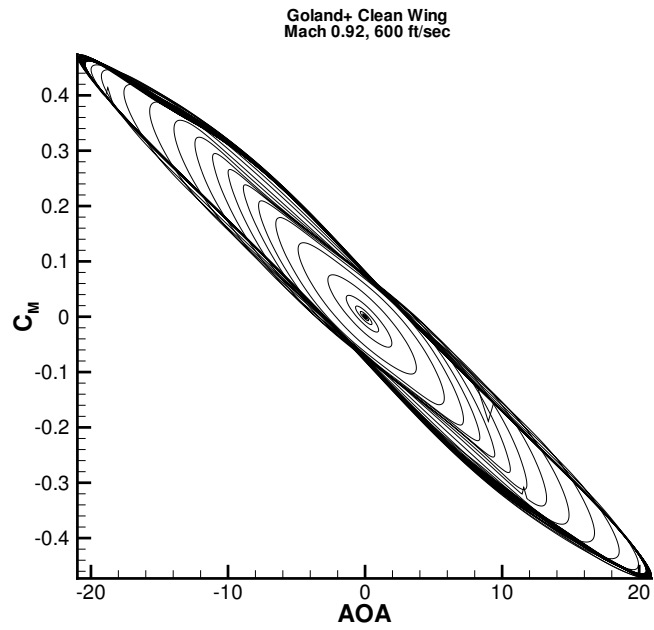

Figure 4.4　Clean Wing PSD

Goland+ Clean Wing
Mach 0.92, 600 ft/sec

Figure 4.5   Clean Wing C_M vs Angle-of-Attack

Goland+ Clean Wing
Mach 0.92, 600 ft/sec
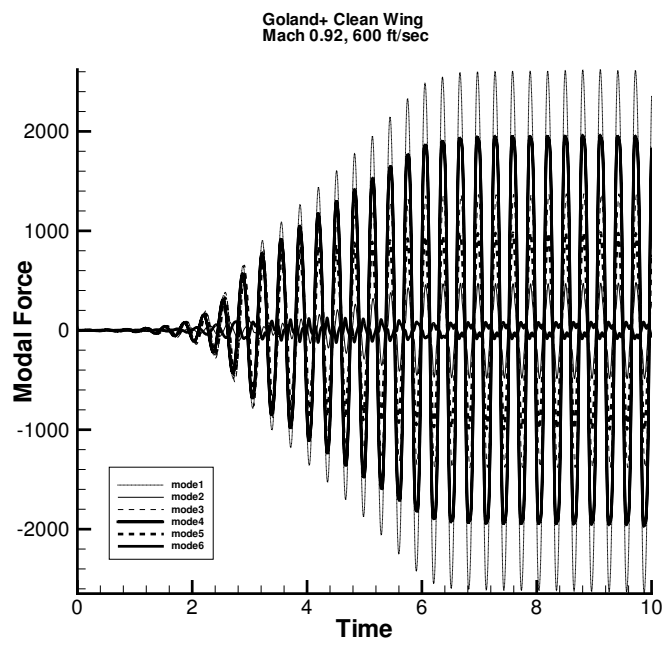
Figure 4.6   Clean Wing Modal Force Amplitudes

4-7

Flow Direction

Wing Root

Wing Tip

Normal Shock

Density
0.300   0.675   1.05   1.42   1.80
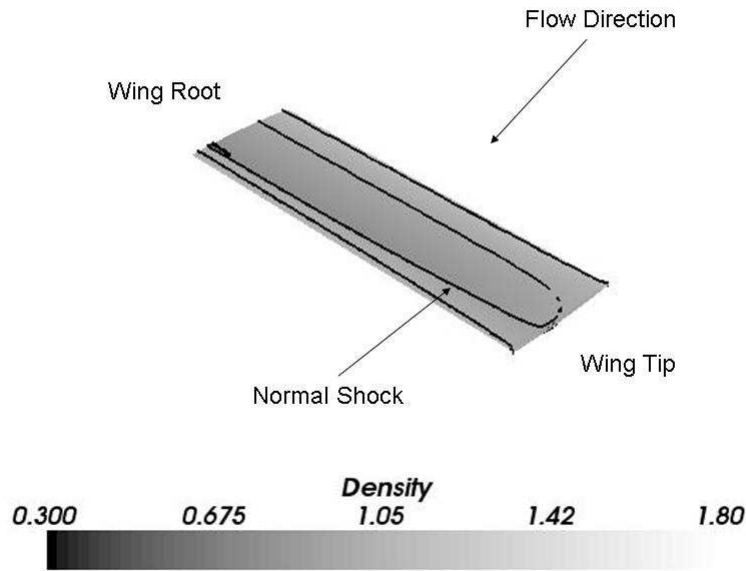
Figure 4.7   Steady State Density Contours

and changed the mode 1 amplitude growth from an exponential growth to a linear growth, as seen in Figure 4.3. This type-B motion continued to gain strength until it consisted of an appearing and disappearing shock at the trailing edge with no observable fore/aft motion. However, this type-B shock motion was only on the inboard 50% span. Most of the energy flowing into the structure was occurring on the outboard 50% span. At approximately 4.6 seconds, a periodic lambda shock began to appear and disappear near the wing tip in conjunction with a strong normal shock moving fore and aft at the trailing edge. This lambda shock and normal shock further limited the energy transferred from the fluid to the structure. At 6.4 seconds, the wing was in LCO. The combination of type-B shock motion, lambda shock motion, and trailing-edge normal-shock motion were responsible for quenching the energy flow from the fluid to the structure resulting in LCO for this wing.

The coupling of mode 1 and mode 2 into a single-degree-of-freedom, torsional motion about a point ahead of the leading edge, leads to a wing twisting motion such

that the aerodynamic forces on the wing are constantly pushing the wing toward the static aeroelastic position. When the wing bends down and twists up, the aerodynamic forces try to restore the wing to its static aeroelastic position. However, the restoring forces are large enough that the amount of energy transferred into the wing causes the wing to overshoot its neutral point, bending and twisting even further in the opposite direction, leading to a growing oscillation. When the oscillations grow to the point that the trailing-edge shock and lambda shock appear near the wing tip, the shocks limit the force on the wing, thereby limiting the overshoot. When the shock strength reaches the point that it balances the inertial forces, a stable LCO is achieved. Figure 4.8 illustrates the pressure distribution on the wing. If the normal shock and lambda shock were not present, the coefficient of pressure (C_P) on the top of the wing would be lower. The net force on the wing would therefore be higher, leading to the wing bending and twisting further in each subsequent cycle.

During a LCO cycle (Figure 4.9), the wing starts bending down and twisting up. A normal shock appears near the trailing edge on the outboard portion of the wing (Figure 4.9a). This normal shock increases the pressure on top of the wing and begins to limit the flow of energy from the fluid into the wing. As the wing continues to bend down and twist up, a lambda shock appears near the tip (Figure 4.9b). When the lambda shock first appears, it runs from the leading edge of the wing near the tip to where the trailing-edge normal shock meets the trailing edge near 50% span. As the wing continues to bend down and twist up, the lambda shock strengthens and the shock angle increases. At the extreme of the wing motion, the lambda shock runs from the leading edge of the wing near the tip, to the center of the normal shock at the trailing-edge, at approximately 75% span (Figure 4.9c). As the wing then begins to straighten and untwist, the lambda shock reverses direction and the shock angle begins to decrease. The normal shock at the trailing edge also begins to weaken and move aft (Figure 4.9d). At the end of the the first half of the LCO cycle, the shocks are completely gone and the forces on the top and bottom of the
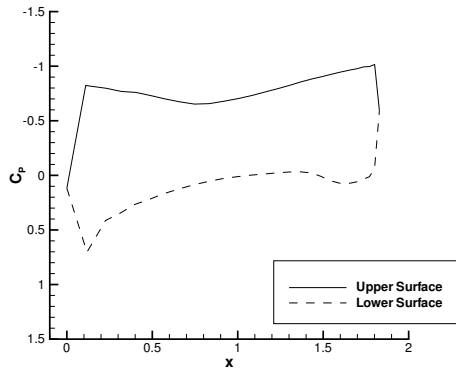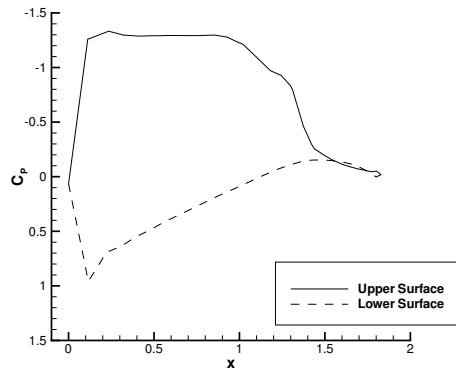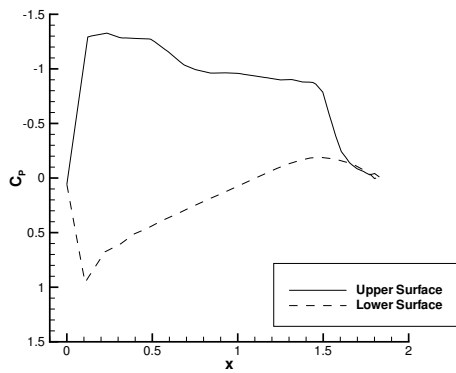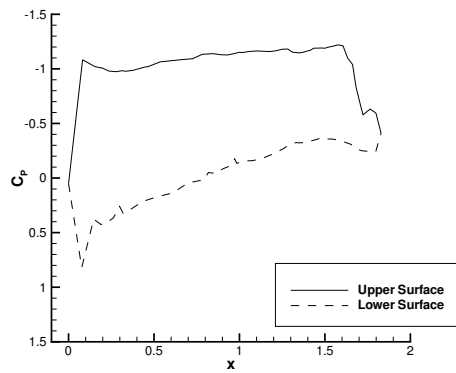
(a) 2m span
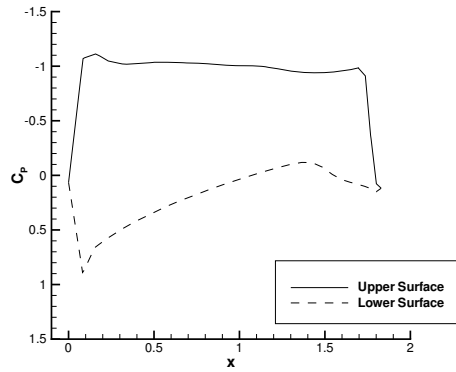
(b) 3m span
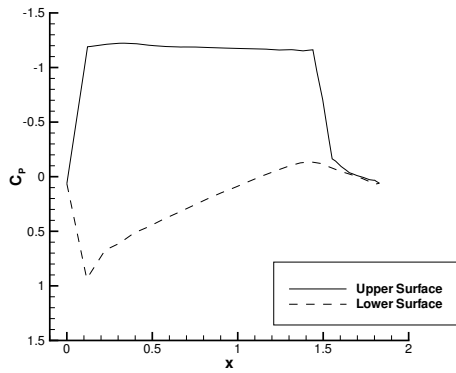
(c) 4m span

(d) 5m span

(e) 5.5m span

(f) 6m span

Figure 4.8   Clean Wing at 6.815 Seconds (Pressure Distribution)

wing are nearly balanced (Figure 4.9e). This is repeated for the second half of the LCO cycle when the wing starts to bend up and twist down.

Figure 4.10 shows the steady pressure contours for a rigid wing at 20 degrees angle-of-attack. The forces on the rigid-wing airfoil section are much higher than those shown in Figure 4.8e, even though the angle-of-attack at the tip is approximately the same. This difference in force is because of the shocks, which provide the quenching mechanisms responsible for LCO in this wing. The normal shock and lambda shock do not appear if the wing is given a constant angle-of-attack. However, if the wing is deformed into the bent and twisted shape that occurs during LCO and a steady-state flow solution is computed, the lambda and trailing-edge shocks are present. These shocks are present because of the shape of the wing and not because of the dynamic motion of the wing. The dynamic motion does, however, play a role in the shock strength and movement. The shocks are weaker and slightly aft when computed for steady-state flow versus those computed for dynamic motion. The coupling of the primary bending and twisting modes is what leads to this deformed shape, which in turn leads to shock motion that provides the energy quenching necessary for LCO. The aerodynamic forces dictate how fast the oscillations grow and the final amplitudes, not whether LCO exists. This was further demonstrated by changing the airfoil on the Goland$^+$ wing in order to change the aerodynamic forces (Appendix D).

If a wing is undergoing LCO, a phase plot will trace an orbit along a closed path and there will be zero net work over a cycle [5]. For the clean-wing configuration, plunge rate versus plunge was plotted for the point where the elastic axis intersects the wing tip. This plunge phase plot, shown in Figure 4.11a, shows the growth of the amplitudes culminating in a closed path indicating LCO. The pitch rate of the wing tip was also plotted versus pitch. This pitch phase plot, shown in Figure 4.11b, also shows the growth of the amplitudes culminating in LCO. Because the LCO motion appears to be a single-degree-of-freedom, torsional motion, the work being done on
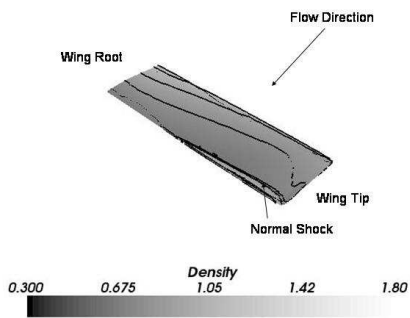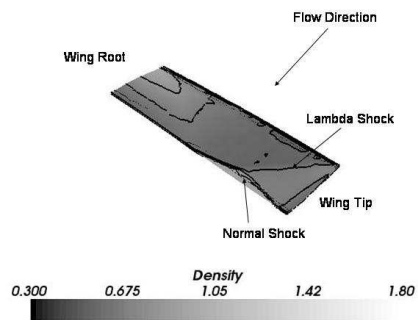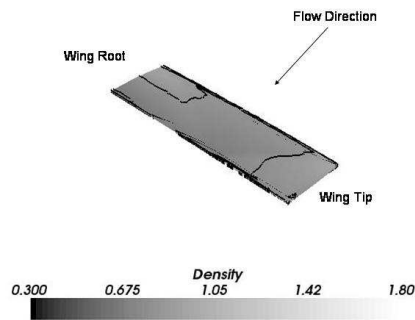
(a) 6.760 Seconds
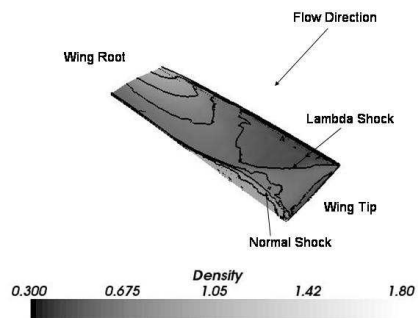
(b) 6.790 Seconds
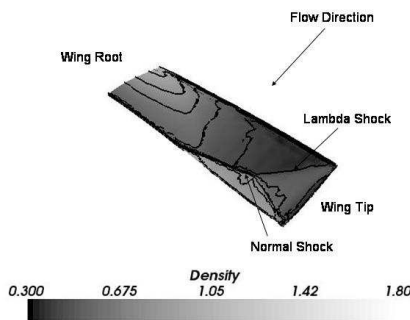
(c) 6.815 Seconds

(d) 6.870 Seconds

(e) 6.890 Seconds

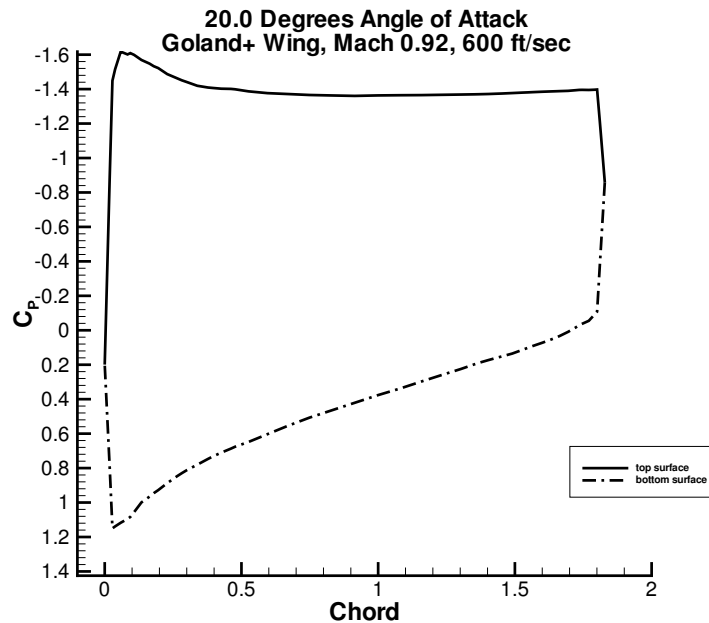Figure 4.9   Clean Wing (Density Contours)

Figure 4.10   Rigid Wing Airfoil C_P plot for 20 degrees Angle-of-Attack

the wing by the fluid can be compared with the wing-tip angle-of-attack. As can be seen in Figure 4.12, whenever the wing is twisting away from zero degrees, work is being done on the fluid, and whenever the wing is twisting toward zero degrees, work is being done on the structure. This results in two work cycles per LCO cycle. There is a 5-degree phase lag between the work and angle-of-attack. This is because the bending mode (mode 1) lags the torsion mode (mode 2) by 5 degrees (Figure 4.3). Integrating the work over an LCO cycle should result in zero net work. However, for this case, the work did not sum to zero. There was an error of 0.05% of the total work done. This was because the thin-plate spline did not conserve energy across the grid boundaries.

4.3   Goland+ Wing with Under-Wing Stores Results

One of the goals of this study was to determine the role of store aerodynamics in LCO. It was found that aerodynamic store shapes affect LCO in two offsetting
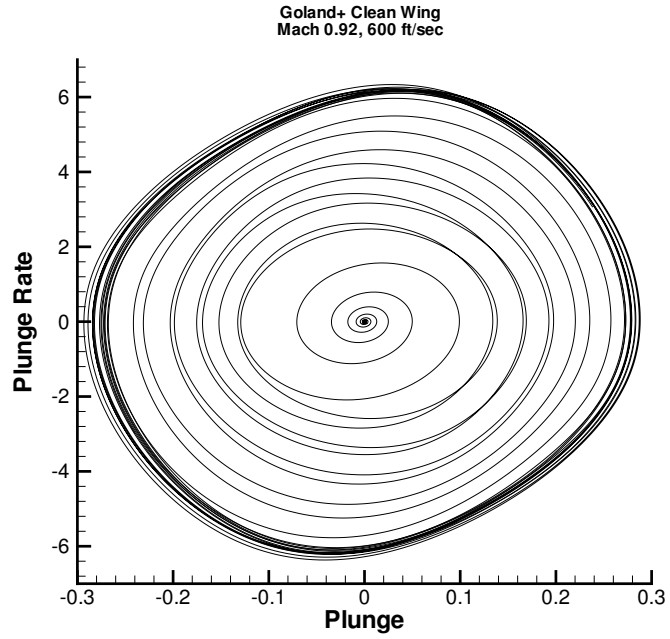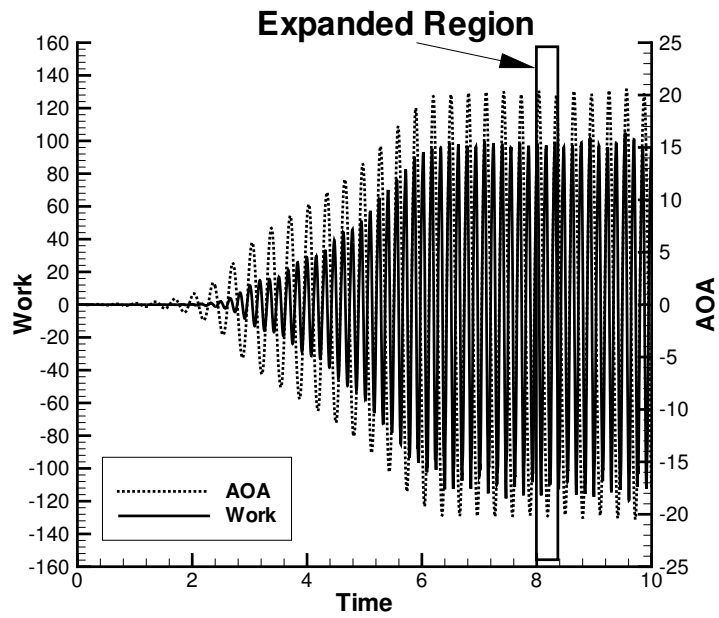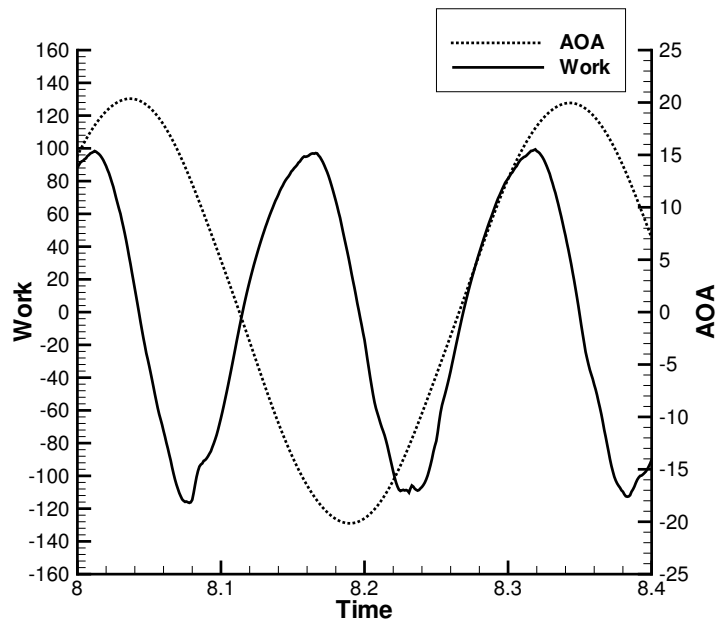
(a) Plunge Phase Plot (Wing Tip)
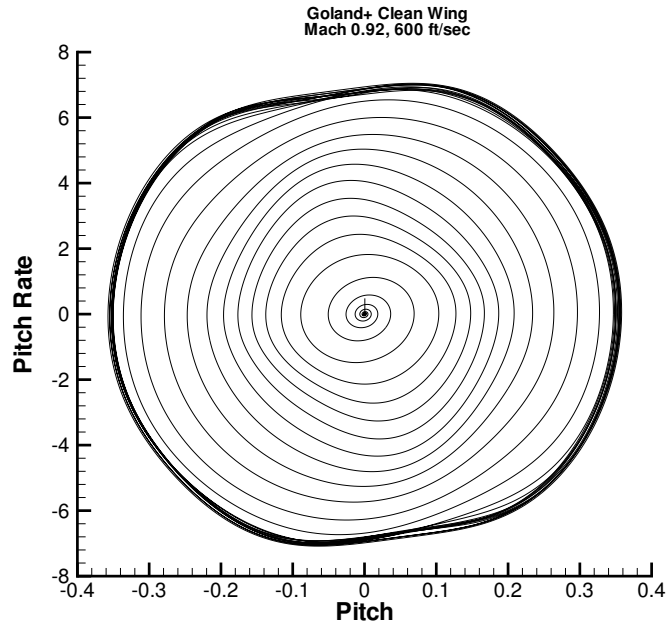
(b) Pitch Phase Plot (Wing Tip)

Figure 4.11   Clean Wing Phase Plots

(a) Work $(N \cdot m)$ on Structure for 10 seconds

(b) Work $(N \cdot m)$ on Structure for One LCO Cycle (Expanded Region)

Figure 4.12   Work on Goland$^+$ Structure (Clean Wing)

4-15

Table 4.1   Effect of Under-Wing Stores on Peak Values

|	20% half-span	50% half-span	80% half-span
C_L	1.10%	4.08%	1.28%
Tip AOA	1.12%	4.96%	2.56%
Mode 1 Force	1.48%	5.22%	0.28%
Mode 2 Force	13.69%	25.15%	14.93%
Mode 3 Force	2.44%	1.01%	1.73%
Mode 4 Force	0.50%	1.96%	0.57%

ways: by interfering with the flow field on the wing surface, and by transferring additional store forces into the structure. The under-wing stores interfere with the airflow on the lower surface of the wing which decreases LCO amplitudes, whereas, store forces transferred into the wing structure directly increase LCO amplitudes.

The further outboard the store was placed, the greater the angle-of-attack experienced by the store. This resulted in higher store loads and increased LCO amplitude. An exception to this was found at the 50% half-span location (Figure 4.13). Small stores with the 12 in (0.3048 m) pylon were placed at 20%, 50%, and 80% half-span locations as discussed in section 4.1. Adding stores increased the mode 2 response in all cases. The mode 1 response decreased for stores at 20% and 80% half-span and increased for stores at 50%. It was speculated that this increase was because of the mode 3 mode-shape (Figure 3.7) which had large displacements in the middle of the wing. Further weight was added to this speculation by observing that the stores primarily contributed to mode 3 forces implying that the store located where mode 3 provided the greatest deformation had the greatest effect. Adding the under-wing stores increased the magnitude of the total modal forces, the magnitude of C_L, and the magnitude of the tip angle-of-attack (Table 4.1). These changes resulted in LCO being reached more quickly than with a clean wing.

For the 20% and 80% half-span configurations, the stores only contributed 0.2% of the peak force in mode 3. The 50% store contributed 0.7% of the peak force in mode 3. To increase these store forces, fins were added to the tail of all
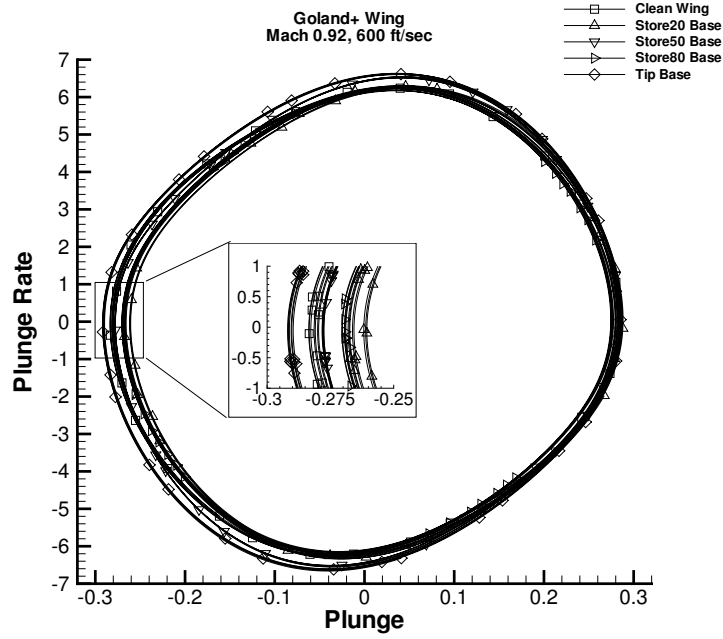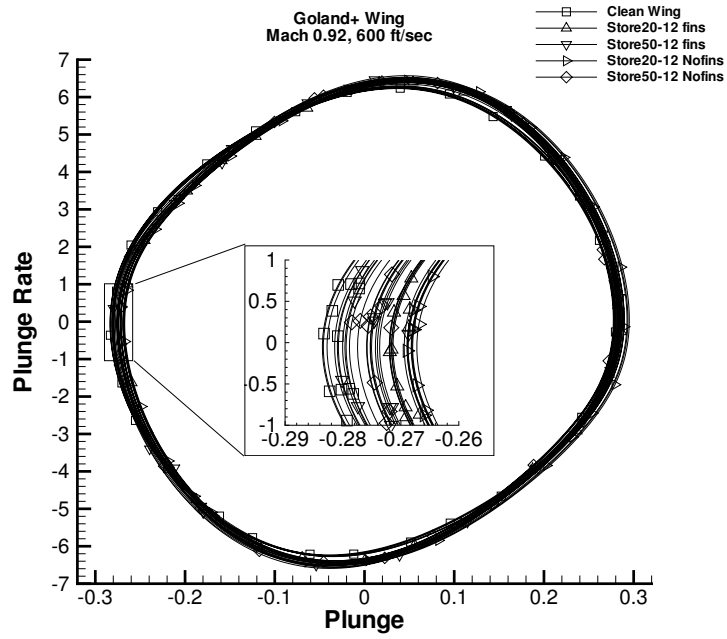
(a) Plunge Phase Plot (Wing Tip)
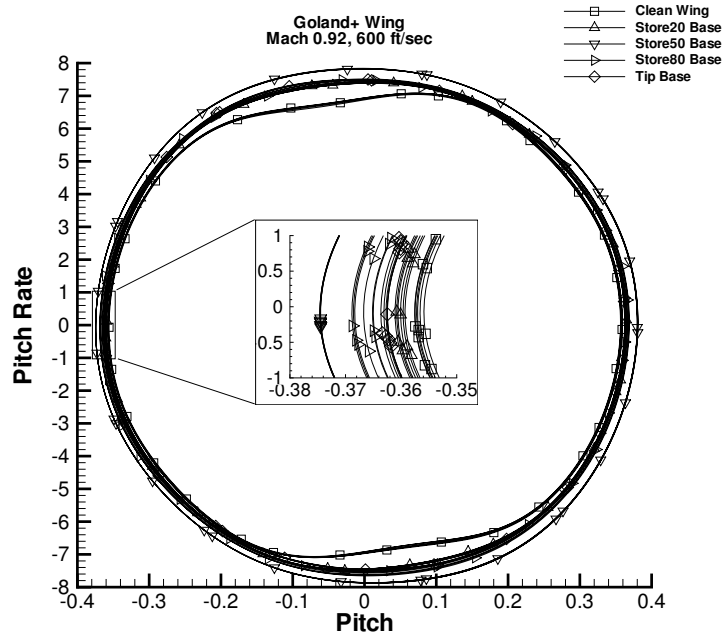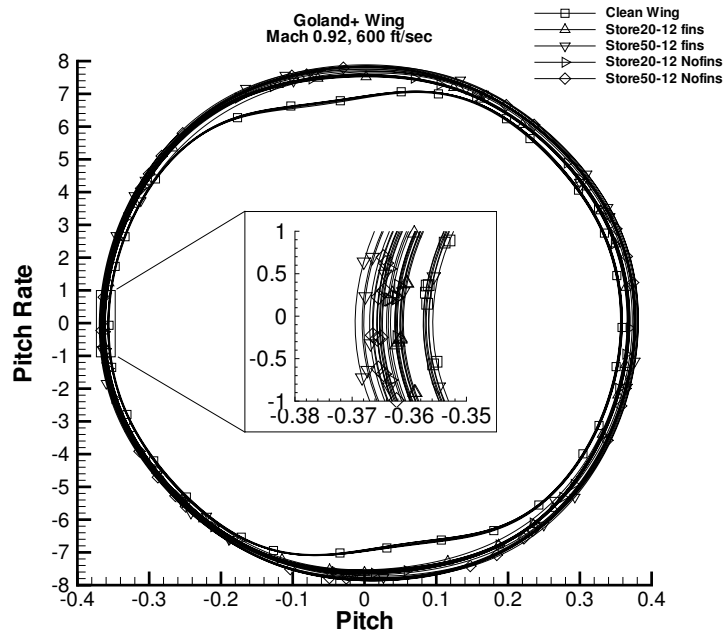

(b) Pitch Phase Plot (Wing Tip)

Figure 4.13   Phase Plots for Wing with Small Stores

the store configurations. The fins were aft of the wing so they did not affect the flow field on the wing. For these small stores, fins did not make a difference in the LCO behavior (Figure 4.14). They did increase the store forces, but the store forces were so small compared to the wing forces that the effects on LCO were negligible. The pylon height was changed from 12 in (0.3048 m) to 6 in (0.1524 m) in order to change the store moments. Shortening the pylon only made a small difference in the LCO behavior (Figure 4.15). The store forces and the wing response were similar, regardless of the pylon height. Shortening the pylon led to lower mode 2 amplitudes, or less twist, but otherwise, the behavior was the same regardless of pylon height. The fins and pylon height weakly affected the twisting moment, whereas, the bending force was the primary contributor to LCO.

The store forces that were transferred into the structural model were magnified in order to amplify how the store forces affected the LCO. Solutions for the wing with a 12 in (0.3048 m) diameter under-wing store centered on a 12 in (0.3048 m) pylon were computed, but with the store forces that were calculated from the aerodynamic loads being magnified by ± 5 before being transferred into the structural model. Altering the store forces in this manner affected the LCO (figures 4.16 and 4.17). The store forces increased the total bending force on the wing, which increased the LCO amplitude. The bending force primarily affected LCO by directly contributing to mode 1. Magnifying the bending force increased the amplitude of the LCO because it increased the restoring force, resulting in greater overshoot beyond the neutral position. Magnifying and reversing the phase of the loads (multiplying forces by -5) decreased the restoring force resulting in less overshoot and a decreased amplitude LCO. These results reinforced the hypothesis that the increased LCO amplitudes observed with small under-wing stores were caused by the store loads which were greater than the quenching effect caused by interference of the flow on the bottom of the wing.

(a) Plunge Phase Plot (Wing Tip)

(b) Pitch Phase Plot (Wing Tip)

Figure 4.14   Phase Plots for Wing with Finned-Stores
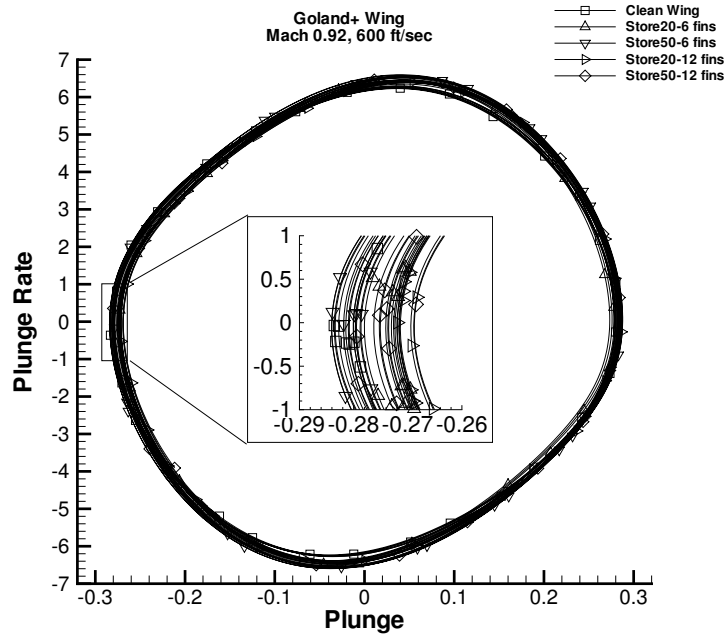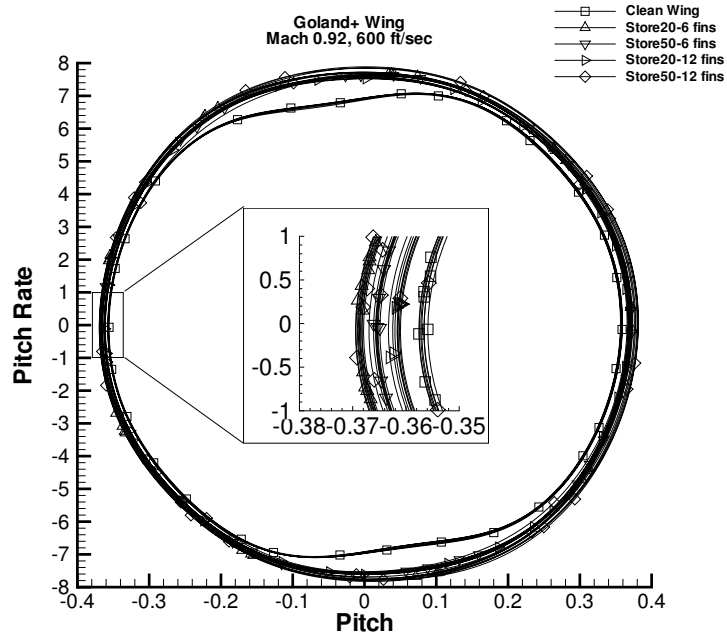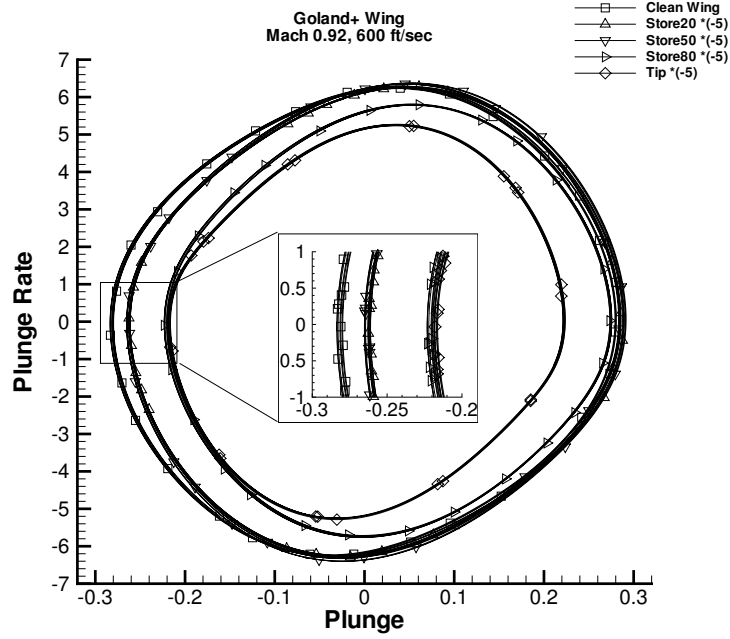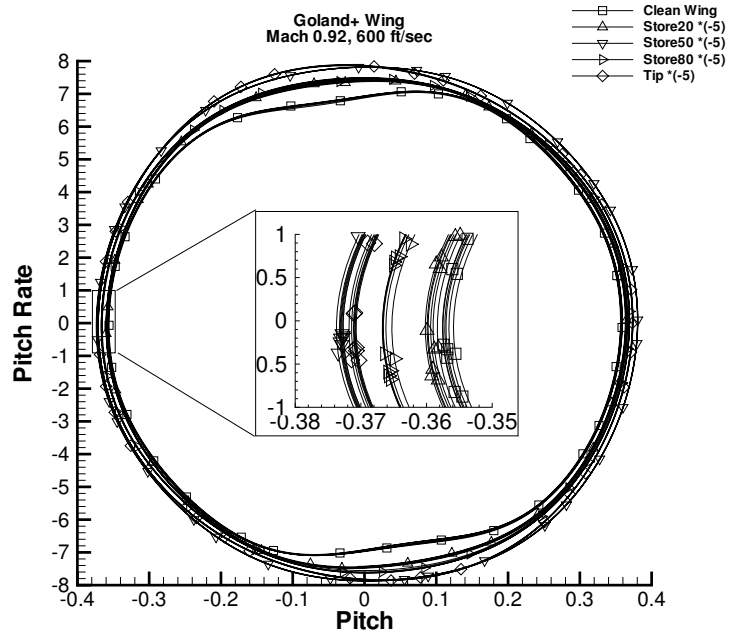
(a) Plunge Phase Plot (Wing Tip)

(b) Pitch Phase Plot (Wing Tip)

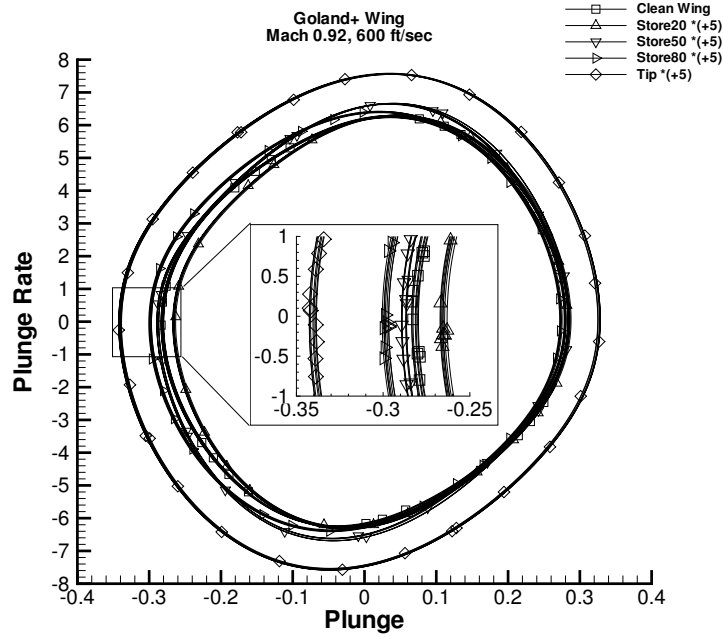Figure 4.15   Phase Plots for Pylon Height Changes

(a) Plunge Phase Plot (Wing Tip)
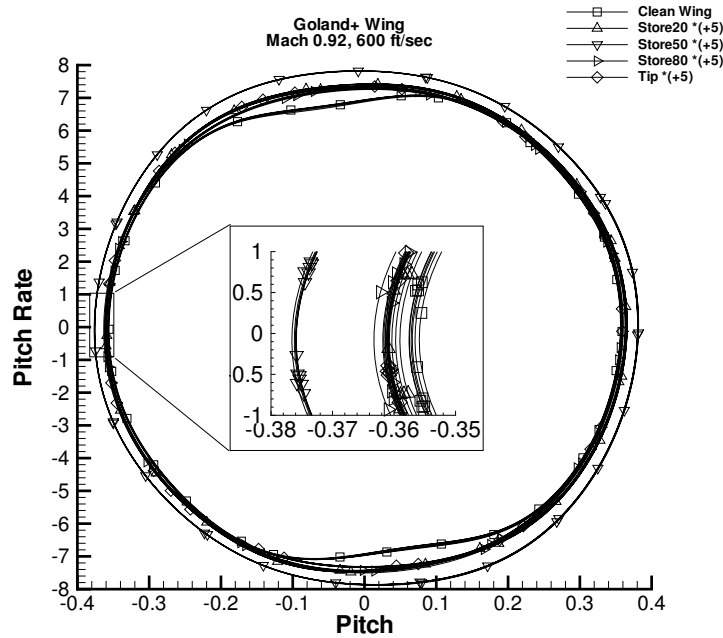

(b) Pitch Phase Plot (Wing Tip)

Figure 4.16   Phase Plots when Store Forces Magnified by -5

4-21

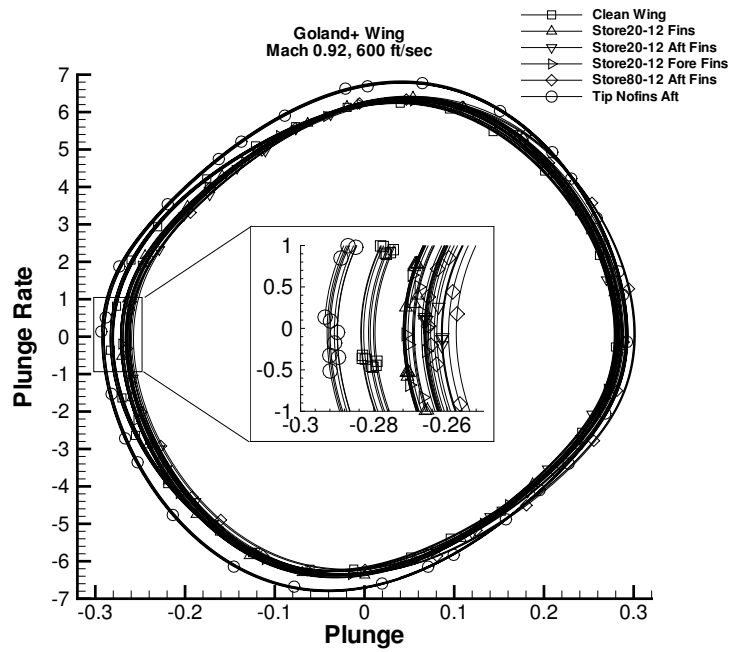(a) Plunge Phase Plot (Wing Tip)

(b) Pitch Phase Plot (Wing Tip)

Figure 4.17   Phase Plots when Store Forces Magnified by +5

The second mechanism by which under-wing stores affected LCO was by interfering with the airflow on the bottom of the wing. The 80% half-span configuration with a small store was computed with the store forces turned off in order to isolate this interference effect. When the store forces were ignored, C_L decreased 0.97%, C_M decreased 1.26%, the tip angle-of-attack decreased 1.59%, mode 1 amplitudes decreased 1.67%, and mode 2 amplitudes decreased 1.82%. These results demonstrated that interference from a small store slightly quenched the LCO.

The under-wing store grids with the 12 in (0.3048 m) pylon and fins were modified to see how stream-wise store position affects the interference on the bottom of the wing. The stores were shifted 2 ft (0.6096 m) fore and aft. The pylon remained centered beneath the wing. Moving the store aft produced LCO (Figure 4.18). When the 50% half-span store and the 80% half-span store were moved forward, the flow separated on the store causing the inviscid fluid solver to fail, so no conclusions could be drawn. The 20% half-span store resulted in LCO when moved forward. This LCO magnitude was similar to the original centered store position. When the stores were moved aft, they only slightly affected the LCO. Shifting under-wing stores fore or aft only slightly changed the LCO because the change in the forces was very small and the interference of the flow on the wing because of the store remained small.

To further amplify the interference effect, the stores without fins were doubled in diameter to 24 in (0.6096 m). The centered 12 in (0.3048 m) pylon was retained. As can be seen in Figure 4.19, the large diameter store had a large affect on the LCO. Whereas adding a small under-wing store produced an LCO of slightly greater amplitude, adding a large under-wing store resulted in an LCO of smaller amplitude. The further outboard the large store, the smaller the amplitude of the LCO. Again, the total modal forces did not change greatly for large stores. The aerodynamic forces were slightly higher with a large store than with a small store but were still less than 1% of the total forces for all modes. This indicated that the large store was affecting the flow on the bottom of the wing and it was influencing the dynamic shock

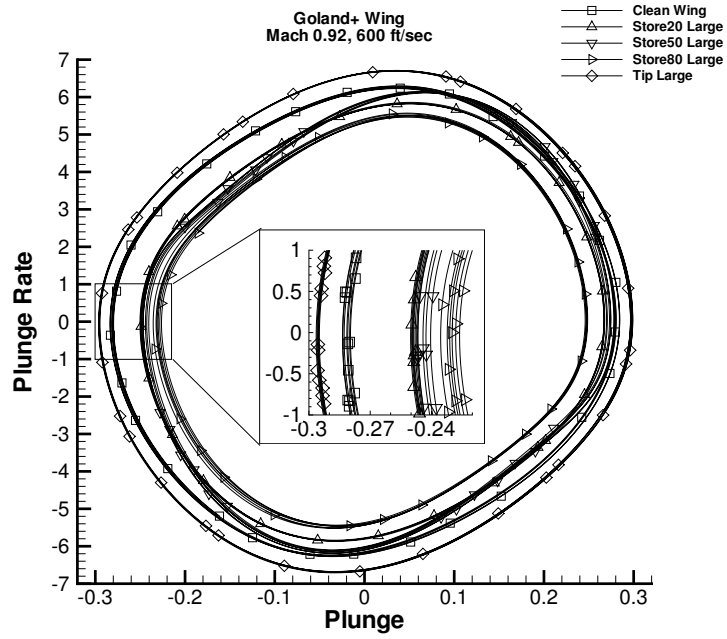(a) Plunge Phase Plot (Wing Tip)
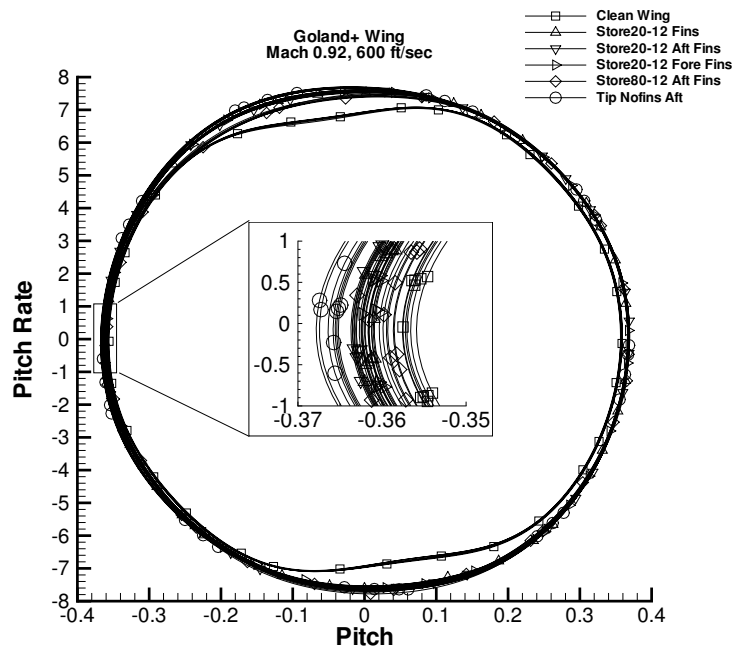
(b) Pitch Phase Plot (Wing Tip)

Figure 4.18   Phase Plots for Wing with Stores Shifted Stream-Wise

motion which was limiting the energy flow into the structure. The interference effect was not great enough to damp out the oscillations, but it was enough to decrease the LCO amplitude.

The large store at 80% half-span illustrates how under-wing stores affect the flow field on the bottom of the wing, and thereby, affect the LCO. When the wing was bent up and twisted down, the flow on the top of the wing was unchanged from the clean wing condition. However, on the bottom of the wing (Figure 4.20a) there were significant changes when compared to the clean wing at the same point in an LCO cycle (Figure 4.20b). The lambda shock was weak if detectable at all, and the normal shock at the trailing edge was weaker than that experienced by the clean wing. The store wake, or the flow from the store that impinged on the flow on the bottom of the wing, increased the pressure on the front half of the wing in the vicinity of the store. The normal shock then increased the pressure again (Figure 4.21). The increase in pressure decreased the downward restoring force on the wing, which had the same effect as the lambda shock on the clean wing, limiting the energy flow into the wing. When the wing was bent down and twisted up, the flow on the top of the wing was unchanged from the clean wing condition. The lambda shock and trailing-edge shock were present, though weaker than those present in the clean wing because of the lower pitch and plunge amplitudes (Figure 4.22). These shocks were still providing quenching leading to LCO. If the store was large enough to have a large wake raise the pressure on the wing, it provided quenching. A very small store with a minimal wake had minimal impact on the LCO caused by interference from the store.

Multiple, small-diameter stores were added to the Goland[+] wing to create further interference. A tip store and the under-wing stores at 20% and 50% half-span were added to the Goland[+] wing. The centered 12 in (0.3048 m) pylon was retained. The small-diameter stores resulted in an LCO with an amplitude slightly greater than the clean wing. For the small stores, the store forces effect was stronger

(a) Plunge Phase Plot (Wing Tip)
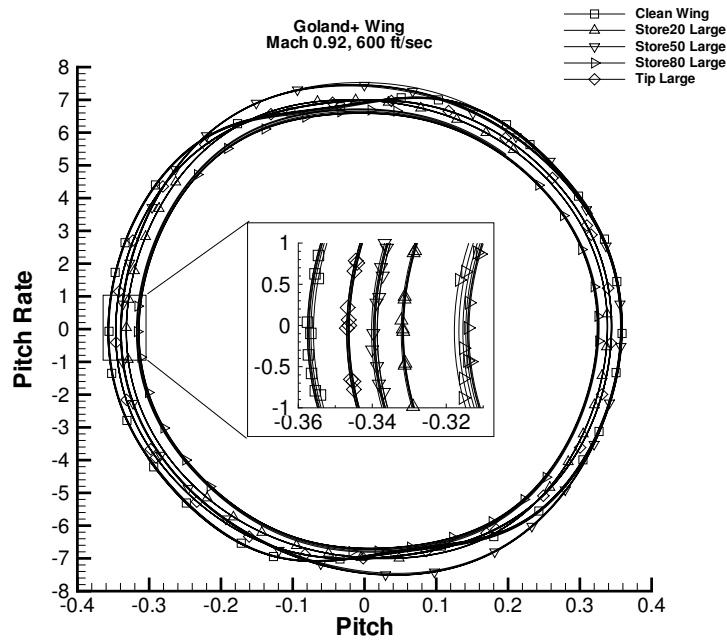
(b) Pitch Phase Plot (Wing Tip)

Figure 4.19   Phase Plots for Large Stores
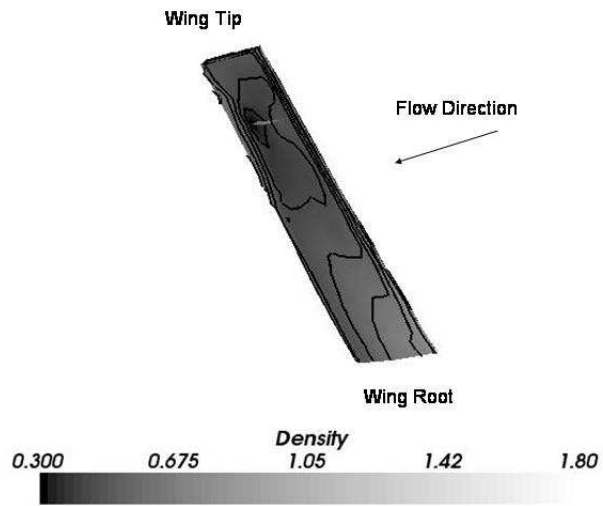
(a) Large 80% Store
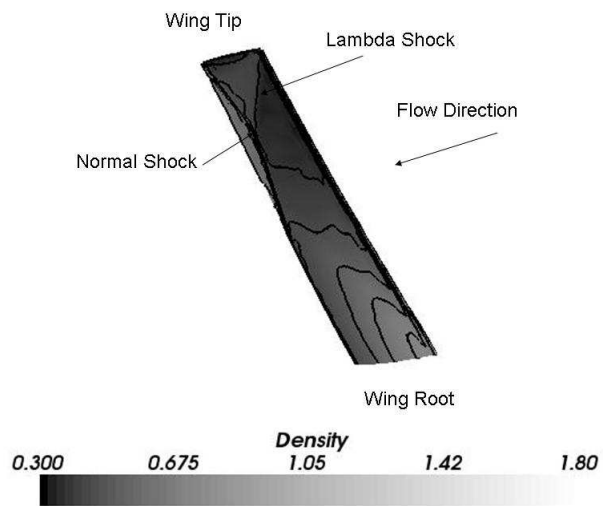
(b) Clean Wing

Figure 4.20   Large 80% Store at 10.495 Seconds (Density Contours)
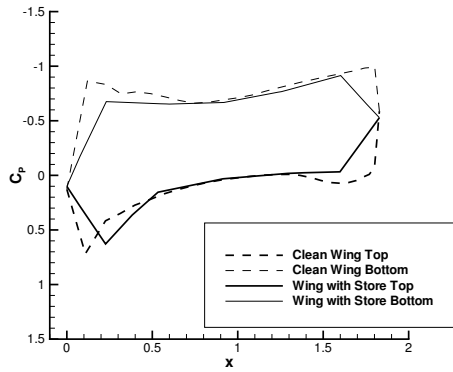
(a) 2m span
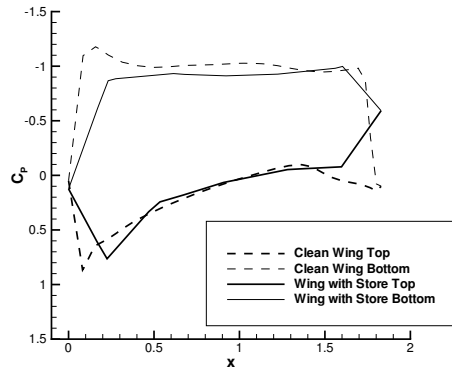
(b) 3m span
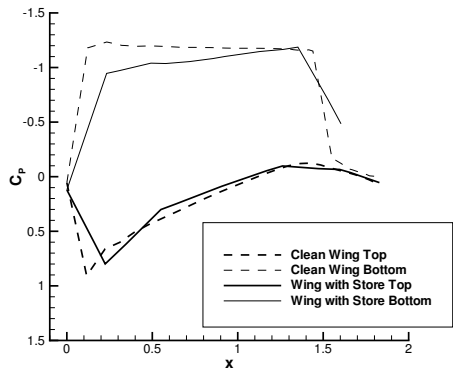
(c) 4m span
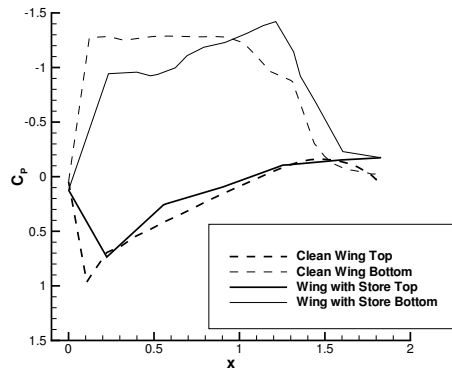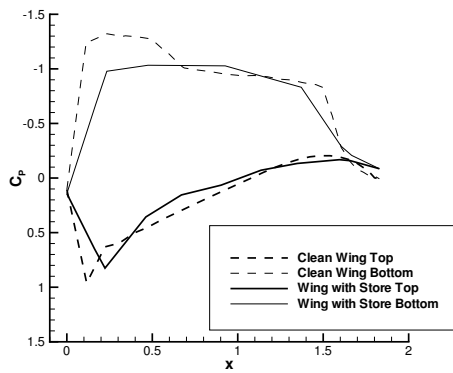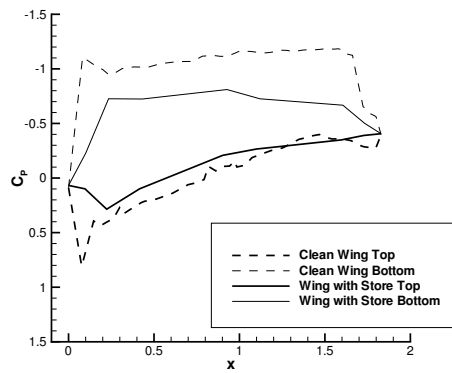
(d) 5m span

(e) 5.5m span

(f) 6m span

Figure 4.21   Large 80% Store at 10.495 Seconds (Pressure Distribution)
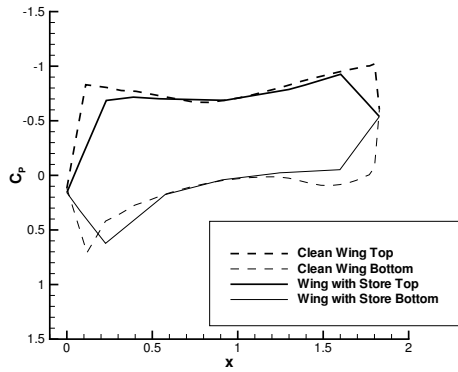
(a) 2m span
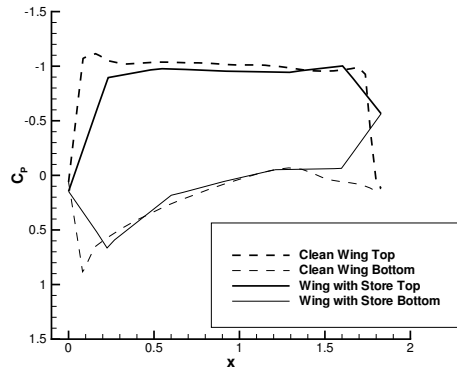
(b) 3m span
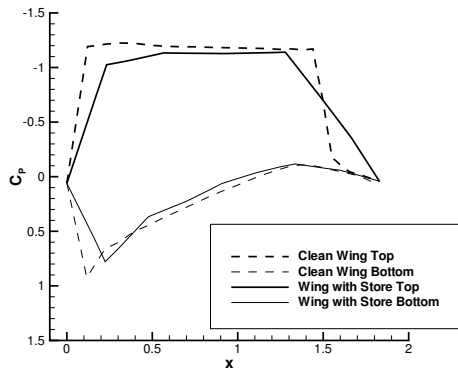
(c) 4m span
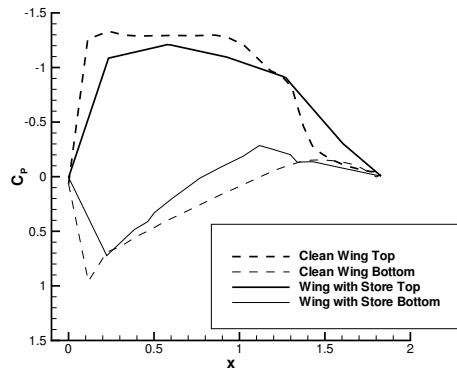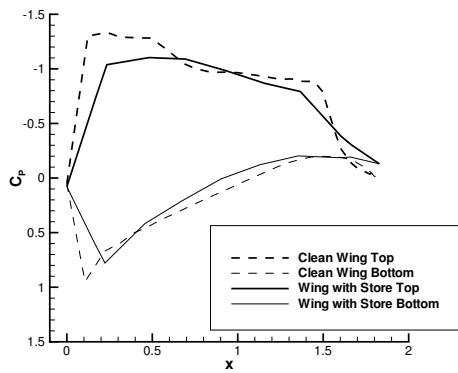
(d) 5m span

(e) 5.5m span
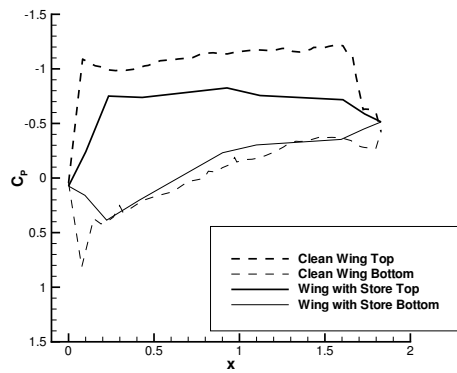
(f) 6m span

Figure 4.22   Large 80% Store at 10.645 Seconds (Pressure Distribution)

than the interference damping effect (Figure 4.23). Multiple, large-diameter stores were then added to the Goland$^+$ wing to create further interference. When the large-store configuration was run, the oscillations damped out. The multiple, large stores interfered with the flow on the bottom of the wing to the extent that it prevented the energy flow into the structure, resulting in damping.

One effect that under-wing stores had on LCO was shown by the mode 1 response oscillating about a negative value instead of about zero, as with a clean wing or with a tip store. This showed that the presence of the under-wing stores shifted the static aeroelastic solution. Shifting the static aeroelastic solution did not change the LCO response, only the neutral configuration about which the wing oscillated. This was further demonstrated by computing the solution for the clean Goland$^+$ wing at a positive angle-of-attack (Appendix E).

To examine the effect of store mass position on LCO as opposed to the store aerodynamics, inertial forces were added to the store aerodynamic forces. The 12 in (0.3048 m) diameter under-wing stores centered on 12 in (0.3048 m) pylons were run with a store mass located -2 ft (-0.6096 m), -1 ft (-0.3048 m), 0 ft (0.0 m), 1 ft (0.3048 m), and 2 ft (0.6096 m) in the x-direction (stream-wise direction) from the elastic axis. As can be seen in Figure 4.24, when the mass was added on the elastic axis or forward of the elastic axis, the LCO amplitude only slightly increased for the under-wing store located at 20% half-span. However, if the mass was added 1 ft (0.3048 m) aft of the elastic axis, a different LCO mode was encountered (figures 4.24 and 4.25). The amplitudes grew in the same manner as the case without the mass, but at approximately 4 seconds, mode 4 started growing and eventually stabilized. At approximately 14 seconds, a new LCO state was reached. When the mass was added 2 ft (0.6096 m) aft of the elastic axis, all of the modes grew, leading to divergent flutter.

When the mass was added to the 50% half-span, under-wing store, divergent flutter was obtained for all stream-wise locations. It was hypothesized that this was
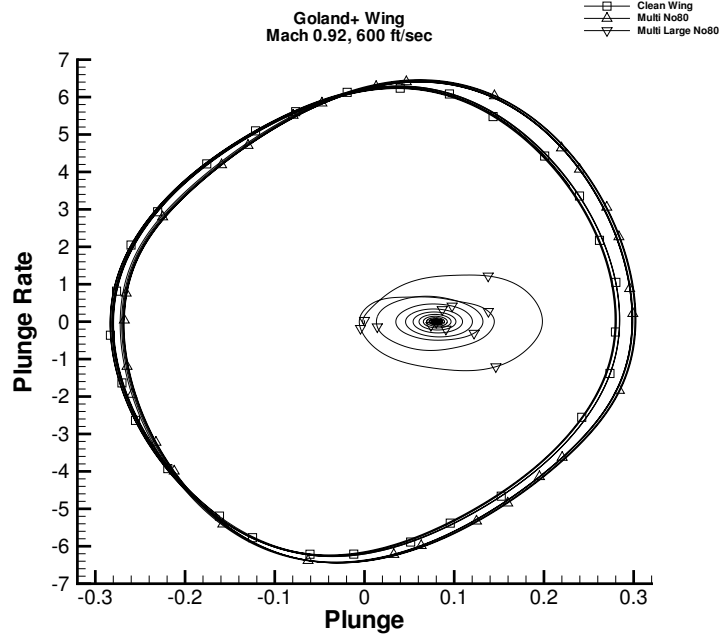
(a) Plunge Phase Plot (Wing Tip)
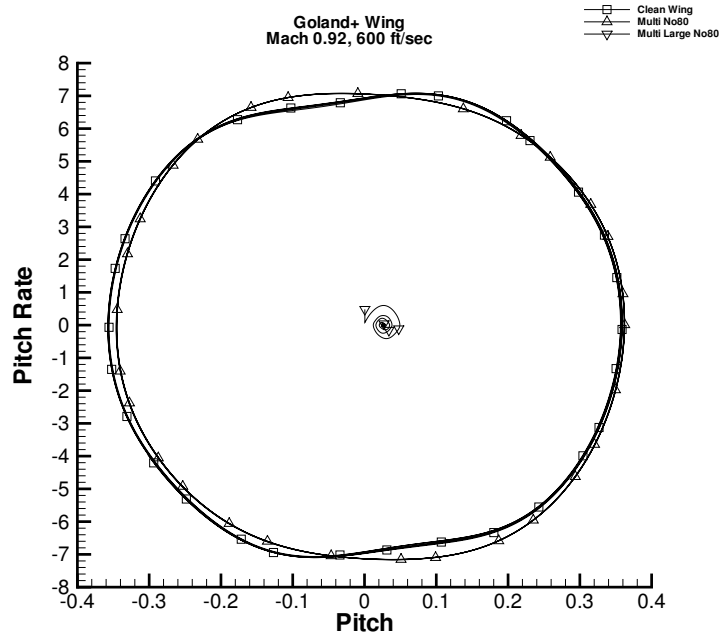
(b) Pitch Phase Plot (Wing Tip)

Figure 4.23   Phase Plots for Wing with Multiple Stores
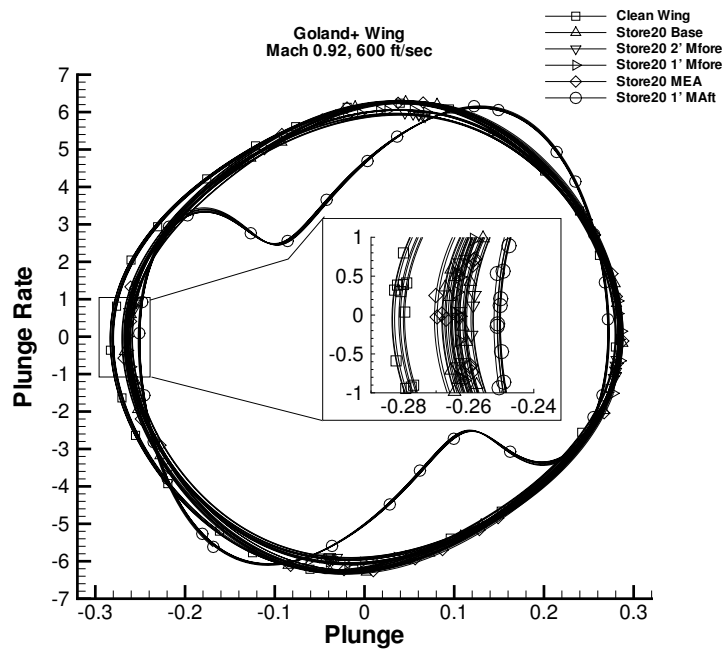
(a) Plunge Phase Plot (Wing Tip)
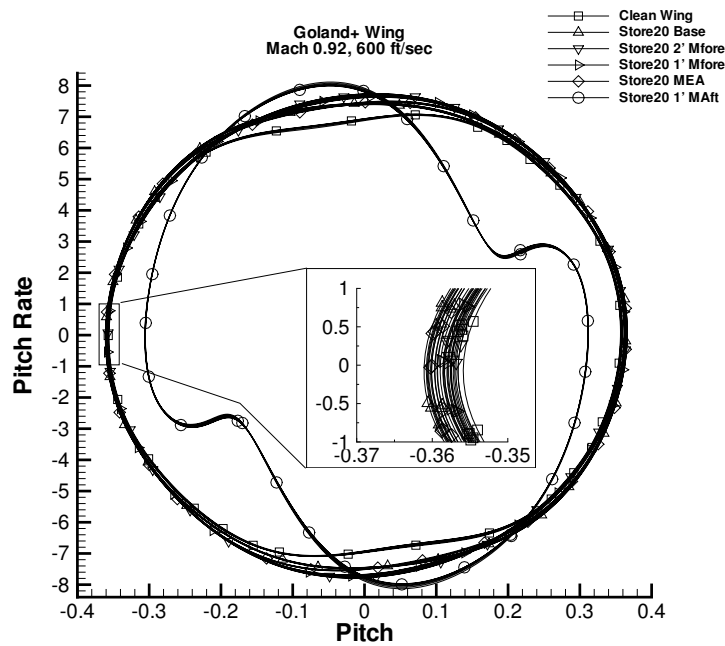
(b) Pitch Phase Plot (Wing Tip)

Figure 4.24   Phase Plots for Store Point Mass at 20% Half-span
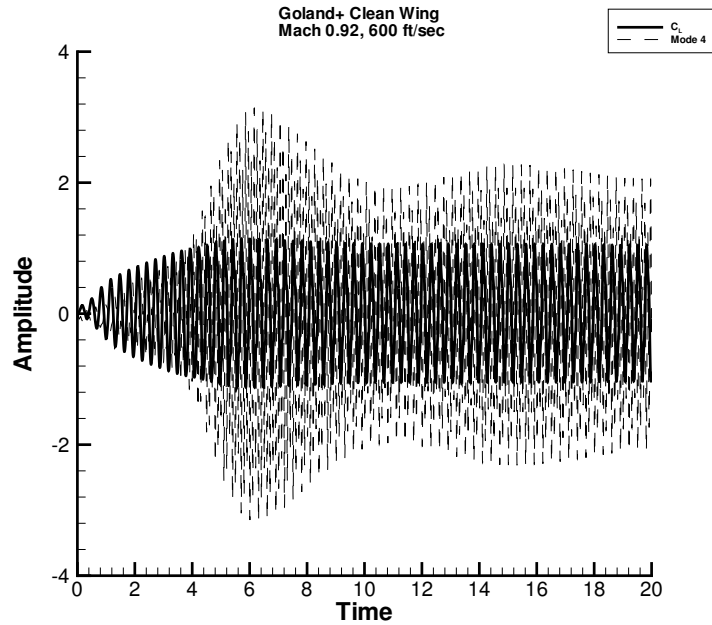
Figure 4.25   Amplitudes for Point Mass 1' Aft of EA at 20% Half-span

because the stores primarily contributed to mode 3 forces. When the store mass was located where mode 3 provided the greatest contribution, it had a large effect. When the mass was placed on the elastic axis, it came close to stabilizing into an LCO. It initially appeared to enter the LCO condition observed without the mass, but at approximately 6 seconds, mode 4 started to diverge followed by mode 3, eventually driving the system to divergent flutter (Figure 4.26). For the other 50% half-span mass locations, the system immediately went into divergent flutter.

Adding the mass to the 80% half-span store illustrated the stabilizing and destabilizing effect mass position provided, as shown in Figure 4.27. When the mass was located on the elastic axis, a LCO response similar to the no-mass case was observed. As the mass was moved forward of the elastic axis, the LCO amplitudes decreased drastically while mode 2 increased in dominance and mode 1 decreased. This result was expected because adding a mass forward of the elastic axis raised the flutter speed, which led to a decreased amplitude LCO. The modes continued to be

Goland+ 50% Store, 12" Pylon, Mass on EA
Mach 0.92, 600 ft/sec
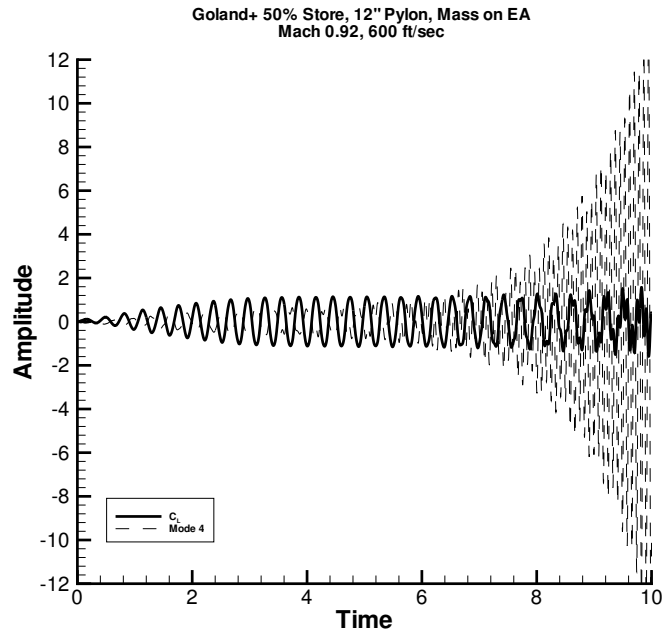
Figure 4.26   Amplitudes for Point Mass on EA at 50% Half-span

coupled into a single-degree-of-freedom response. When the mass was moved aft of the elastic axis, the LCO amplitudes increased significantly. Again, this matched the expected result because adding a mass aft of the elastic axis lowered the flutter speed, leading to an increased amplitude LCO. Mode 1 continued to grow in dominance while mode 2 decreased in importance. The modes continued to be coupled into a single-degree-of-freedom response, but with mode 4 growing and beginning to play a role in the response. However, by the time the mass had moved 2 ft (0.6096 m) aft, it was no longer a single-degree-of-freedom response, and a different LCO state was reached. If the mass continued to move aft, mode 4 would begin to dominate and divergent flutter would be encountered. Adding inertial forces did not change the shock motion nor change the quenching mechanism. It did change the inertia of the wing and determined how efficient the shock motion was at limiting the energy transferred into the structure. As the wing twisted more due to a forward mass, the shock motion caused the energy flow to be limited before the inertia grew too

4-34

high, decreasing the amplitude of the LCO. Conversely, as the wing bent more for a rearward mass, the inertia grew higher before the shock motion limited the energy flow, thereby, increasing the amplitude of the LCO.

4.4   Goland⁺ Wing with Tip-Store Results

A tip store affected the circulation of the fluid around the wing tip and contributed to store forces, but it did not interfere with the airflow on the bottom of the wing. Adding a tip store increased the mode 1 and mode 2 responses. Like the under-wing stores, the tip store primarily contributed to force in mode 3 where the tip store was responsible for 4.8% of the total mode 3 force. However, the total force in mode 3 decreased by 6.63% from that of the clean wing. Adding the tip store increased C_L by 5.06% and the tip angle-of-attack by 1.43%. Unlike the under-wing store, the mode 1 response for the tip store oscillates about zero instead of about a negative value, the same as the clean wing. These changes resulted in the amplitudes of the motion growing faster than the clean wing and reaching LCO more quickly. The tip store increased the mode 1 amplitudes which increased the amount of bending.

The tip store was shifted 2 ft (0.6096 m) fore and aft. When the tip store was moved forward, the motion damped out. Analysis showed that the flow around the tip of the wing was very sensitive to the presence of a store. Moving the tip store forward appeared to prevent the energy from flowing into the wing because mode 1 and mode 2 did not couple into a single-degree-of-freedom flutter mode, but remained independent. Unlike the LCO cases, store forces also directly correlated with modal response with mode 1 and mode 2 being the dominant force contributors. Moving the tip store aft resulted in an LCO state with a similar twist and greater plunge compared to the centered store LCO. In this case, mode 1 increased greatly when the store was shifted aft. The tip angle-of-attack, C_L, C_M, and the modal forces all increased slightly. Mode 3 decreased slightly while modes 2, 4, 5, and 6 all increased
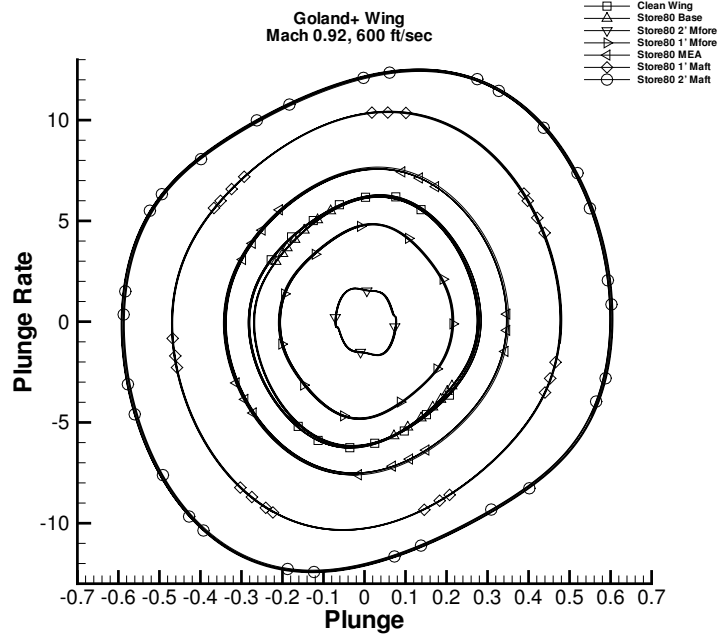
(a) Plunge Phase Plot (Wing Tip)
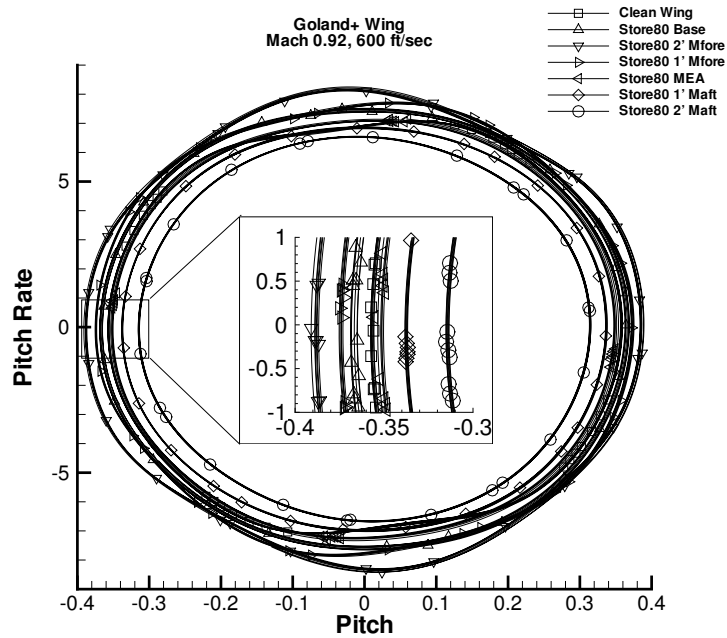
(b) Pitch Phase Plot (Wing Tip)

Figure 4.27   Phase Plots for Store Point Mass at 80% Half-span

slightly. Overall, moving the tip store fore and aft showed that the wing-tip region was very sensitive to flow changes. These flow changes manifested as changes in the mode 1 response leading to damping (move tip store forward) or by increasing the amount of plunge (move tip store aft).

In order to amplify the effect the store forces were having on the LCO, the store forces were magnified by ± 5 before being transferred into the structural model. Magnifying the loads in this manner affected the LCO (figures 4.16 and 4.17). Tip stores have the same effects as under-wing stores: magnifying the bending force on the wing, and increasing the LCO amplitude. The same effect was seen when the tip store diameter was increased to 10 in (0.254 m). As can be seen in Figure 4.19, the large diameter tip store produced a higher amplitude LCO. The large tip store contributed 9% of mode 3 forces. Unlike the under-wing stores, this was a significant fraction of the total forces on the wing. The store basically acted as an extension of wing area, increasing the bending forces on the wing and increasing the LCO amplitude.

To examine the effect of tip-store mass position on LCO as opposed to store aerodynamics, inertial forces were added to the store aerodynamic forces. The 5 in (0.127 m) diameter tip store was run with a store mass located -2 ft (-0.6096 m), -1 ft (-0.3048 m), 0 ft (0.0 m), 1 ft (0.3048 m), and 2 ft (0.6096 m) in the x-direction (stream-wise direction) from the elastic axis. When the mass was added at the wing tip on the elastic axis, mode 6 began to grow at 2.5 seconds and led to divergent flutter. When the mass was added aft of the elastic axis, all of the modes, except for mode 2, began to grow which led to divergent flutter. When the mass was added forward of the elastic axis (Figure 4.28), it appeared that a coupled LCO response was obtained with mode 2 being increasingly dominant the further forward the mass was moved. However, at approximately 10 seconds, mode 4 rapidly began to grow leading to divergent flutter (Figure 4.29). Adding inertial forces forward of the elastic axis changed the coupling of the modes and did not lead to a lower amplitude

LCO. As seen with the under-wing stores, adding the inertial forces did not change the shock motion nor change the damping mechanism but instead changed how the modes couple. The coupling of the primary bending and twisting modes is what led to shock motion that provided the energy quenching necessary for LCO.
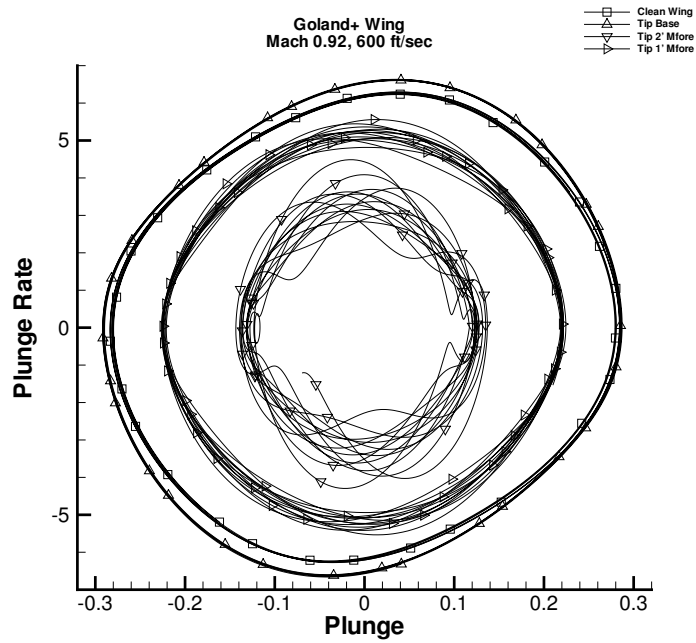
(a) Plunge Phase Plot (Wing Tip)
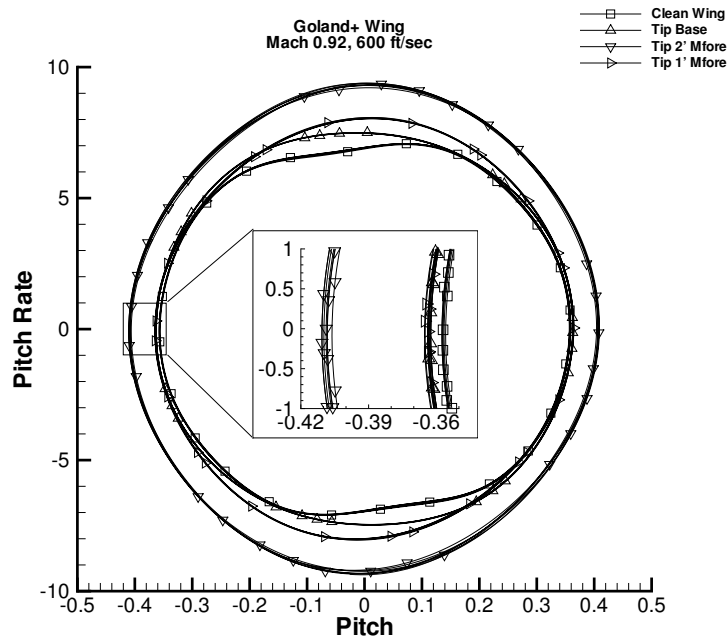
(b) Pitch Phase Plot (Wing Tip)

Figure 4.28   Phase Plots for Store Point Mass at Wing Tip
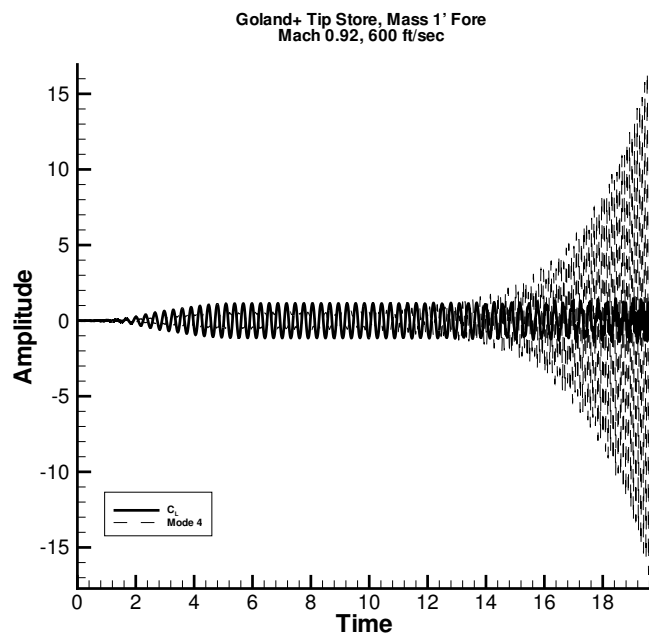
Figure 4.29   Amplitudes for Point Mass 1' Fore of EA at Tip

V. Conclusions

5.1 Conclusions

FLUENT 6.1 was successfully integrated with a modal structural model to form an aeroelastic program based on a fully unstructured grid formulation capable of simulating flutter and LCO. Using this program, the aerodynamic nonlinearity responsible for LCO of the Goland[+] clean-wing (with tip mass) at Mach 0.92, 600 ft/sec (182.88 m/sec), was analyzed. The LCO consisted of a nearly in-phase coupling of mode 1 and mode 2, which produced a single-degree-of-freedom torsional motion with an axis of rotation running from the elastic axis at the root of the wing, to a point slightly forward of the leading edge at the tip of the wing. For LCO to exist, a nonlinearity must have been present to provide the quenching mechanism that limited the amplitude of the oscillations. For the Goland[+] wing, the only nonlinearity present was the appearance/disappearance of shocks. Flow separation and structural nonlinearity were not modelled. Periodically appearing and disappearing lambda and trailing-edge shocks decreased the restoring forces on the Goland[+] wing, resulting in a balancing of the inertial forces and a stable LCO.

For the Goland[+] wing, as the oscillations grew, there was a transition from Tijdeman type-A shock motion [56], to Tijdeman type-B shock motion [56] in the inboard half of the wing. The shock motion in the outboard half of the wing span remained type-A. The type-B shock motion limited the flow of energy from the fluid into the structure, and changed the amplitude growth from an exponential growth to a linear growth. The type-B motion continued to gain strength until it consisted of an appearing and disappearing shock at the trailing edge, with no observable fore/aft motion.

Two additional quenching mechanisms later appeared in the outboard half-span, which further limited the amplitude growth and led to LCO. The first was a strong trailing-edge shock that moved fore and aft, and the second was a strong

lambda shock that ran from the leading edge of the wing near the tip, to the normal shock on the trailing edge. These shocks decreased the restoring force on the wing limiting the overshoot, thereby balancing the inertial forces producing a stable LCO. The combination of type-B shock motion, lambda shock motion, and the motion of the normal shock at the trailing edge was responsible for limiting the energy flow from the fluid to the structure resulting in LCO.

Aerodynamic store shapes were added to the Goland$^+$ wing at different spanwise locations to determine how store aerodynamics affect LCO. It was found that aerodynamic store shapes affect LCO in two ways: by interfering with the flow field on the wing surface, and by adding loads into the structure. Under-wing stores interfered with the airflow on the lower surface of the wing, diminishing LCO amplitudes. On the other hand, the transfer of store loads into the wing structure increased LCO amplitudes for both tip stores and under-wing stores. Under-wing stores also led to a negative offset of the amplitudes of the primary bending mode by shifting the static aeroelastic solution. The addition of stores did not affect the LCO frequency, which was always approximately 3.3 Hz. In addition to the negative offset, under-wing stores decreased the mode 1 amplitudes, which decreased the amount of bending. Tip stores increased the mode 1 amplitudes, which increased the amount of bending.

Aerodynamic store forces increase LCO amplitudes. This effect was demonstrated when the aerodynamic store forces were magnified in order to better discern their effect on LCO. Magnifying the forces showed that the twist of the wing was driven by mode 1 and mode 2 coupling. The bending force primarily affected the LCO by directly contributing to mode 1. Magnifying the bending force increased the amplitude of the LCO. This was expected because increasing the restoring force resulted in greater overshoot beyond the neutral position. Magnifying but reversing the direction of the aerodynamic store forces decreased the restoring force resulting in less overshoot and a decreased amplitude LCO.

Interference from under-wing stores decreases LCO amplitudes. The larger the diameter of the under-wing store, the larger the interference with the flow field on the bottom of the wing. This led to increased energy quenching and a lower amplitude LCO. Multiple stores were added to the Goland$^+$ wing. Again, it was found that the larger the store, the more energy quenching that was present due to interference with the flow field on the bottom of the wing.

In summary, The energy quenching mechanism responsible for limit-cycle oscillation in the Goland$^+$ wing has been determined. The primary bending and torsional modes couple, resulting in periodically appearing and disappearing lambda and trailing-edge shocks which decrease the restoring forces on the wing, limiting the flow of energy from the fluid into the structure. Stores affect LCO in two offsetting ways. Adding under-wing stores interferes with the airflow on the bottom of the wing which also reduces the restoring forces, thereby providing additional quenching of the LCO. Under-wing and tip stores also add carriage loads into the wing which increases the flow of energy from the fluid into the structure, thereby amplifying the LCO.

5.2   Recommendations for Future Research

The Goland$^+$ wing was analyzed with an inviscid fluid solver and using the thin-plate spline to transfer data between the aerodynamic and structural grids. These splines conserved total forces and moments but did not conserve energy. The next step in the research should involve incorporation of an energy-conserving spline that more accurately transfers data between the grids.

FLUENT's grid deformation algorithms were the main limitation preventing the use of the viscous solver and FLUENT's turbulent models. Grid deformation could be controlled externally by incorporating a faster and more robust grid deformation algorithm tailored for deforming wings. This could be implemented through a UDF, bypassing FLUENT's internal grid deformation algorithms. FLUENT In-

corporated is also addressing this short-coming and may provide a faster and more robust grid deformation algorithm in a future release. With a faster, more robust grid deformation algorithm, and using the viscous solver, the flow around the wing tip and around the stores could be examined in more detail. A viscous analysis into how stream-wise movement of stores could then be conducted. Viscous analysis would also allow for nonlinearities due to shock-wave/boundary-layer interaction to be studied.

Inertial forces were added to the Goland$^+$ wing in order to compare how store mass position affected LCO as opposed to the store aerodynamics. In this research, inertial forces were added to the store forces by simulating the addition of a store mass. The structural model was not modified; the mass matrix, stiffness matrix, and the modal matrix did not contain any store mass effects. In future research, the structural model should be modified to account for these store masses in order to validate the results what were obtained by simulating the masses. The effect of adding masses at different span-wise and stream-wise positions on LCO and on the flutter stability boundary should be further studied.

There is significant interest in the discovery of LCO during flight test of an F–16. Future research should try to duplicate this flight test scenario. Initial simulations of this scenario did not result in LCO (Appendix F). In the initial inviscid simulations, only the wing and the tip launcher were modelled. The fuselage and under-wing stores were not modelled. The dominant bending and twisting modes did not couple into a single degree-of-freedom flutter mode as did the Goland$^+$ wing. Additional testing should be conducted to determine whether LCO can be obtained with this simplified wing or whether additional grid details, such as the fuselage and under-wing stores, need to be included. Viscous modelling may also be necessary to duplicate the flight test results.

Appendix A.   Spline Routines

For aeroelastic analysis, there are two grids; an aerodynamic grid on the surface of the body, and a structural grid on the structural members of the body. Data needs to be transferred between these two grids, but they normally are non-point matching. In this case, a spline matrix can be used to transfer data between the grids.

A.1   Thin-Plate Spline

The thin-plate spline method provides a means to characterize an irregular surface by using functions that minimize $\int_\Omega |D^2 v|^2$, a functional similar to the bending energy of a thin plate [18]. Duchon [18] proved that only one solution exists in the form

$$\sigma(t) = \sum_{a \epsilon A} \lambda_a |t - a|^2 \ln|t - a| + \alpha_o t + \beta \qquad (A.1)$$

with $\sum \lambda_a = 0$ and $\sum \lambda_a a = 0$.

The function in A.1 can be used to construct a function $\delta(x)$, given its values at a set of N discrete "nodal" values [50]

$$\delta(\bar{x}) = \beta + \alpha_{o_x} x + \alpha_{o_y} y + \alpha_{o_z} z + \sum_{i=1}^{N} \lambda_i |\bar{x} - \bar{x}_i|^2 \ln|\bar{x} - \bar{x}_i|. \qquad (A.2)$$

The coefficients λ_i, β, α_{o_x}, α_{o_y}, and α_{o_z} are determined by solution of the minimization problem [50]. Applying A.2 to each of the N nodes yields

$$H_i = \beta + \alpha_{o_x} x_i + \alpha_{o_y} y_i + \alpha_{o_z} z_i + \sum_{j=1}^{N} \lambda_j |\bar{x}_i - \bar{x}_j|^2 \ln|\bar{x}_i - \bar{x}_j|. \qquad (A.3)$$

Equation A.3 is subject to the following side conditions:

$$\sum_{i=1}^{N} \lambda_i = \sum_{i=1}^{N} \lambda_i x_i = \sum_{i=1}^{N} \lambda_i y_i = \sum_{i=1}^{N} \lambda_i z_i = 0. \qquad (A.4)$$

Writing equations A.3 and A.4 in matrix notation gives

$$\{\delta\} = [B]\{\lambda\} + [R]\{\alpha\} \tag{A.5}$$

and

$$[R]^T\{\lambda\} = 0. \tag{A.6}$$

The elements of $[B]$ are

$$B_{ij} = r_{ij}^2 \ln(r_{ij}^2) \tag{A.7}$$

and the elements r_{ij}^2 are defined as

$$r_{ij}^2 = (x_i - x_j)^2 + (y_i - y_j)^2 + (z_i - z_j)^2. \tag{A.8}$$

The matrix $[R]$ is defined as

$$[R] = \left[\left\{ \begin{array}{c} 1 \\ 1 \\ \vdots \\ 1 \end{array} \right\} \left\{ \begin{array}{c} x_1 \\ x_2 \\ \vdots \\ x_N \end{array} \right\} \left\{ \begin{array}{c} y_1 \\ y_2 \\ \vdots \\ y_N \end{array} \right\} \left\{ \begin{array}{c} z_1 \\ z_2 \\ \vdots \\ z_N \end{array} \right\} \right]. \tag{A.9}$$

The column matrices $\{\delta\}$, $\{\lambda\}$, and $\{\alpha\}$ are defined as

$$\{\delta\} = \left\{ \begin{array}{c} \delta_1 \\ \delta_2 \\ \vdots \\ \delta_N \end{array} \right\}, \tag{A.10}$$

$$\{\lambda\} = \begin{Bmatrix} \lambda_1 \\ \lambda_2 \\ \vdots \\ \lambda_N \end{Bmatrix}, \tag{A.11}$$

and

$$\{\alpha\} = \begin{Bmatrix} \beta_o \\ \alpha_{ox} \\ \alpha_{oy} \\ \alpha_{oz} \end{Bmatrix}. \tag{A.12}$$

Solving equations A.5 and A.6 for $\{\lambda\}$ and $\{\alpha\}$ gives

$$\{\lambda\} = \left[[B]^{-1} - [B]^{-1}[R] \left[[R]^T[B]^{-1}[R] \right]^{-1} [R]^T[B]^{-1} \right] \{\delta\} \tag{A.13}$$

and

$$\{\alpha\} = \left[[R]^T[B]^{-1}[R] \right]^{-1} [R]^T[B]^{-1}\{\delta\}. \tag{A.14}$$

Letting subscript s represent the structural grid and subscript a represent the aerodynamic grid, equation A.5 can then be written as

$$\{\delta_a\} = [B_{as}]\{\lambda_s\} + [R_a]\{\alpha_s\}. \tag{A.15}$$

The transformation spline matrix $[S]$ is needed in the form

$$\{\delta_a\} = [S]\{\delta_s\}. \tag{A.16}$$

Therefore, $\{\delta_s\}$ can be factored out of equation A.15 and the equations can be solved for $[S]$,

$$[S] = \left[[B_{as}] \left[[B_s]^{-1} - [B_s]^{-1}[R_s] \left[[R_s]^T [B_s]^{-1}[R_s] \right]^{-1} [R_s]^T [B_s]^{-1} \right] \right.$$
$$\left. + [R_a] \left[[R_s]^T [B_s]^{-1}[R_s] \right]^{-1} [R_s]^T [B_s]^{-1} \right]. \quad \text{(A.17)}$$

The elements of $[B_{as}]$ and $[B_s]$ are defined as

$$B_{as_{ij}} = r_{as_{ij}}^2 \ln(r_{as_{ij}}^2) \tag{A.18}$$

and

$$B_{s_{ij}} = r_{s_{ij}}^2 \ln(r_{s_{ij}}^2) \tag{A.19}$$

where

$$r_{as_{ij}}^2 = (x_{a_i} - x_{s_j})^2 + (y_{a_i} - y_{s_j})^2 + (z_{a_i} - z_{s_j})^2 \tag{A.20}$$

and

$$r_{s_{ij}}^2 = (x_{s_i} - x_{s_j})^2 + (y_{s_i} - y_{s_j})^2 + (z_{s_i} - z_{s_j})^2. \tag{A.21}$$

$[R_a]$ and $[R_s]$ are defined by equation A.9 where the a subscript stands for the aerodynamic grid and the s subscript stands for the structural grid.

Once the spline transformation matrix $[S]$ is generated, displacements and coordinates of the displaced aerodynamic grid can be computed from displacements of the structural grid with the following:

$$[\delta_a] = [S][\delta_s], \tag{A.22}$$

$$[q] = [q]_o + [\delta] \tag{A.23}$$

where $[q]_o$ is the original undeformed grid. The grid coordinate matrices are defined as

$$[q] = \begin{bmatrix} q_{x_1} & q_{y_1} & q_{z_1} \\ q_{x_2} & q_{y_2} & q_{z_2} \\ \vdots & \vdots & \vdots \\ q_{x_N} & q_{y_N} & q_{z_N} \end{bmatrix}.$$ (A.24)

In addition, the transferal of forces from the aerodynamic grid to the structural grid can be achieved by the transpose of $[S]$ [1],

$$[F_s] = [S]^T [F_a],$$ (A.25)

where the force matrices are defined as

$$[F] = \begin{bmatrix} F_{x_1} & F_{y_1} & F_{z_1} \\ F_{x_2} & F_{y_2} & F_{z_2} \\ \vdots & \vdots & \vdots \\ F_{x_N} & F_{y_N} & F_{z_N} \end{bmatrix}.$$ (A.26)

A limitation of the thin-plate spline is that no two structural-grid points can be located at the same coordinates, nor can all the structural-grid points lie in the same plane [1].

A.2 Infinite-Plate Spline

The infinite-plate spline method [28] is based upon the small deflection equation of an infinite plate. Mathematically, it is a two-dimensional implementation of the thin-plate spline method. The changes to equations A.3, A.8, A.9, A.12, A.20, and A.21 are as follows:

$$H_i = \beta + \alpha_{o_x} x_i + \alpha_{o_y} y_i + \sum_{j=1}^{N} \lambda_j |\bar{x}_i - \bar{x}_j|^2 \ln |\bar{x}_i - \bar{x}_j|,$$ (A.27)

$$r_{ij}^2 = (x_i - x_j)^2 + (y_i - y_j)^2, \tag{A.28}$$

$$[R] = \left[\left\{ \begin{array}{c} 1 \\ 1 \\ \vdots \\ 1 \end{array} \right\} \left\{ \begin{array}{c} x_1 \\ x_2 \\ \vdots \\ x_N \end{array} \right\} \left\{ \begin{array}{c} y_1 \\ y_2 \\ \vdots \\ y_N \end{array} \right\} \right], \tag{A.29}$$

$$\{\alpha\} = \left\{ \begin{array}{c} \beta_o \\ \alpha_{o_x} \\ \alpha_{o_y} \end{array} \right\}, \tag{A.30}$$

$$r_{as_{ij}}^2 = (x_{a_i} - x_{s_j})^2 + (y_{a_i} - y_{s_j})^2, \tag{A.31}$$

and

$$r_{s_{ij}}^2 = (x_{s_i} - x_{s_j})^2 + (y_{s_i} - y_{s_j})^2. \tag{A.32}$$

The remaining equations are the exact same as formulated for the thin-plate spline. Equations A.24 and A.25 remain the same since the spline is still used for a three-dimensional problem. Since the aerodynamic grid is three dimensional, when creating the $[R_a]$ matrix as shown in equation A.29, the aerodynamic grid points are projected to the spline plane on which the structural grid lies. Or in other words, the z-component of the grid coordinates are ignored.

Unlike the thin-plate spline, the structural-grid points can lie on the same plane for the infinite-plate spline. However, they can not lie in a line. Like the thin-plate spline, no two structural-grid points can be located at the same coordinates [1].

A.3   Spline Conclusions

Any spline matrix can be used with the aeroelastic program. Two have been implemented, the thin-plate spline and the infinite-plate spline. If a three-dimensional, structural grid is used, the thin-plate spline provides superior results [50]. If the structural grid is a two-dimensional, flat plate, the infinite-plate spline must be used because the thin-plate spline is invalid if all the points lie in a single plane. If the structural grid is based on a beam model with all the grid points in a straight line, neither of these two methods will work because neither method is valid if all the points lie in a line.

Appendix B. Structural Model

The semi-discrete equations of motion can be written as

$$[M]\{\ddot{u}\} + [C]\{\dot{u}\} + [K]\{u\} = \{F\} \tag{B.1}$$

where $[M]$ is the mass matrix, $[C]$ is the damping matrix, $[K]$ is the stiffness matrix, $\{F\}$ is the applied forces, $\{u\}$ is the modal displacements, $\{\dot{u}\}$ is the modal velocities, and $\{\ddot{u}\}$ is the modal accelerations [30].

One of the most widely used integration methods for solving this initial-value problem is the Newmark method [30], which consists of the following equations:

$$\left([M] + \gamma\Delta t[C] + \beta\Delta t^2[K]\right)\{\ddot{u}\}_{n+1} = \{F\}_{n+1} - [C]\left(\{\dot{u}\}_n + (1-\gamma)\Delta t\{\ddot{u}\}_n\right)$$
$$- [K]\left(\{u\}_n + \Delta t\{\dot{u}\}_n + \frac{\Delta t^2}{2}(1-2\beta)\{\ddot{u}\}_n\right), \tag{B.2}$$

$$\{\dot{u}\}_{n+1} = \{\dot{u}\}_n + \Delta t\left[(1-\gamma)\{\ddot{u}\}_n + \gamma\{\ddot{u}\}_{n+1}\right], \tag{B.3}$$

$$\{u\}_{n+1} = \{u\}_n + \Delta t\{\dot{u}\}_n + \frac{\Delta t^2}{2}\left[(1-2\beta)\{\ddot{u}\}_n - 2\beta\{\ddot{u}\}_{n+1}\right]. \tag{B.4}$$

If $\gamma = \frac{1}{2}$, this implicit method is second-order accurate [30]. This method is stable if $\Delta t \leq \frac{\Omega}{\omega}$ where ω is the maximum natural frequency [30]. If a linear acceleration is assumed, $\beta = \frac{1}{6}$ and $\Omega = 3.464$ [30].

Assuming a linear acceleration and no structural damping, equations B.2, B.3, and B.4 simplify to:

$$\left([M] + \frac{\Delta t^2}{6}[K]\right)\{\ddot{u}\}_{n+1} = \{F\}_{n+1} - [K]\left(\{u\}_n + \Delta t\{\dot{u}\}_n + \frac{\Delta t^2}{3}\{\ddot{u}\}_n\right), \quad \text{(B.5)}$$

$$\{\dot{u}\}_{n+1} = \{\dot{u}\}_n + \frac{\Delta t}{2}\left((\{\ddot{u}\}_n + \{\ddot{u}\}_{n+1})\right), \quad \text{(B.6)}$$

and

$$\{u\}_{n+1} = \{u\}_n + \Delta t\{\dot{u}\}_n + \frac{\Delta t^2}{6}\left(2\{\ddot{u}\}_n + \{\ddot{u}\}_{n+1}\right). \quad \text{(B.7)}$$

Within the aeroelastic routine, forces are calculated at the centroid of each aerodynamic grid wing face. These forces are then splined to the structural grid nodes. A generalized force vector for the modal system is then calculated from

$$\{F_g\} = [\Phi]^T\{F_s\}. \quad \text{(B.8)}$$

$\{F_g\}$ is the generalized force and moment vector, $\{F_s\}$ is the force and moment vector for the structural grid nodes, and $[\Phi]$ is the modal matrix, the columns of which are the eigenvectors. There is a slight phase lag between the fluid solver and the structure. The forces can be extrapolated forward in time to try and mitigate this phase lag if desired. The extrapolated, generalized force and moment vector is calculated as

$$\{F_g\}_N = 2.5\{F_g\}_N - 2.0\{F_g\}_{N-1} + 0.5\{F_g\}_{N-2}. \quad \text{(B.9)}$$

Once the forces are determined, Equation B.5 is first solved for the generalized acceleration vector $\{\ddot{u}\}_{n+1}$ using an LUP-decomposition [11]. Equations B.6 and B.7 are then solved directly to get the generalized velocity vector $\{\dot{u}\}_{n+1}$ and the generalized displacement vector $\{u\}_{n+1}$. Displacement and rotation of the structural

grid nodes are then found from

$$\{\delta_s\} = [\Phi]\{u\}_{n+1}. \tag{B.10}$$

These new displacements are then splined to get new aerodynamic grid displacements and coordinates in order to deform the mesh.

Appendix C. Grid Convergence Study

Once the aeroelastic program was validated, it was used to study LCO of the Goland$^+$ wing described in section 3.2.2. Four grids were built to look at grid convergence; a coarse grid consisting of 68,949 tetrahedral cells with 518 cell faces on the wing, a medium grid consisting of 269,596 tetrahedral cells with 13,358 cell faces on the wing, a fine grid consisting of 660,347 tetrahedral cells with 42,102 cell faces on the wing, and a viscous grid consisting of 2,203,065 tetrahedral, prism, and pyramid cells with 54,886 cell faces on the wing. The coarse, medium, and fine grids were tested using the inviscid solver. The viscous grid was tested using the Spalart-Allmaras turbulence model. These grids were used to compute steady state solutions for Mach 0.92, 600 ft/sec (182.88 m/sec), at angles of attack of 0 to 20 degrees in 2 degree increments. C_L and C_M plots are shown in Figure C.1. Below 11 degrees angle-of-attack, all of the inviscid grids produced similar C_L and C_M results. The viscous grid C_L results are less and the C_M results are more than the results produced by the inviscid grids. Above 11 degrees, the coarse grid is under-predicting C_L and slightly over predicting C_M while the viscous results and medium grid inviscid results were approximately the same. The viscous results did not predict a stall under 20 degrees, however, a small separation bubble behind the leading edge did appear at 10 degrees angle-of-attack and continued to grow larger as the angle-of-attack was increased. The inviscid fluid solver failed in this region for the fine grid at angles-of-attack greater than 12 degrees.

A slice through the wing was taken at 3.2808 ft (1 m) span and the coefficient of pressure for the airfoil was plotted. As can be seen in figures C.2 - C.12, the coarse grid did not accurately capture the pressure distribution across the wing. At zero degrees angle-of-attack, the shock was located at a chord position of 4.921 ft (1.5 m). For the inviscid grids, as the angle-of-attack was increased to 2 degrees, the shock moved immediately to the trailing edge of the wing. For the viscous grid,
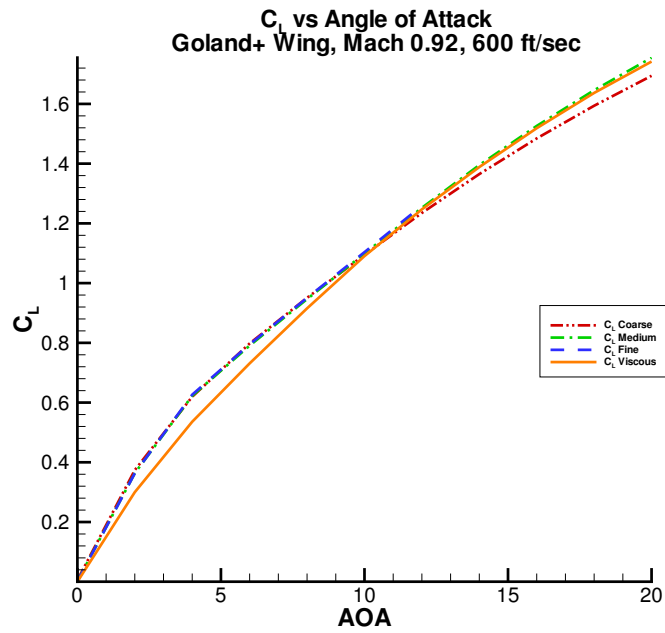
(a) C_L
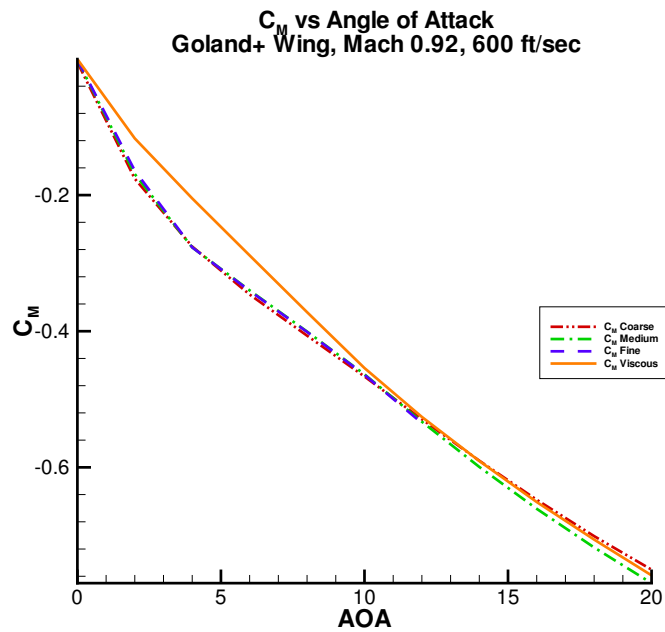
(b) C_M

Figure C.1 C_L and C_M vs Angle-of-Attack

C-2

Figure C.2 C_P plots for Mach 0.92, 600 ft/sec (182.88 m/sec), 0 degrees

Figure C.3 C_P plots for Mach 0.92, 600 ft/sec (182.88 m/sec), 2 degrees

Figure C.4 C_P plots for Mach 0.92, 600 ft/sec (182.88 m/sec), 4 degrees

Figure C.5 C_P plots for Mach 0.92, 600 ft/sec (182.88 m/sec), 6 degrees

Figure C.6 C_P plots for Mach 0.92, 600 ft/sec (182.88 m/sec), 8 degrees
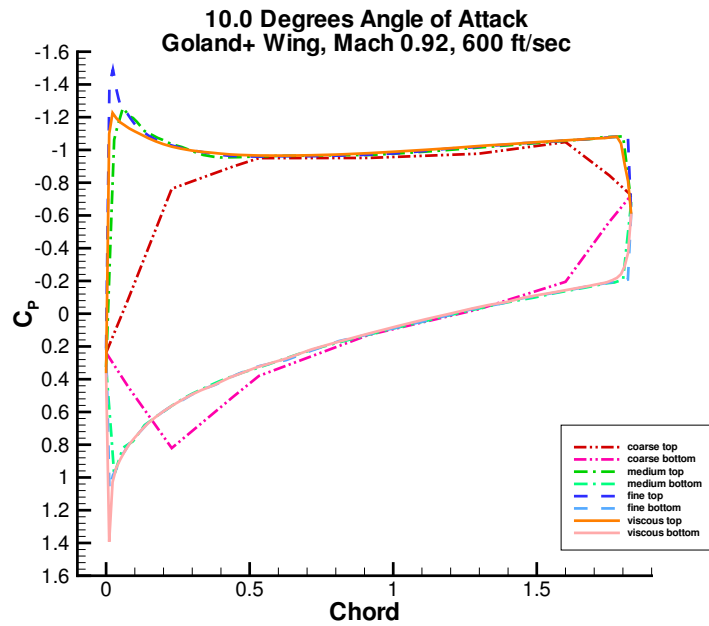
Figure C.7 C_P plots for Mach 0.92, 600 ft/sec (182.88 m/sec), 10 degrees
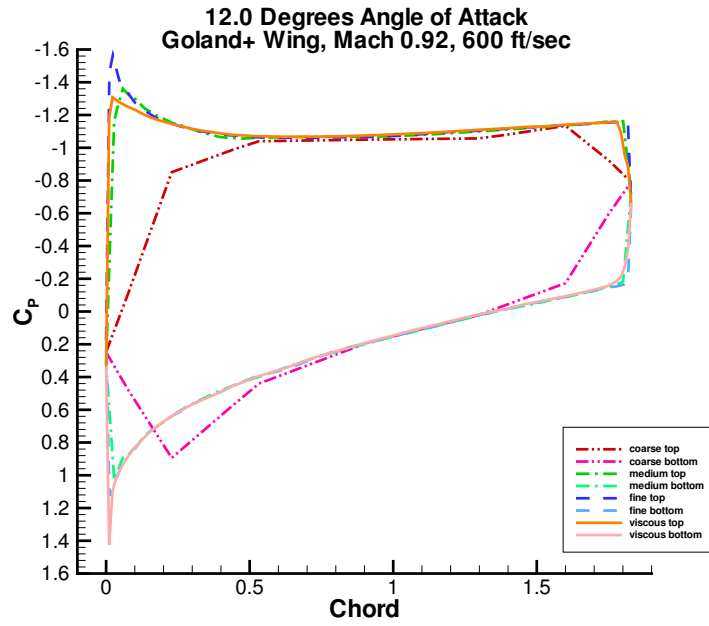
Figure C.8 C_P plots for Mach 0.92, 600 ft/sec (182.88 m/sec), 12 degrees
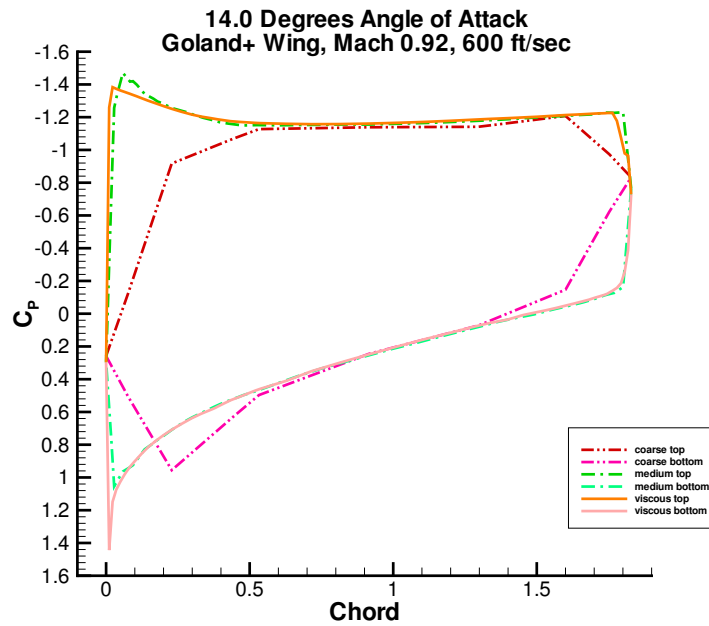
Figure C.9 C_P plots for Mach 0.92, 600 ft/sec (182.88 m/sec), 14 degrees
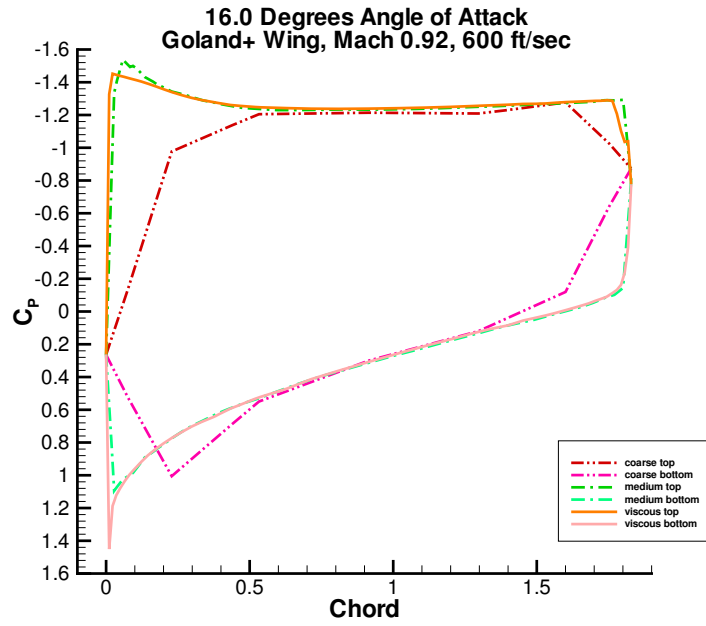
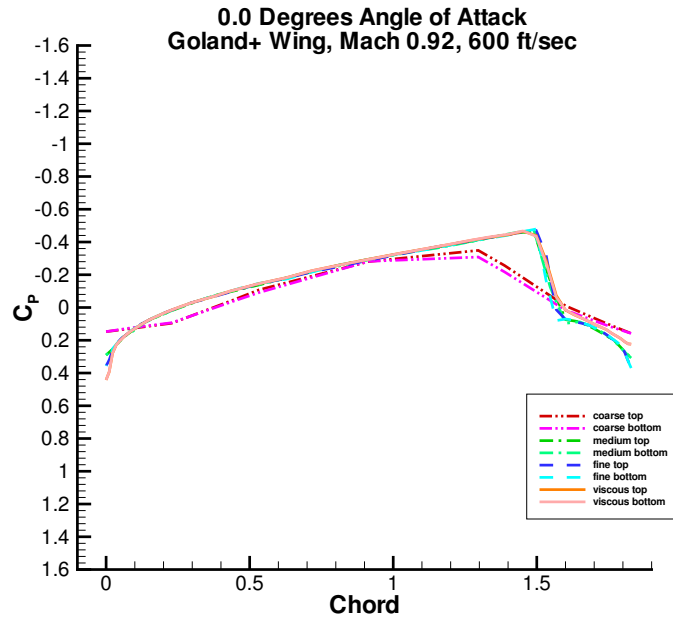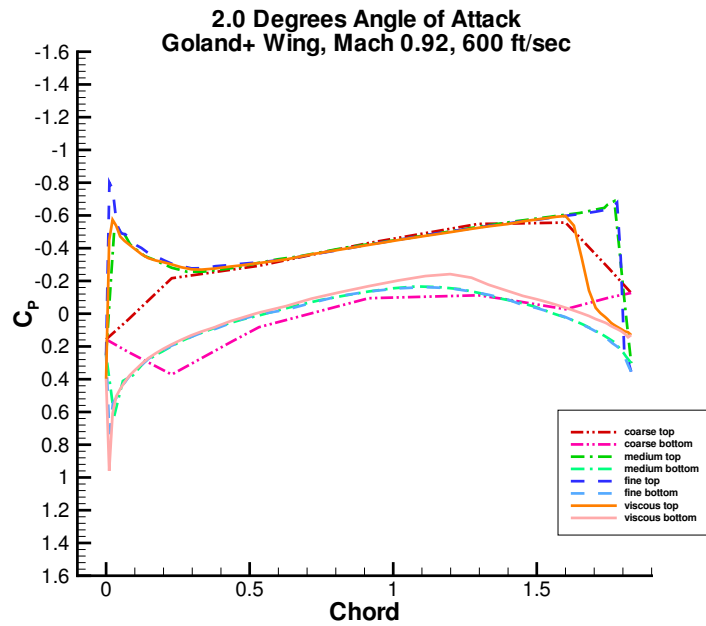Figure C.10 C_P plots for Mach 0.92, 600 ft/sec (182.88 m/sec), 16 degrees
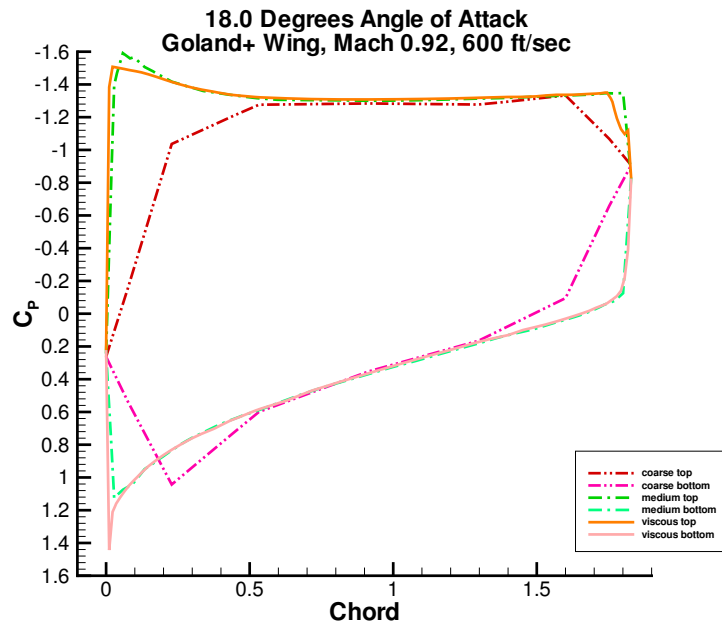
Figure C.11 C_P plots for Mach 0.92, 600 ft/sec (182.88 m/sec), 18 degrees

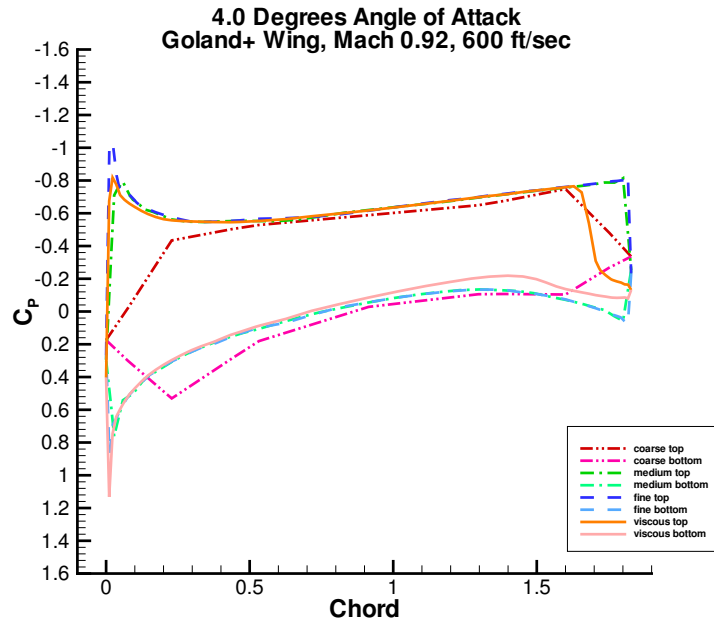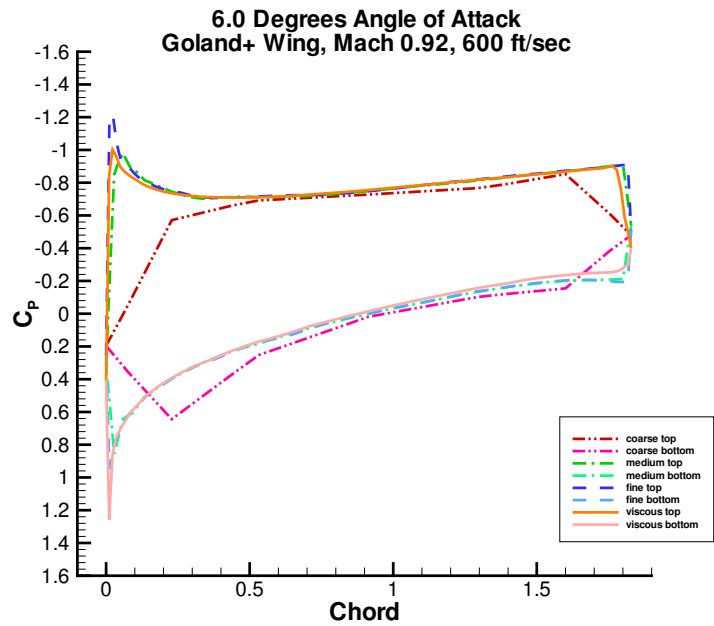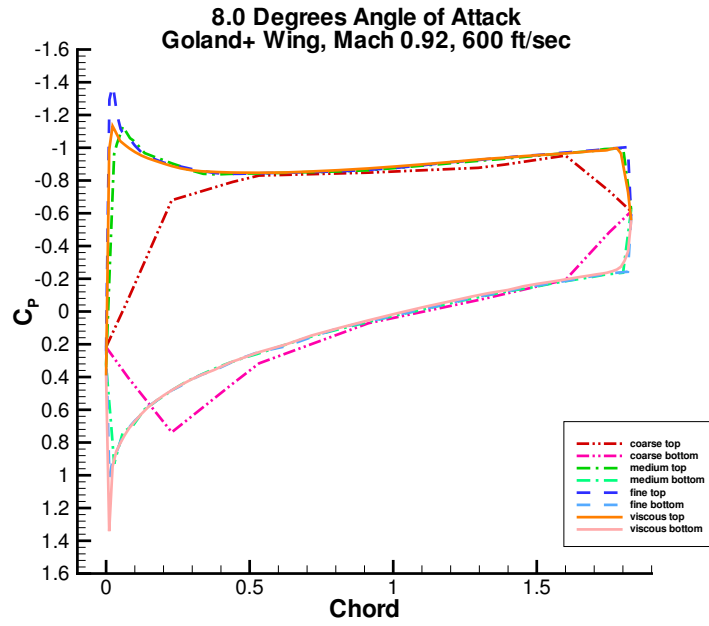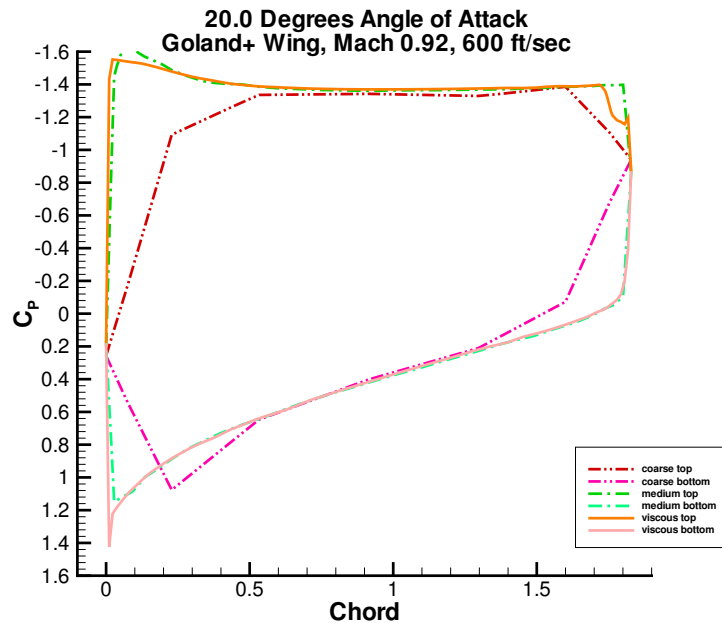Figure C.12 C_P plots for Mach 0.92, 600 ft/sec (182.88 m/sec), 20 degrees

the shock slowly moved aft and did not reach the trailing edge until approximately 8 degrees. At 14 degrees angle-of-attack and above, the viscous results showed that the flow separated behind the shock on the top of the wing.

The coarse grid failed to accurately capture the pressure distribution at the leading and trailing edge of the wing but it did capture the pressure distribution in the center of the wing. A fourth inviscid grid was then built that fell between the coarse and medium grids. This grid correctly captured the pressure distribution at the leading and trailing edge of the wing, but with fewer cells than the medium grid. It consisted of 194,780 tetrahedral cells with 9,178 cell faces on the wing. This grid was used to compute a clean-wing baseline solution against which all other LCO simulations were compared.

At 600 ft/sec (182.88 m/sec) and Mach 0.92, the dynamic pressure is beyond the flutter point and was shown by Snyder, et al. [51] to result in LCO. For the Goland+, these flow conditions fall within the transonic flutter dip region. This

case was used as a baseline for all simulations in this study. To match the conditions of Snyder, et al. [51], the far-field density, temperature, and pressure were set to 0.0023771 $slugs/ft^3$ (1.225 kg/m^3), 518.67°R (288.15 K), and 722.1813 lb/ft^2 (34578.04 Pa) respectively, while R was set to 585.7438 $\frac{ft \cdot lb_f}{slug \cdot °R}$ ($R = 97.951$ $\frac{N \cdot m}{Kg \cdot K}$).

LCO for the Goland$^+$, clean-wing was computed on all five grids discussed above, at 600 ft/sec (182.88 m/sec), Mach 0.92. The three coarsest inviscid grids correctly captured the LCO. This was initially surprising, because the coarse grid did not accurately capture the pressure distribution on the wing at the leading and trailing edges, nor did it accurately define the shock location due to the large size of the cells. However, because the structural grid was coarser than even the coarse aerodynamic grid, all of the aerodynamic grids produced a similar force distribution when transferred to the structural grid. The amplitudes of the LCO and the modal contributions were approximately the same regardless of the grid. The only significant variation in the LCO due to grid refinement was in the frequency. The frequency was 3.37 Hz for the coarse grid, 3.31 Hz for the baseline grid, and 3.27 Hz for the medium grid. The computation time varied greatly. It took approximately 5.5 hours to produce one second of data using six 2.2 GHz opteron processors on the coarse grid, 15.6 hours on the baseline grid, and 21 hours on the medium grid.

The fine grid produced only 6.584 seconds of data before the fluid solver failed. This failure was due to the twist producing high angles-of-attack at the wing tip, and the solver's inability to handle the adverse pressure gradient that appeared behind the leading edge. This failure was in the same location that the steady, viscous runs showed a very small separation bubble. The coarse grids averaged out this small problem area so that the solver did not crash. When the solver failed, C_L was oscillating at a frequency of 3.15 Hz and the frequency was increasing. With this grid, it took 27.3 hours to produce one second of data using six 2.2 GHz opteron processors.

The viscous grid using the Spalart-Allmaras turbulence model was run for less than 3 seconds because of very large computation times. With this grid, it was taking seven days to produce one second of data using sixteen 2.2 GHz opteron processors. As the amplitudes continued to grow and the motion continued to increase, the computational time required for each time step was increasing. Therefore, this aeroelastic analysis tool was found to be inadequate for viscous calculations.

Appendix D. Goland⁺ with NACA 65-004 Airfoil

To determine whether the airfoil affects the flow of energy between the fluid and the structure, or whether the flow of energy was independent of the airfoil, the Goland⁺, biconvex airfoil was replaced with a NACA 65-004 airfoil. Since the airfoil affects the shock strength, location, and movement, it was expected to affect the amplitude of the LCO. With the biconvex airfoil, LCO was established by 6.4 seconds with a mode 1 amplitude of ±8.8 as discussed above. With the same initial perturbation and flow conditions, the NACA 65-004 airfoil mode 1 amplitude only realized ±1.4 after 15 seconds (Figure D.1). This demonstrated that the airfoil was critical to the transfer of energy between the structure and fluid. A large initial velocity perturbation was then given to the NACA 65-004 configuration (Figure D.2). The large perturbation quickly accelerated the motion past the LCO conditions seen with the bi-convex wing. Mode 1 and mode 2 were still in phase as they were for the bi-convex wing. This led to the same trailing-edge and leading-edge shock structure (Figure D.3) as previously seen. At 6.365 seconds the inviscid fluid solver crashed due to the large angle-of-attack. Based on the shock structure and mode coupling, it was hypothesized that it would settle into LCO, although at an angle-of-attack higher than the inviscid fluid solver was capable of simulating. Regardless, this case demonstrated the importance of the airfoil on the LCO solution. The airfoil dictated how fast the oscillations grew and the final LCO amplitudes. The coupling of the modes and the corresponding shock motion determined whether a damping mechanism was present that could lead to LCO.
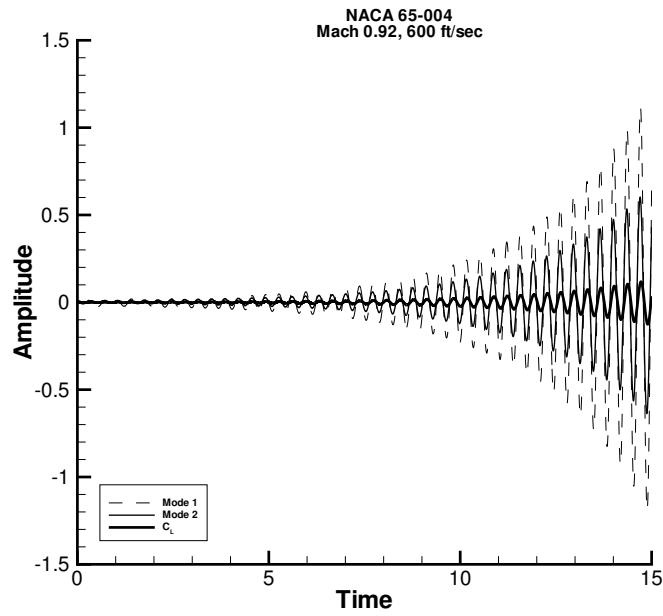
Figure D.1   NACA 65-004 C_L and Modal Amplitudes
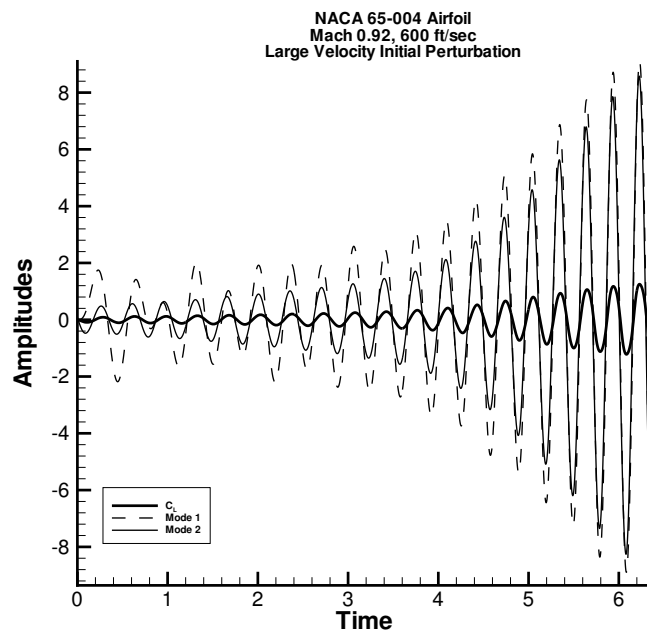
Figure D.2   NACA 65-004 (Large Velocity Perturbation) C_L and Modal Amplitudes
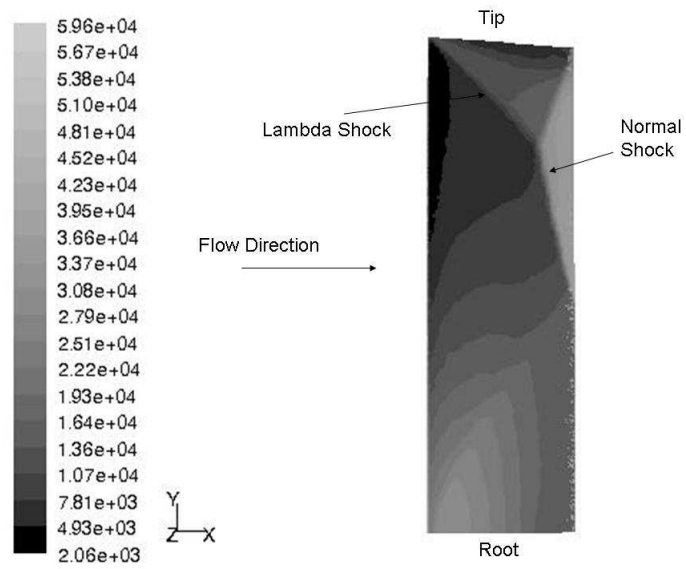
Figure D.3   Clean Wing with NACA 65-004 Airfoil Pressure Contours

Appendix E. LCO at Positive Angle-of-Attack

To determine whether the angle-of-attack of the wing affects the flow of energy between the fluid and the structure, the root angle-of-attack was changed from 0.0 degrees to 2.0 degrees. Changing the angle-of-attack changed the static aeroelastic solution, causing a displacement of the static values about which the modes and C_L (Figure E.1) oscillated. The wing oscillated about a C_L of 0.1676 instead of 0.0 and about a tip angle-of-attack of 1.36 degrees instead of 0.0 degrees. This new neutral point was the new static aeroelastic solution for the wing at 2.0 degrees angle-of-attack. The pattern of the energy flow between the fluid and structure was unaffected.
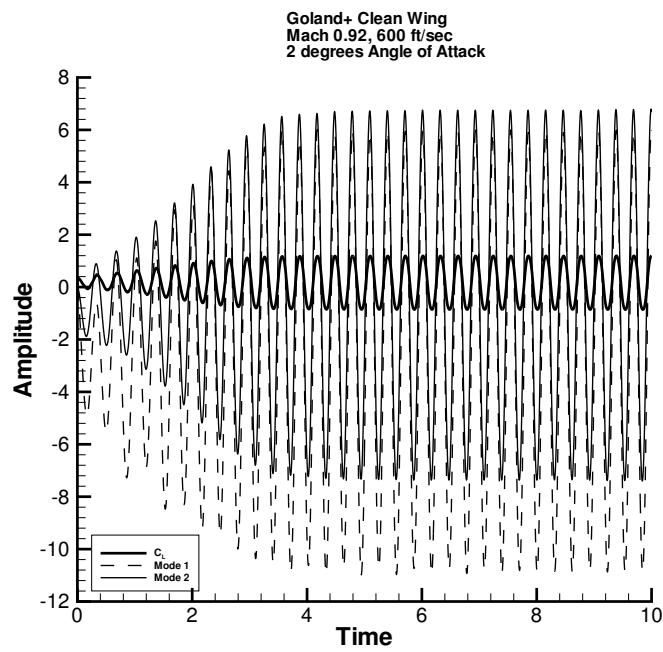
Figure E.1 C_L and Modal Amplitudes at 2.0 Degrees Angle-of-Attack

Appendix F.   F–16 Results

Air Force SEEK EAGLE Office used a block 40 F–16C for LCO testing [15]. The F–16 has a cropped delta wing, blended with the fuselage. It has a wingspan of 32 ft, 8 in (9.9568 m) and a NACA 64A-204 airfoil. The wing aspect ratio is 3.2 and the leading-edge sweep is 40 degrees [15]. The configuration shown in Figure F.1 exhibited LCO in level flight test conditions ranging from Mach 0.70 to Mach 0.95 at 2,000 ft, 5,000 ft, and 10,000 ft pressure altitude [15].

An attempt to compute the F–16 LCO state with the aeroelastic program was made. The store configuration and mass properties used by the modal structural model obtained from Denegri [15], are shown in Tables F.1 and F.2. The modal structural model consisted of 26 modes which ranged in frequency from 5.21 Hz to 24.33 Hz [15]. The first six modes are shown in Figure F.2. An inviscid grid made up of 1,189,805 tetrahedral cells was created for this problem. The under-wing stores and the fuselage were not modelled in the aerodynamic grid, but the tip launcher was modelled. The wing was projected to the centerline through the area located by the fuselage, therefore, the total span was correct (Figure F.3). Denegri [15] found that the dominant LCO modes were anti-symmetric, therefore, both sides of the F–16 wing were modelled. The 2,000 ft pressure altitude, Mach 0.90 test condition was simulated. Acceleration data for the aerodynamic grid point corresponding to the forward, vertical accelerometer was collected. This was compared to the flight-

Figure F.1   F–16C Store Configuration

Table F.1   F–16 Store Configuration and Attachment Reference Points

Station[*]	Location	x (in.)	y (in.)	z (in.)	Store	Suspension equipment
1	Wingtip	380.46	180.00	92.00	None	LAU-129/A launcher
2	Underwing	371.56	157.00	91.35	AIM-9P missile	LAU-129/A launcher
3	Underwing	349.67	120.00	90.72	Air-Ground missile	Launcher/pylon
4	Underwing	316.87	71.00	90.02	Empty 370 gal. tank	Fuel Pylon

[*] Left wing station loading. For the flight test, the right wing was configured as a mirror image of the left wing.

Table F.2   F–16 Store Mass Properties

Store	Weight	Center of gravity[*]			Moments of inertia (slug-ft.^{2})		
	(lb.)	x(in.)	y(in.)	z(in.)	Roll	Pitch	Yaw
LAU-129/A wingtip launcher	84.9	-15.20	0.00	-0,01	–	13.73	13.70
AIM-9P missile, LAU-129/A underwing launcher, and missile pylon	276.3	-14.65	0.01	-13.30	1.31	68.63	67.77
Air-ground missile, launcher, and weapon pylon	898.7	-2.27	0.02	-20.72	19.72	134.74	116.95
370 gallon fuel tank (empty) and pylon	470.5	-1.85	-0.18	-10.00	–	197.93	187.64

[*] Positive values are aft, outboard, or above the store attachment reference point x-y-z locations (see Table F.1).

test results shown in Figure F.4 [15]. This figure shows that the wing-tip response amplitude was about ±3g or $1,158\ in/sec^2$ ($29.42\ m/s^2$) for this test condition.

With an initial modal displacement perturbation of 0.02 to mode 2, after 11 seconds, the wing-tip response amplitude was around $180\ in/sec^2$ ($4.57\ m/s^2$), but still growing. Since the computation time for this grid was over 50 hours for one second of data on sixteen 2.2 GHz Opteron processors, it would take too long to determine whether LCO would develop using this small initial perturbation. The accelerations had a frequency of 8.4 Hz, which was close to that reported by Denegri [15].

A large, initial-velocity perturbation of 10.0 was given to mode 4 to determine if run times could be reduced. The large initial perturbation kicked the wing to
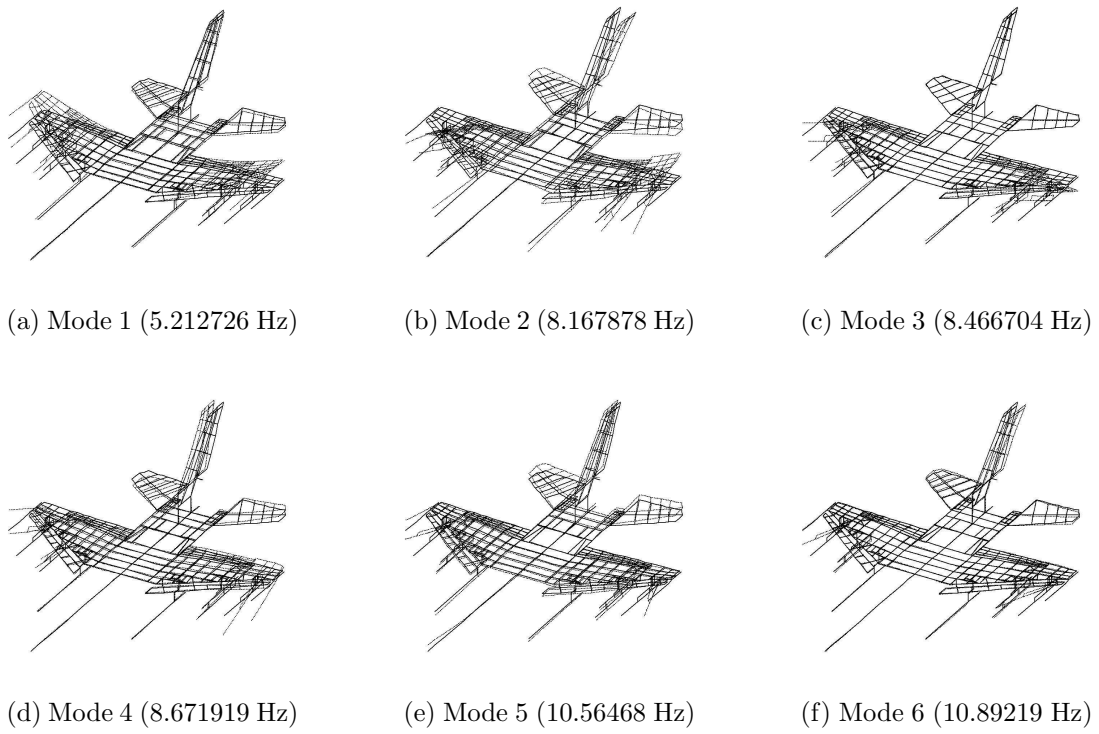
(a) Mode 1 (5.212726 Hz)   (b) Mode 2 (8.167878 Hz)   (c) Mode 3 (8.466704 Hz)

(d) Mode 4 (8.671919 Hz)   (e) Mode 5 (10.56468 Hz)   (f) Mode 6 (10.89219 Hz)

Figure F.2   Mode Shapes for F–16C
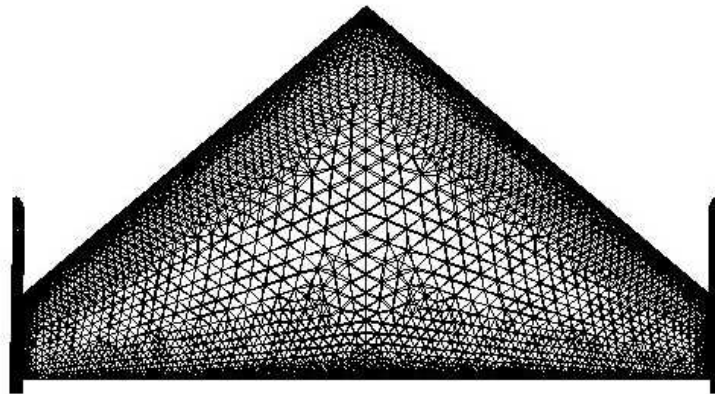
Figure F.3   F–16C Inviscid Grid
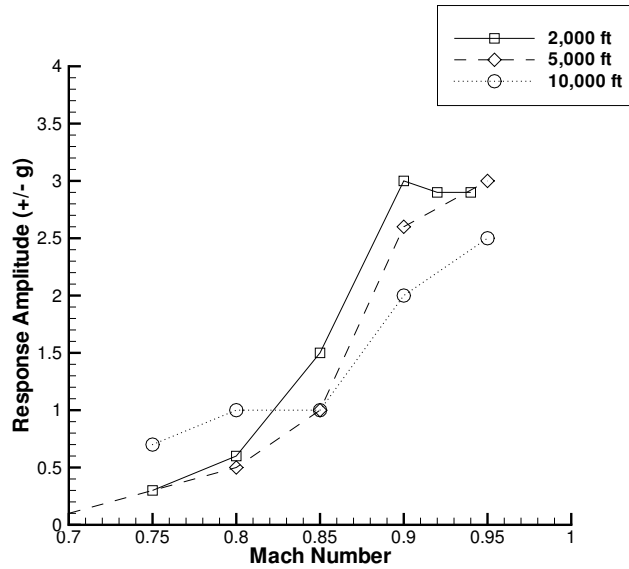
Figure F.4   F–16C Wing-Tip Response

the acceleration levels seen in flight test, but did not result in LCO. The amplitudes continued to grow resulting in divergent flutter (Figure F.5). Modes 2 and 4 were the dominant modes. Mode 2 was the first anti-symmetric bending mode and mode 4 was the first anti-symmetric twisting mode. These two modes were 107 degrees out of phase and did not couple into a single degree-of-freedom flutter mode as did the Goland+ wing (Figure F.6). These results imply that the structural model, as implemented, did not correctly or completely model the structure or that there is a different mechanism responsible for LCO in the F–16 than that found in the Goland+ wing. The different mechanism could be boundary-layer/shock-wave interaction or shock-induced separation on the wing, both of which require viscous modelling.

Additional testing is required to determine whether LCO can be obtained with this simplified wing or whether additional grid details, such as the fuselage and underwing stores, need to be included. Viscous modelling may also be necessary to duplicate the flight test results. Other researchers are also trying to simulate this flight-test scenario [14, 54, 55], but to date, no one has been able to completely duplicate the flight-test results.

Figure F.5   F–16 Wing-Tip Acceleration (Large Initial Condition)

Figure F.6   F–16 Modal Amplitudes

References

1. *ZAERO version 5.2 Theoretical Manual.* ZONA Technology, Inc., Scottsdale, AZ, 13 edition, 2001.

2. *FLUENT 6.1 User's Guide.* FLUENT, Inc., Lebanon, NH, 2003.
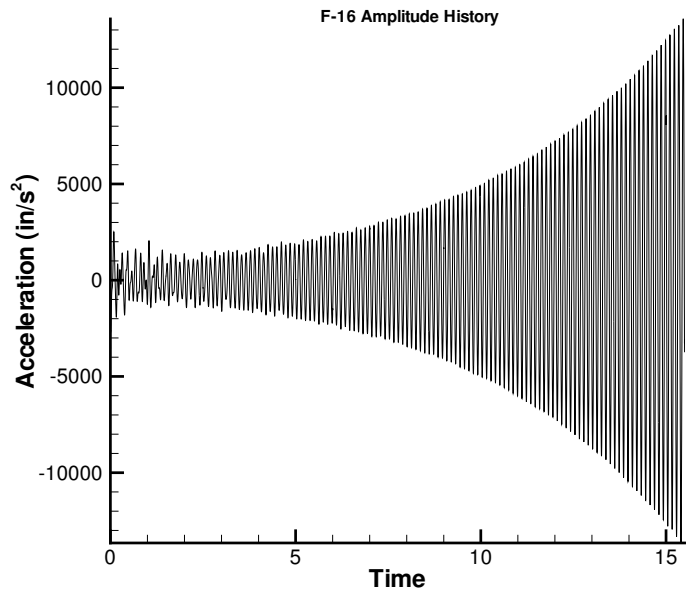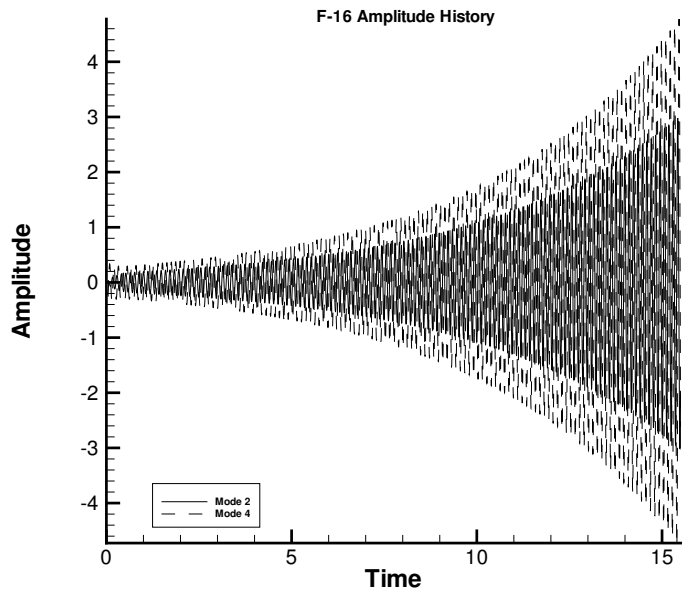
3. Batina, J.T., D.A. Seidel, S.R. Bland, and R.M. Bennett. "Unsteady Transonic Flow Calculations for Realistic Aircraft Configurations". AIAA-87-0850, 1987.

4. Belk, Davy M. and Raymond C. Maple. "Automated Assembly of Structured Grids for Moving Body Problems". AIAA-95-1680-CP, 1995.

5. Bendiksen, O.O. "Transonic Limit Cycle Flutter/LCO". AIAA-2004-1694, 45th AIAA/ASME/ASCE/AHS/ASC Structures, Structural Dynamics, and Materials Conference, Palm Springs, CA, April 19-22, 2004.

6. Beran, P.S., N.S. Khot, F.E. Eastep, R.D. Snyder, and J.V. Zweber. "Numerical Analysis of Store-Induced Limit-Cycle Oscillation". *Journal of Aircraft*, 41(6):1315–1326, November-December 2004.

7. Beran, P.S., N.S. Khot, F.E. Eastep, R.D. Snyder, J.V. Zweber, L.J. Huttsell, and J.N. Scott. "The Dependence of Store-Induced Limit-Cycle Oscillation Predictions on Modelling Fidelity". Paper #44, RTO Applied Vehicle Technology Panel Symposium on Reduction of Military Vehicle Acquisition Time and Cost Through Advanced Modelling and Virtual Product Simulation, Paris, France, April 22-25, 2002.

8. Bunton, Robert W. and Charles M. Denegri Jr. "Limit Cycle Oscillation Characteristics of Fighter Aircraft". *Journal of Aircraft*, 37(5):916–918, September-October 2000.

9. Cai, J., F. Liu, and H.M. Tsai. "Static Aeroelastic Computation with a Coupled CFD and CSD Method". AIAA-2001-0717, 39th AIAA Aerospace Sciences Meeting & Exhibit, Reno, NV, January 8-11, 2001.

10. Chen, P.C., E. Sulaeman, D.D. Liu, and C.M. Denegri Jr. "Influence of External Store Aerodynamics on Flutter/LCO of a Fighter Aircraft". AIAA-2002-1410, 43rd AIAA/ASME/ASCE/AHS/ASC Structures, Structural Dynamics, and Materials Conference, Denver, CO, April 22-25, 2002.

11. Cormen, Thomas H., Charles E. Leiserson, and Ronald L. Rivest. *Introduction to Algorithms*. MIT Press, Cambridge, MA, 2 edition, 2001.

12. Denegri, Charles M., James A. Dubben, and Daniel L. Maxwell. "In-Flight Wing Deformation Characteristics During Limit-Cycle Oscillations". *Journal of Aircraft*, 42(2):500–508, March-April 2005.

13. Denegri, Charles M. Jr. "Limit Cycle Oscillation Flight Test Results of a Fighter with External Stores". AIAA-2000-1394, 41st AIAA/ASCE/AHS/ASC Structures, Structural Dynamics, and Materials Conference, Atlanta, GA, April 3-6, 2000.

14. Denegri, Charles M. Jr. and James A. Dubben. "F-16 Limit Cycle Oscillation Analysis Using Transonic Small-disturbance Theory". AIAA-2005-2296, 46th AIAA/ASCE/AHS/ASC Structures, Structural Dynamics, and Materials Conference, Austin, TX, April 18-21, 2005.

15. Denegri, Charles M. Jr. and James A. Dubben. "In-Flight Wing Deformation Characteristics During Limit Cycle Oscillations". AIAA-2003-1426, 44th AIAA/ASCE/AHS/ASC Structures, Structural Dynamics, and Materials Conference, Norfolk, VA, April 7-10, 2003.

16. Dowell, E., J. Edwards, and T.W. Strganac. "Nonlinear Aeroelasticity". AIAA-2003-1816, 44th AIAA/ASCE/AHS/ASC Structures, Structural Dynamics, and Materials Conference, Norfolk, VA, April 7-10, 2003.

17. Dowell, Earl H. and Deman Tang. "Nonlinear Aeroelasticity and Unsteady Aerodynamics". *AIAA Journal*, 40(9):1697–1707, September 2002.

18. Duchon, Jean. "Splines Minimizing Rotation-Invariant Semi-Norms in Sobolev Spaces". W. Schempp and K. Zeller (editors), *Constructive Theory of Functions of Several Variables: Proceedings of a Conference Held at Oberwolfach, April 25-May 1, 1976*, 85–100. Springer-Verlag, Berlin, 1977.

19. Eastep, F.E. and J. J. Olsen. "Transonic Flutter Analysis of a Rectangular Wing with Conventional Airfoil Sections". *AIAA Journal*, 18(10):1159–1164, October 1980.

20. Farhat, C., M. Lesoinne, P.S. Chen, and S. Lanteri. "Parallel Heterogeneous Algorithms for the Solution of Three-Dimensional Transient Coupled Aeroelastic Problems". AIAA-95-1290-CP, 1995.

21. Farhat, C., K. Pierson, and C Degand. "CFD Based Simulation of the Unsteady Aeroelastic Response of a Maneuvering Vehicle". AIAA-2000-0899, 38th AIAA Aerospace Sciences Meeting & Exhibit, Reno, NV, January 10-13, 2000.

22. Farhat, Charbel, Philippe Geuzaine, Gregory Brown, and Chuck Harris. "Nonlinear Flutter Analysis of an F-16 in Stabilized, Accelerated, and Increased Angle of Attack Flight Conditions". AIAA-2002-1490, 43rd AIAA/ASME/ASCE/AHS/ASC Structures, Structural Dynamics, and Materials Conference, Denver, CO, April 22-25, 2002.

23. Geuzaine, Philippe, Gregory Brown, and Charbel Farhat. "Three-Field-Based Nonlinear Aeroelastic Simulation Technology: Status and Application to the Flutter Analysis of an F-16 Configuration". AIAA-2002-0870, 40th AIAA Aerospace Sciences Meeting & Exhibit, Reno, NV, January 14-17, 2002.

24. Geuzaine, Philippe, Gregory Brown, Chuck Harris, and Charbel Farhat. "Aeroelastic Dynamic Analysis of a Full F-16 Configuration for Various Flight Conditions". *Journal of Aircraft*, 41(3):363–371, March 2003.

25. Goland, Martin. "The Flutter of a Uniform Cantilever Wing". *Journal of Applied Mechanics*, 12(4):197–208, December 1945.

26. Gordnier, Raymond E. "Computation of Limit-Cycle Oscillations of a Delta Wing". *Journal of Aircraft*, 40(6):1206–1208, November-December 2003.

27. Gordnier, Raymond E. and Reid B. Melville. "Transonic Flutter Simulations Using an Implicit Aeroelastic Solver". *Journal of Aircraft*, 37(5):872–879, September-October 2000.

28. Harder, Robert L. and Robert N. Desmarais. "Interpolation Using Surface Splines". *Journal of Aircraft*, 9(2):189–191, February 1972.

29. Hodges, Dewey H. and G. Alvin Pierce. *Introduction to Structural Dynamics and Aeroelasticity.* Cambridge University Press, New York, NY, 2002.

30. Hughes, Thomas J. R. *The Finite Element Method – Linear Static and Dynamic Finite Element Analysis.* Prentice-Hall, Inc., Englewood Cliffs, NJ, 1987.

31. Huttsell, L., D. Schuster, J. Volk, J. Giesing, and M. Love. "Evaluation of Computational Aeroelasticity Codes for Loads and Flutter". AIAA-2001-0569, 39th AIAA Aerospace Sciences Meeting & Exhibit, Reno, NV, January 8-11, 2001.

32. Janardhan, Srinivasan, Ramana V. Grandhi, Frank Eastep, and Brian Sanders. "Parametric Studies of Transonic Aeroelastic Effects of an Aircraft Wing/Tip Store". *Journal of Aircraft*, 42(1):253–263, January-February 2005.

33. Kim, D.H., Y.M. Park, I. Lee, and O.J. Kwon. "Nonlinear Aeroelastic Computation of Wings with Pylon/Finned-Store Using Parallel Unstructured Euler Solver". AIAA-2002-1289, 43rd AIAA/ASME/ASCE/AHS/ASC Structures, Structural Dynamics, and Materials Conference, Denver, CO, April 22-25, 2002.

34. Kim, Dong-Hyun and In Lee. "Transonic and Supersonic Flutter Characteristics of a Wing-Box Model with Tip Stores". AIAA-2001-1464, 42nd AIAA/ASME/ASCE/AHS/ASC Structures, Structural Dynamics, and Materials Conference, Seattle, WA, April 16-19, 2001.

35. Kim, Dong-Hyun, Young-Min Park, In Lee, and Oh Joon Kwon. "Nonlinear Aeroelastic Computations of a Wing/Pylon/Finned-Store Using Parallel Computing". *AIAA Journal*, 40(1):53–62, January 2005.

36. Kolonay, R. M. *Unsteady Aeroelastic Optimization in the Transonic Regime.* Ph.D. thesis, Purdue University, Dept. of Aeronautics and Astronautics, Lafayette, IN, 1996.

37. Kwon, Hyuk J., Soo H. Park, Jae H. Lee, Yoonsik Kim, In Lee, and Jang H. Kwon. "Transonic Wing Flutter Simulation Using Navier-Stokes and $k - \omega$ Turbulent Model". AIAA-2005-2294, 46th AIAA/ASCE/AHS/ASC Structures, Structural Dynamics, and Materials Conference, Austin, TX, April 18-21, 2005.

38. Lee-Rausch, Elizabeth M. and John T. Batina. "Calculation of AGARD 445.6 Flutter Using Navier-Stokes Aerodynamics". AIAA-93-3476-CP, 1993.

39. Lijewski, Lawrence E. "Transonic Euler Solutions of a Wing-Pylon-Finned Body Configuration Using Blocked and Overlapping Grid Schemes". AIAA-91-2854-CP, 1991.

40. Liu, F., J. Cai, Y. Zhu, A.S.F. Wong, and H.M. Tsai. "Calculation of Wing Flutter by a Coupled CFD-CSD Method". AIAA-2000-0907, 38th AIAA Aerospace Sciences Meeting & Exhibit, Reno, NV, January 10-13, 2000.

41. Meijer, J.J. and A. M. Cunningham Jr. "Development of a Method to Predict Transonic Limit Cycle Oscillation Characteristics of Fighter Aircraft". *AGARD Conference Proceedings 507 – Transonic Unsteady Aerodynamics and Aeroelasticity*, AGARD-CP-507, 23–1 thru 23–21. AGARD, 1992.

42. Melville, Reid. "Nonlinear Mechanisms of Aeroelastic Instability for the F-16". AIAA-2002-0871, 40th AIAA Aerospace Sciences Meeting & Exhibit, Reno, NV, January 14-17, 2002.

43. Melville, Reid. "Nonlinear Simulation of F-16 Aeroelastic Instability". AIAA-2001-0570, 39th AIAA Aerospace Sciences Meeting & Exhibit, Reno, NV, January 8-11, 2001.

44. Melville, Reid. "Aeroelastic Instability of Tactical Aircraft in Nonlinear Flow Regimes". AIAA-2002-2970, 32nd AIAA Fluid Dynamics Conference, St. Louis, MO, June 24-26, 2002.

45. Melville, Reid B., Scott A. Morton, and Donald P. Rizzetta. "Implementation of a Fully-Implicit, Aeroelastic Navier-Stokes Solver". AIAA-97-2039-CP, 1997.

46. Morton, Scott A., Reid B. Melville, and Miguel R. Visbal. "Accuracy and Coupling Issues of Aeroelastic Navier-Stokes Solutions on Deforming Meshes". *Journal of Aircraft*, 35(5):798–805, September-October 1998.

47. Parker, G.H., R.C. Maple, and P.S. Beran. "The Role of Viscosity in Store-Induced Limit-Cycle Oscillation". AIAA-2005-1916, 46th AIAA/ASME/ASCE/AHS/ASC Structures, Structural Dynamics, and Materials Conference, Austin, TX, April 18-21, 2005.

48. Parker, G.H., R.C. Maple, and P.S. Beran. "The Role of Store Aerodynamics in Store-Induced Limit-Cycle Oscillation". Proceeedings of International Forum of Aeroelasticity and Structural Dynamics, Munich, Germany, June 28 - July 2, 2005.

49. Sadeghi, M., S. Yang, F. Liu, and H.M. Tsai. "Parallel Computation of Wing Flutter with a Coupled Navier-Stokes/CSD Method". AIAA-2003-1347, 41st AIAA Aerospace Sciences Meeting & Exhibit, Reno, NV, January 6-9, 2003.

50. Smith, Marilyn J., Dewey H. Hodges, and Carlos E. S. Cesnik. *An Evaluation of Computational Algorithms to Interface Between CFD and CSD Methodologies.* Technical Report WL-TR-96-3055, Wright Laboratory, Wright-Patterson AFB, OH, 1995.

51. Snyder, R.D., J.N. Scot, N.S. Khot, P.S. Beran, and J.V. Zweber. "Predictions of Store-Induced Limit-Cycle Oscillations Using Euler and Navier-Stokes Fluid Dynamics". AIAA-2003-1727, 44th AIAA/ASCE/AHS/ASC Structures, Structural Dynamics, and Materials Conference, Norfolk, VA, April 7-10, 2003.

52. Tang, L., R.E. Bartels, P.C. Chen, and D.D. Liu. "Simulation of Transonic Limit Cycle Oscillations using a CFD Time Marching Method". AIAA-2001-1292, 42nd AIAA/ASME/ASCE/AHS/ASC Structures, Structural Dynamics, and Materials Conference, Seattle, WA, April 16-19, 2001.

53. Terashima, H. and K. Fujii. "Effects of Number of Stores on the Transonic Flutter Characteristics of a Delta Wing Configuration". AIAA-2004-2234, 34th AIAA Fluid Dynamics Conference, Portland, OR, June 28-July 1, 2004.

54. Thomas, J.P., E.H. Dowell, K.C. Hall, and C.M. Denegri Jr. "Further Investigation of Modelling Limit Cycle Oscillation Behavior of the F-16 Fighter Using a Harmonic Balance Approach". AIAA-2005-1917, 46th AIAA/ASME/ASCE/AHS/ASC Structures, Structural Dynamics, and Materials Conference, Austin, TX, April 18-21, 2005.

55. Thomas, J.P., E.H. Dowell, K.C. Hall, and C.M. Denegri Jr. "Modelling Limit Cycle Oscillation Behavior of the F-16 Fighter Using a Harmonic Balance Approach". AIAA-2004-1696, 45th AIAA/ASME/ASCE/AHS/ASC Structures, Structural Dynamics, and Materials Conference, Palm Springs, CA, April 19-22, 2004.

56. Tijdeman, H. and R. Seebass. "Transonic Flow Past Oscillating Airfoils". *Annual Review of Fluid Mechanics*, 12:181–222, 1980.

57. Yates, E. Carson Jr. *AGARD Standard Aeroelastic Configurations for Dynamic Response I – Wing 445.6.* AGARD Report AGARD-R-765, NASA Langley Research Center, Hampton, VA, 1988.

Vita

Major Gregory H. Parker graduated as valedictorian from Purvis High School in Purvis, Mississippi in 1984. He received his Bachelor of Science Degree in Aeronautical Engineering from Mississippi State University in August 1988 and his Master of Science in December 1989. While at Mississippi State, he worked at the Raspet Flight Research Laboratory as a draftsman and later as a system engineer responsible for designing, building, installing, and testing, the aileron control system and fuel system for an all-composite, general aviation aircraft. He also designed an instrumentation system and data-reduction system for a general aviation aircraft under development for Honda Motor Company. Maj Parker was commissioned as a Second Lieutenant in the United States Air Force on 20 December 1988.

While on active duty with the Air Force, Maj Parker served as test manager for the MC-130H Combat Talon II in the Special Operations SPO, and as an aircraft systems analyst in the National Air Intelligence Center, at Wright-Patterson AFB, Ohio. As the B-2 engineering flight commander stationed at Whiteman AFB, Missouri, Maj Parker supervised a team of engineers, analysts, and instrumentation personnel and was directly responsible for all aspects of operational testing of the B-2 stealth bomber. While stationed at Eglin AFB, Florida, Maj Parker served as the AIM-120 test director where he was responsible for planning, coordinating, and executing AMRAAM operational test. He also served as the F-15 MSIP program manager and as the first Eglin F-15 combined-test-force (CTF) technical director where he was responsible for budgeting, planning, and reporting on all F-15 fighter tests.

In 2002 he was assigned to the Air Force Institute of Technology at Wright-Patterson AFB, Ohio where he was enrolled as a student in the aeronautical engineering doctoral program. Upon graduation he will be assigned to the Multidisciplinary Technologies Center at the Air Force Research Laboratories.

REPORT DOCUMENTATION PAGE

Form Approved
OMB No. 0704–0188

1. REPORT DATE *(DD–MM–YYYY)*	2. REPORT TYPE	3. DATES COVERED *(From — To)*
22–12–2005	Doctoral Dissertation	Sep 2002 — Dec 2005

4. TITLE AND SUBTITLE

Dynamic Aeroelastic Analysis of Wing/Store Configurations

5a. CONTRACT NUMBER

5b. GRANT NUMBER

5c. PROGRAM ELEMENT NUMBER

6. AUTHOR(S)

Parker, Gregory H., Major, USAF

5d. PROJECT NUMBER

5e. TASK NUMBER

5f. WORK UNIT NUMBER

7. PERFORMING ORGANIZATION NAME(S) AND ADDRESS(ES)

Air Force Institute of Technology
Graduate School of Engineering and Management
2950 Hobson Way
WPAFB, OH. 45433-7765

8. PERFORMING ORGANIZATION REPORT NUMBER

AFIT/DS/ENY/06-06

9. SPONSORING / MONITORING AGENCY NAME(S) AND ADDRESS(ES)

AFRL/VASD
Attn: Dr. Philip S. Beran
2210 8th Street
WPAFB, OH. 45433-7765

10. SPONSOR/MONITOR'S ACRONYM(S)

11. SPONSOR/MONITOR'S REPORT NUMBER(S)

12. DISTRIBUTION / AVAILABILITY STATEMENT

APPROVED FOR PUBLIC RELEASE; DISTRIBUTION UNLIMITED.

13. SUPPLEMENTARY NOTES

14. ABSTRACT

Limit-cycle oscillation, or LCO, is an aeroelastic phenomenon characterized by limited amplitude, self-sustaining oscillations produced by fluid-structure interactions. In order to study this phenomenon, code was developed to interface a modal structural model with a commercial computational fluid dynamics program. LCO was simulated for a rectangular wing, referred to as the Goland+ wing. It was determined that the aerodynamic nonlinearity responsible for LCO in the Goland+ wing was the combination of strong trailing-edge and lambda shocks which periodically appear and disappear. This mechanism limited the flow of energy into the structure which quenched the growth of the flutter, resulting in a steady LCO. Under-wing and tip stores were added to the Goland+ wing to determine how stores affected limit-cycle oscillation. It was found that aerodynamic store shapes affect LCO in two offsetting ways: under-wing stores interfere with the airflow on the lower surface of the wing which decreases LCO amplitudes, whereas, aerodynamic forces on both under-wing and tip stores directly increase LCO amplitudes.

15. SUBJECT TERMS

Aeroelasticity, Limit-Cycle, Computational Fluid Dynamics, Flutter, Limit-Cycle Oscillation, LCO, Wing/Store Configurations, Goland$^+$ Wing

16. SECURITY CLASSIFICATION OF:			17. LIMITATION OF ABSTRACT	18. NUMBER OF PAGES	19a. NAME OF RESPONSIBLE PERSON
a. REPORT	b. ABSTRACT	c. THIS PAGE			Raymond C. Maple, Lt Col, USAF (ENY)
U	U	U	UU	124	19b. TELEPHONE NUMBER *(include area code)* (937) 255–3636, ext 4577

Standard Form 298 (Rev. 8–98)
Prescribed by ANSI Std. Z39.18